A HIGH PRECISION STUDY OF LI-ION BATTERIES

by

Aaron Smith

Submitted in partial fulfilment of the requirements
for the degree of Doctor of Philosophy

at

Dalhousie University
Halifax, Nova Scotia
April 2012

DALHOUSIE UNIVERSITY

DEPARTMENT OF PHYSICS AND ATMOSPHERIC SCIENCE

The undersigned hereby certify that they have read and recommend to the Faculty of Graduate Studies for acceptance a thesis entitled "A HIGH PRECISION STUDY OF LI-ION BATTERIES" by Aaron Smith in partial fulfilment of the requirements for the degree of Doctor of Philosophy.

Dated: April 2, 2012

External Examiner: _____

Research Supervisor: _____

Examining Committee: _____

_____

Departmental Representative: _____

DALHOUSIE UNIVERSITY

DATE: April 2, 2012

AUTHOR: Aaron Smith

TITLE: A HIGH PRECISION STUDY OF LI-ION BATTERIES

DEPARTMENT OR SCHOOL: Department of Physics and Atmospheric Science

DEGREE: PhD CONVOCATION: May YEAR: 2012

_____

Signature of Author

To my wife

Table of Contents

List of Tables

List of Figures

Abstract

Undesired reactions in Li-ion batteries, which lead to *capacity* loss, can consume or produce charge at either the positive or negative electrode. For example, the formation and repair of the solid electrolyte interphase consumes Li^+ and e^- at the negative electrode. Electrolyte oxidation at the positive electrode allows extra electrons (with corresponding electrolyte decomposition products) to be extracted at the electrode compared to the number which could be extracted in the absence of electrolyte oxidation. High purity electrolytes, various electrolyte additives, electrode coatings and special electrode materials are known to improve cycle life and therefore must impact coulombic efficiency. Careful measurements of coulombic efficiency are needed to quantify the impact of different battery materials on cell life time **in only a few charge-discharge cycles and in a relatively short time**. In order to make an impact on Li-ion cells for automotive and energy storage applications, where thousands of charge-discharge cycles are required, coulombic efficiency must be measured to an accuracy and precision of at least 0.01%.

An instrument designed to make high-precision coulombic efficiency measurements on Li ion batteries is described in this thesis. Such measurements can be used to detect the influence of different electrode materials, voltage ranges, cell temperature, etc. on the performance of a cell. The effects of cycle induced and time-related *capacity* loss can be probed using experiments carried out at different C-rates. Precision differential voltage and *capacity* measurements can also be used to identify the different failure mechanisms that occur in full cells.

List of Abbreviations and Symbols Used

AA - atomic absorption

BET - Brunauer–Emmett–Teller

b(T,t) - parasitic reaction rate that depends on the cell temperature

CE - coulombic efficiency

CE_{pos} – coulombic efficiency of positive half cell

CE_{neg} - coulombic efficiency of positive half cell

dQ/dV(V, n) – differential capacity analysis

dV/dQ(Q, n) - differential voltage analysis

$dV/dQ(Q)_f$ - differential voltage with respect to charge of calculated full cell

$dV/dQ(Q)_p$ - differential voltage with respect to charge of positive half cell

$dV/dQ(Q)_n$ - differential voltage with respect to charge of negative half cell

E - *capacity* (in coulombs or mAh) of Li^+ in the electrolyte after the formation cycle

e^- - electrons

HPC - high precision charger

I – current

I_A - applied constant current

I_{Li} - effective parasitic current forming the SEI

I_{ox}^{a} - effective parasitic current caused by electrolyte oxidation

I_{ox}^{b} - effective parasitic current caused by shuttle mechanisms / metal ion dissolution

I_p - effective parasitic current caused by charge trapped in the positive electrode during

IRC – irreversible *capacity*

K - *capacity* still available in the positive electrode for additional lithium

k - proportionally constant

Li^+ - Li ions

LMO - $LiMn_2O_4$

MCMB - mesocarbon microbeads

m_n - active mass of the negative electrode

m_o – number of formation cycles

m_p - active mass of the positive electrode

n – cycle number

NMC - $Li[Ni_{1/3}Mn_{1/3}Co_{1/3}]O_2$

Q_c - is the charge *capacity* immediately preceding Q_d

$Q`_c$ - is the charge *capacity* immediately following Q_d

Q_d - is the discharge *capacity* of the cell

Q_o - cell *capacity*

q – specific *capacity*

q_{Li} – amount of charge consumed by the SEI in one half cycle

q_{ox}^{a} – amount of charge consumed by electrolyte oxidation in one half cycle

q_{ox}^{b} – amount of charge consumed by shuttle mechanisms / metal ion dissolution in one half cycle

q_p – amount of charge trapped in the positive electrode during each half cycle

R - *capacity* left in the graphite electrode

RTD - resistance temperature detector

S - *capacity* (in coulombs or mAh) of Li atoms in the SEI after the formation cycle

SEI - solid electrolyte interphase

T – temperature

t – time

V – voltage

XRD - x-ray diffraction

x - thickness of the passivating layer

ZBH - zero background holder

Δ_C - slippage per cycle at the top of charge

Δ_D - slippage per cycle at the bottom of discharge

ΔdQ/dV(V, n, m) – delta differential capacity analysis

ΔI - percentage accuracy in the current

ΔQ - percentage error in the cell *capacity*

ΔT - precision of the temperature control

Δt - interval between voltage measurements

ΔV - precision of the voltage measurement

δ_n - negative electrode slippage

δ_p - positive electrode slippage

θ – Bragg angle

μ - chemical potential

τ - is the time of one narrow range cycle

Acknowledgements

I would like to thank my supervisor Jeff Dahn for the opportunity to work in his group. Originally, the High Precision Charger project was nothing more than a simple idea, but with his help and experience it has become a point of great interest in the battery community. I would also like to thank Chris Burns, Simon Trussler, Nupur Sinha, Toby Bond, Hannah Dahn, David Stevens and all the summer students who have helped with this project in one way or another. Your help and advice has been invaluable. Finally, I would like to thank my wife Shawna for her patience and love.

Chapter 1 Introduction

Li-ion batteries are used in cellular phones, laptops, camcorders, and other portable electronic devices because they have high energy density and calendar lives of at least 3 – 4 years, enabling them to outlive the portable electronics that they power. New applications for Li-ion batteries in backup power supplies, satellites and electric vehicles demand significantly longer calendar lives. For example, batteries used in energy storage and automotive applications require a life time of at least 10 years, and must operate under challenging environmental conditions. Assuming the batteries are cycled once or twice a day for ten years, such as with electric vehicles, this would translate to a minimum of 3000 cycles, with 10000 cycles being a more preferable goal. The ability of Li-ion cells to operate under realistic conditions must be demonstrated; however this is problematic because such tests take an extremely long time. In an attempt to demonstrate the desired number of cycles, many battery manufacturers and researchers cycle their batteries 12 to 60 times per day [1–5]. Such accelerated testing methods may, however, lead to spurious conclusions about cycle life under realistic conditions due to the reduced time available for reactions which reduce cycle life to occur.

Over the past 10 years, only a few published results exist that report cell performance monitored over periods of months or years [6–12]. The most impressive of these articles, by Broussely et al. [6], observed the aging of cells over a period of 4 years. They demonstrated that the *capacity*, power, internal pressure, and impedance of Li-ion cells are strongly dependent on time. A proper choice of materials and a good cell design allows Li-ion batteries with a long expected life time to be made. Erik Scott et al.

demonstrated the effect of cycling rate on *capacity* loss for cells cycling for over two years [12]. They demonstrated that a cell cycled once a week had a larger fade in *capacity* per cycle than a cell cycled once a day. However, when the same data was plotted versus elapsed time it showed that the cell cycled once a day appeared to have a larger fade in *capacity* per unit time than the other cell. This demonstrates that both time and cycling affect the *capacity* retention of the cells. Unfortunately, such patient and careful publications are far too few.

Undesired reactions in Li-ion batteries can consume active lithium (lithium which can be inserted into or removed from either the positive or negative electrode) and convert it to inactive lithium (a lithium compound which can no longer be inserted into an electrode) in the cell. This loss of active lithium ultimately leads to *capacity* loss. For example, organic solvents in the electrolyte can react with Li ions, Li^+, and electrons, e^-, to form a layer of reduction products on the negative electrode [6,13]. During the formation of this layer, Li ions and electrons are consumed irreversibly and become inactive. The electrolyte can also decompose on the positive electrode, but in this case an oxidation product is formed and an equivalent number of electrons are passed to the positive electrode [13]. These additional electrons can than remove Li ions from the electrolyte and transfer them into either the negative or positive electrodes. Unfortunately, this gives the false impression that additional charge has been produced while, in reality, cell components have been lost. Advanced battery materials such as high purity electrolytes, electrolyte additives [14–20], electrode coatings [21–26] and special electrode materials [17] have been shown to reduce the above reactions and

improve cycle life. The sum effect of all the parasitic reactions inside a Li-ion cell can be monitored by carefully measuring the Coulombic Efficiency, CE, of the cell

$$CE = Q_d/Q_c = \text{charge delivered during discharge/charge stored during charge} \quad 1.1$$

As battery manufacturers produce cells that are increasingly free of unwanted side reactions, the CE becomes closer to unity (1.0000…) and the cells are able to cycle without loss of lithium, electrolyte decomposition, etc. In some cases, it is conceivable that side reactions at the positive and negative electrodes could be nonzero and balanced with each other. This would make it seem that the cell was cycling without the loss of active lithium. However, the existence of these reactions would be detected by a CE less than 1.0000 and cells would ultimately fail due to the consumption of cell components.

Many authors who study new electrode materials for Li-ion cells use CE measurements in their publications. For example, Wang et al. [27] studied TiO_2 hollow spheres as anode materials for Li-ion cells and reported: "the coulombic efficiency is approximately 98% after 40 cycles, indicating excellent cycling stability and reversibility". Of course, full Li-ion cells incorporating such a negative electrode would have a short cycle life. Yi et al. [28] report the CE of half cells using $LiNi_{0.5}Mn_{1.5}O_4$ and $LiMn_{1.4}Cr_{0.2}Ni_{0.4}O_4$, showing improved CE for the latter. However, the latter also had increased *capacity* fade. Song et al. [29] reported CE measurements for arrays of Si nanotubes and showed that the CE of cells cycled every 40 hours and 10 hours was 87% and 90% , respectively, for the first cycle. Zhange et al. [30] reported the CE of cells made with Fe_3O_4/graphene composites and Fe_3O_4 nano-particles and showed values close

to 98% after ten cycles. Obrovac and Krause [31] report the CE of crystalline Si electrodes made with an unspecified binder to be 99.8% after about 50-90 cycles. In references [27–30], the CE measurements show a significant amount of noise and scatter, about ±0.5 %, when CE is plotted versus cycle number. More care in the measurements may have been taken in ref. [31], because the scatter in the CE measurements is only about ±0.1 %. However, it is our contention that none of the measurements of CE presented in the literature are accurate or precise enough to be able to distinguish whether a battery will meet the demands of automotive or grid energy storage applications. For a battery to meet the goal of 3000 cycles it must have a CE better then 99.99%, which means one would have to be able to measure CE at least that well.

To achieve high precision measurements of CE there are four experimental factors that need to be carefully controlled. 1) The delivered charge and discharge currents must be accurately balanced and stable. 2) The measured voltage of the cell must be precise. 3) The length of time between voltage measurements must be as short as possible. 4) The temperature of the cells must be held constant. Unfortunately, traditional battery testers are simply unequipped to achieve all 4 criteria.

Figure 1.1 shows a photograph of the high precision charge (HPC) at Dalhousie University. The HPC is a special battery testing system designed to control all the necessary variables needed to measure the CE of an electrochemical cell to within ±0.01% [32]. The HPC is an extremely useful experimental device and has been used to show the behaviors of various parasitic reactions and make accurate long term projections about cell life [33–37].

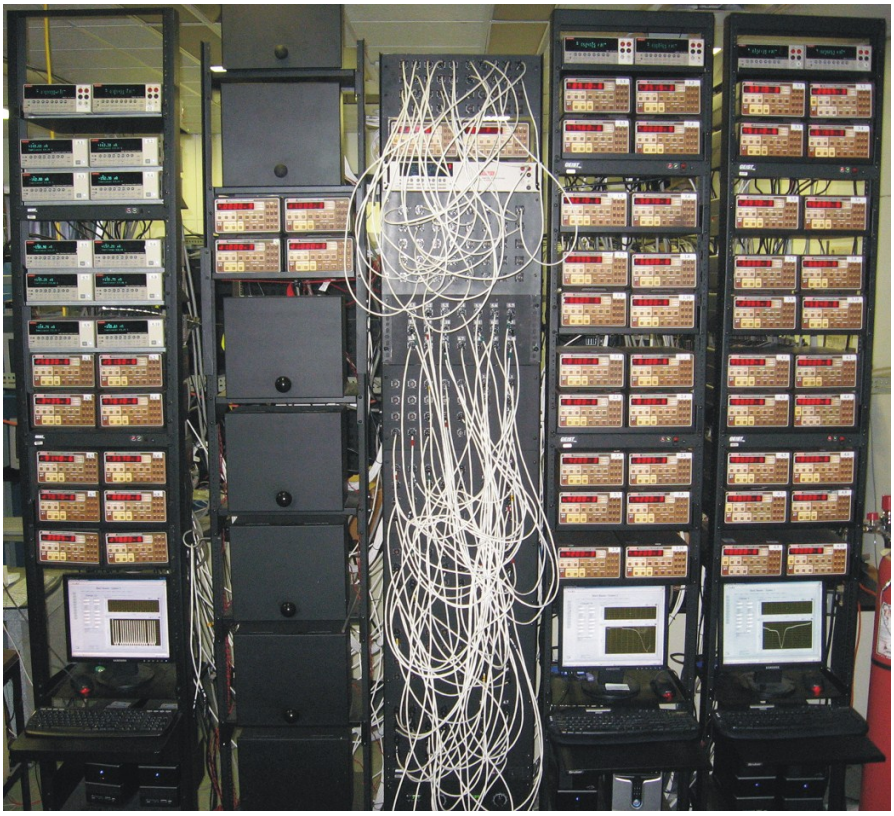

Figure 1.1 Photograph of the high precision charger at Dalhousie University

The aim of this thesis is to develop advanced testing equipment and techniques, like the HPC, to observe different failure mechanisms in Li-ion cells. If these mechanisms can be better understood this could lead to better projections of cell life times and suggest improved cell designs and materials. However, in order to understand these mechanisms all aspects of Li-ion cells must be understood.

Chapter 2 introduces the components of a Li-ion cell. The chapter discusses some of the common materials used in positive and negative electrodes, as well as the salts and solvents used in the electrolyte. Lastly, the designs of different types of cells used in this thesis are introduced.

Chapter 3 discusses some the degradation mechanisms common to Li-ion cells. These parasitic reactions can convert active lithium in a cell to inactive lithium through a

number a different reactions routes. Ultimately, this loss of active lithium leads to loss of cell *capacity* and eventually cell death.

Chapter 4 introduces the concept of high precision coulometry as an approach for testing Li ion cells. The requirements for high precision measurements will be discussed and compared to commercial testing equipment available today. The instrument will be described in detail and example data will be provided.

Chapter 5 introduces the automated storage/cycling equipment developed by the author, Chris Burns and Nupur Sinha. The device will be described in detail along with the necessary formulations for understanding storage/cycling results.

Chapter 6 discusses the concept of differential capacity (dQ/dV) and differential voltage (dV/dQ) analysis. The strengths and weaknesses of dQ/dV and dV/dQ analysis will be discussed along with an explanation of how high precision coulometry can be used to augment these measurements. Lastly, a software program developed by the author will be introduced which can be used to interpret dQ/dV and dV/dQ results from Li-ion full cells.

Chapter 7 briefly discusses the other experimental equipment used in this thesis to support the results found using high precision coulometry.

Chapter 8 presents a high precision study of the formation of reduction products on graphite electrodes. The experiment shows that the amount of charge consumed by this layer of reduction products is primarily dependant on time, temperature and the surface area of the graphite electrode. The experiment also shows that the cumulative amount of charge consumed by this layer increases with $time^{1/2}$.

Chapter 9 presents the *capacity* loss and CE of $LiCoO_2$, $LiFePO_4$, $LiMn_2O_4$ and $Li[Ni_{1/3}Mn_{1/3}Co_{1/3}]O_2$/graphite commercial Li-ion batteries as a functions of cycle number. The experiments show that time, not cycle count, is the dominant contributor to the coulombic inefficiency (1-CE) of Li-ion batteries cycled at low rates and high temperatures. Long term cycling of $LiCoO_2$/Graphite commercial cells was also performed to confirm these results.

Chapter 10 shows $LiCoO_2$, $Li[Ni_{⅓}Mn_{⅓}Co_{⅓}]O_2$, and $LiMn_2O_4$/graphite commercial cells cycling between narrow voltage limits on a high precision charger and stored at various open circuit voltages on the automated storage/cycling tester. The experiment shows that narrow range cycling and storage experiments are useful techniques for identifying the relative amount of damage caused at different open circuit voltages in Li ion cells. However, this experiment also shows that these tests do not always identify the same parasitic reactions and should be used in concert to complement each other.

Chapter 11 shows dQ/dV and CE of electrodes mixed with different ratios of $LiMn_2O_4$ and $Li[Ni_{1/3}Mn_{1/3}Co_{1/3}]O_2$. The experiments showed that the addition of even modest amounts of $Li[Ni_{1/3}Mn_{1/3}Co_{1/3}]O_2$ to $LiMn_2O_4$ electrodes produced a significant improvement in *capacity* retention. $Li[Ni_{1/3}Mn_{1/3}Co_{1/3}]O_2$ also helps suppress the loss of Mn from $LiMn_2O_4$, and a correlation between Mn loss, *capacity* retention and CE is shown.

Chapter 12 will summarize and conclude the thesis. It also describes the future of high precision coulometry and gives other examples of how precision coulometry can be used in battery testing.

Chapter 2 Li-Ion Batteries

2.1 Electrode Materials

A Li-ion battery is composed of multiple Li-ion cells. These cells convert chemical potential energy directly to electrical energy through reduction-oxidation (redox) reactions. An electrochemical cell has three basic components; the positive and negative electrodes, where redox reactions occur, and a salt$^-$ containing electrolyte which allows for the transport of ions between the electrodes. In Li-ion cells Li^+ ions move between the two electrodes while an equivalent number of electrons are passed through an external circuit. Since the Li ions are in a state of equilibrium when they are transferred between the electrodes, the only work being done in the cell is done on the electrons. This work can be simply calculated as eV, where e is the magnitude of the charge of an electron and V is the open circuit voltage of the cell. The work done in the cell can also be calculated as the difference in chemical potential, μ, of lithium atoms in the positive electrode and those in the negative electrode

$$eV_{Net} = \mu_{negative} - \mu_{positive}. \qquad 2.1$$

where the charge of an electron is constant. Therefore, the voltage of a cell can be increased by either decreasing the chemical potential of lithium atoms in the positive electrode (higher potentials versus Li/Li^+) or increasing the chemical potential of lithium atoms in the negative electrode (lower potentials versus Li/Li^+). Increasing the voltage of

a cell can be beneficial, because it allows more energy, E, to be stored for the same amount of *capacity*, Q.

$$E = \int_0^{Q_{\max}} V(Q)dQ = \frac{\int_0^{Q_{\max}} V(Q)\,dQ}{\int_0^{Q_{\max}} dQ} * \int_0^{Q_{\max}} dQ = V_{ave} Q_{\max} \quad , \qquad 2.2$$

where V_{ave} is the average open circuit voltage of the cell. Equation 2.2 also shows that if the electrodes are made with materials which can store more charge per unit mass or volume (specific or volumetric *capacities*) this would increase the stored energy of the cell, while operating at the same voltage. There are currently many researchers focused on finding new materials which increase open circuit voltage of the cell and have larger *capacities*, but these are not their only considerations. New electrode materials should also have long cycle life, low toxicity, be cheap to produce and have good safety characteristics.

The majority of positive and negative electrode materials react with lithium through the process of intercalation. Intercalation is a topotactic reaction where lithium atoms are reversibly inserted into and removed from the host material without significantly changing its structure. This lack of change in the host material is beneficial, because it helps to reduce damage to the crystal structure of the host during charge – discharge cycling.

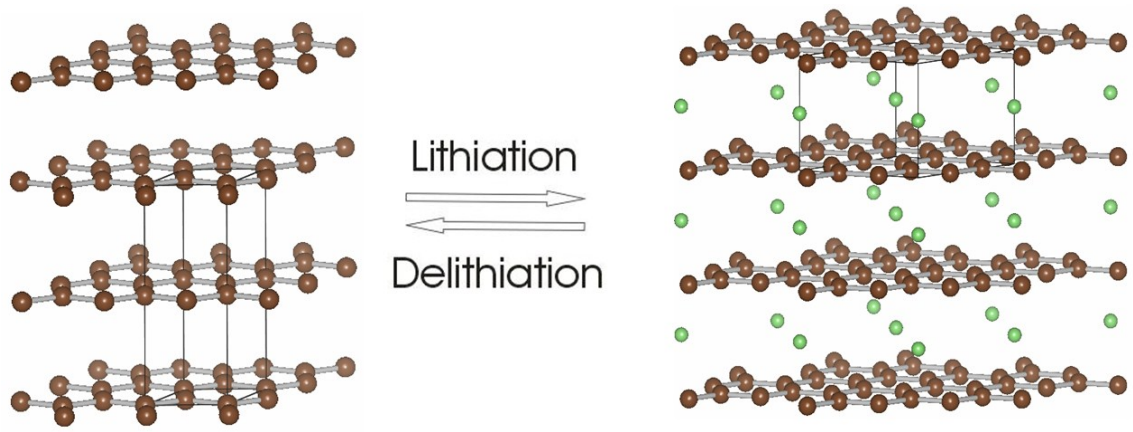

Figure 2.1 The crystal structure of graphite in a fully lithiated and delithiated state. Carbon atoms are brown and lithium atoms are green.

Figure 2.1 illustrates the intercalation and de-intercalation of Li atoms into the layered structure of graphite which is the most common negative electrode material. The intercalation of graphite results in volumetric expansions of ~10% making the process highly reversible and allowing Li_xC_6 to survive thousands of charge / discharge cycles [38]. Other advantages to using graphite are that it intercalates Li atoms at an average potential of 0.1 V versus Li^+/Li (i.e. high chemical potential), is inexpensive and has a specific *capacity* of 372 mAh/g [39].

Figure 2.2 illustrates the intercalation and de-intercalation of lithium in three different positive electrode structures; layered, spinel and olivine. $Li[M]O_2$ (M = Co, Ni, Mn, etc) layered structure materials intercalate Li atoms between MO_2 layers in a manner similar to graphite. The two most frequently used layered structure positive electrode materials are Li_xCoO_2 ($0.5 < x < 1$, 130 ~ 140 mAh/g [40]) and $Li[Ni_{1/3}Mn_{1/3}Co_{1/3}]O_2$ (cycled between 2.5 and 4.4 V - 160 mAh/g [41]). Materials with spinel ($Li[M]_2O_4$, M = Mn, Ni, Co, etc) and olivine structures ($Li[M]PO_4$, M = Fe, Mn, Co, etc) intercalate and de-intercalate Li atoms through tunnels. The most common spinel and olivine structures

used as positive electrode materials are $Li_{(1+x)}Mn_{(2-x)}O_4$ (110 mAh/g [42]) and $LiFePO_4$ (165 mAh/g [43]), respectively.

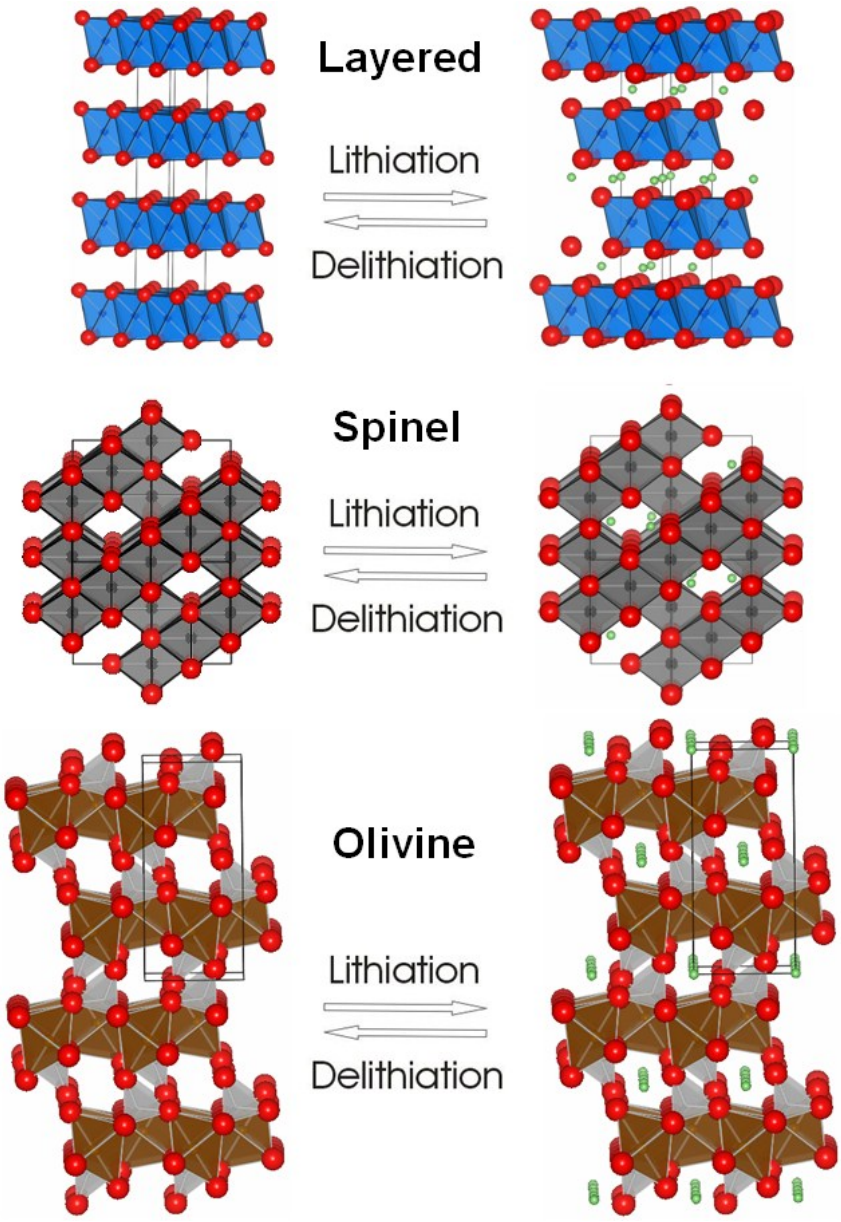

Figure 2.2 The crystal structure of the three most common positive electrode materials in fully lithiated and delithiated states. Oxygen, lithium and phosphorus atoms are always shown in red, green and grey, respectively. Transition atoms are blue in the layered structure, black in the spinel structure and brown in the olivine structure.

2.2 Electrolyte

Electrolytes in Li-ion batteries usually consist of an organic solvent, typically a carbonate, containing free Li^+ which can be transported between the positive and negative electrodes. The most common salt used in Li-ion batteries is lithium hexafluorophosphate ($LiPF_6$) because of its high ionic conductivity (>10^{-3} S/cm), Li ion transference number (0.35) and acceptable safety characteristics [44]. However, $LiPF_6$ is expensive, hygroscopic and has been shown to form hydrofluoric acid (HF) when exposed to water [45]. Thus, other lithium salts have been developed with the aim of improving upon these properties; such as, lithium bis(oxalato)borate ($LiB(C_2O_4)_2$), lithium tetrafluoroborate ($LiBF_4$) and lithium (bis) trifluoromethanesulfonimide ($(LiN(SO_2CF_3)_2$) [46–48].

Solvents used in Li-ion cell electrolytes usually include some kind of carbonate. Carbonates typically have large dielectric constants, greater then 3, which allow for Li salt solutions with concentrations greater then 1 M [49]. The most common carbonates used in Li-ion cells are ethylene carbonate (EC), diethyl carbonate (DEC), dimethyl carbonate (DMC), propylene carbonate (PC) and ethyl methyl carbonate (EMC) [49]. However, in practice the solvents used by battery manufactures are often some combination of the above carbonates, such as EC:DEC (1:2 v:v).

2.3 Common Battery Designs

Li-ion batteries come in two basic designs, wound and stacked cells. Both designs have differences, but the basic cell components used in each one are very similar. Figure 2.3 shows a schematic diagram of the most common wound cell, the 18650 cylindrical cell

(18 mm diameter and 65 mm length). Generally, positive and negative electrodes are made by coating an electrode material on both sides of a thin metal foil, called a current collector. These current collectors are used to provide a low resistance pathway for electrons to travel from the electrode material to the electrode leads connected to the outside of the cell. The double-sided positive and negative electrodes are then stacked on top of each other in alternating layers with a porous member, called a separator, being placed between each layer. The separator acts like an insulating layer, keeping the two electrodes physically separated while the pores inside the separator allow the Li^+ in the electrolyte to be transferred between the electrodes. The battery components are then fit into a casing which provides protection for the electrochemical cell.

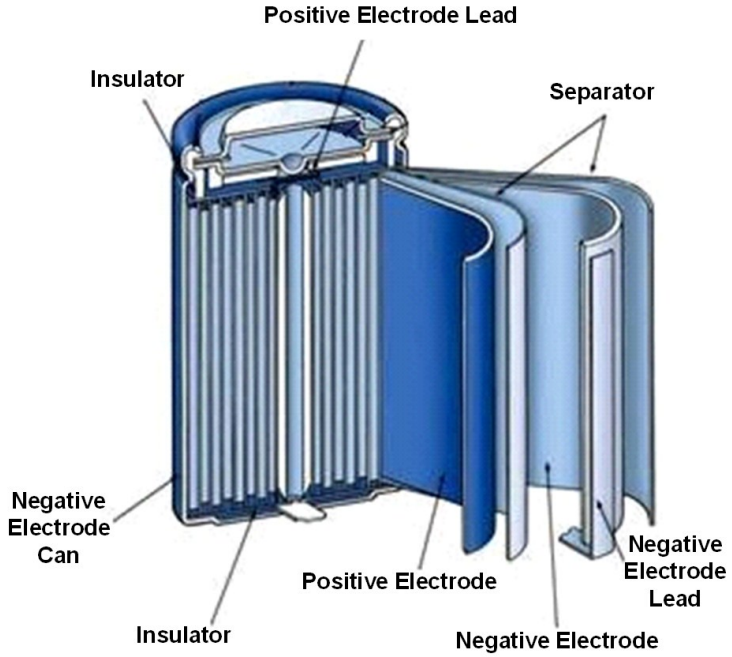

Figure 2.3 Schematic diagram of the internal components of an 18650 cylindrical cell

The difference between wound and stacked cells is how they are constructed. Wound cells are made from long positive and negative electrodes (with a layer of separator between each electrode) wound continuously into a tight roll, as in Figure 2.3.

Stacked cells are made from single sheets of double sided electrodes stacked one on top of another, with a sheet of separator between each layer. Wound cylindrical cells can be made mostly by automation and thus can be made cheaply in an industrial setting. However, the equipment required to properly make wound cells is expensive. Therefore, coin type cells, which require fewer resources, are a more preferable option for smaller laboratories.

Coin cells have the same basic components of the Li ion cells described above (positive and negative electrodes, current collectors, separators, electrolyte and casing) with a few additional pieces. One of the major differences is that coin cells use electrodes cut into small circles (about 1.25 cm^2) and only have electrode material spread on one side of the current collectors. Coin cells can be divided into three categories. Cells that use **different** intercalating materials for the positive and negative electrodes with no reference electrode between them are called "full cells". Cells that use the **same** intercalating material for both electrodes with no reference electrode between them are called "symmetric cells". Cells that use intercalating materials for only the positive (working) electrode while a disk of Li metal is used as the reference/counter (negative) electrode are called "half cells". Half cells are useful devices, because the potential of the Li metal remains constant at 0.00 V versus Li^+/Li during cycling. Thus the potential versus specific *capacity* and other characteristics of the working electrode material can be studied without the interference of the counter electrode. Figure 2.4 shows a diagram of the components of a coin cell. The spacer and spring in the coin cell are used to press the positive and negative electrodes together when the coin cell is sealed.

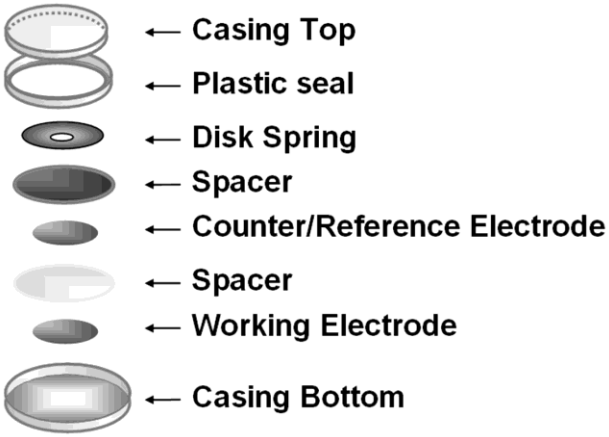

Figure 2.4 Diagram of the components in a coin type cell.

2.4 Electrochemical Behavior of Li-Ion Cells

When cycling half cells Li ions are moved between the working electrode and the Li disk acting as the counter electrode. During charge Li ions and a corresponding number of electrons are removed from the working electrode increasing its potential. During discharge Li ions and electrons are inserted into the working electrode decreasing its potential. Assuming the applied current, I_A, used to drive Li^+ and electrons between the two electrodes is known and constant then the *capacity* of the cell can be determined by

$$Q_o = \int_0^t I_A(t') * dt' = I_A * t \qquad 2.3$$

where t is the measured time of the charge or discharge. In this thesis the word "capacity" has several meanings which can normally be taken from context. However, in an attempt to reduce confusion for non-specialist readers, a distinction will be made in notation used to describe different meanings of the word "capacity". Until this point

capacity has referred to the total capacity of a cell or specific capacity of a material being cycled between fixed voltage limits and is measured in units of mAh or mAh/g respectively. When capacity is used in this way or any way in which term capacity could be referred to as a dependent variable it will be italicized. Capacity can also be used as an independent variable to specify the state of charge of an electrode or cell. For example, when cell potential, V, is specified as a function of electrode capacity (proportional to state of charge), Q, as the function, V(Q), such as in Figure 2.5, it will not be italicized.

By convention, positive electrodes increase in capacity during charge (de-lithiation) and decrease in capacity during discharge (lithiation). Conversely, negative electrodes increase in capacity during discharge (lithiation) and decrease in capacity during charge (de-lithiation). This is a useful convention because during the cycling of a full cell one electrode will always be lithiated and the other will be delithiated. During charge Li^+ and electrons are transferred from the positive to the negative electrode and during discharge Li^+ and electrons are transferred from the negative to the positive electrode.

Figure 2.5 shows the potential versus capacity of Li_xCoO_2/Li, Li_xFePO_4/Li and Li_xC_6/Li half cells. The masses of the working electrodes have been balanced so the *capacities* of the cells equal 100 mAh. Figure 2.5 shows that the voltage of a full cell is determined by the difference in potential between the positive and negative electrodes. This means that the higher potentials of the Li_xCoO_2/Li half cell over the Li_xFePO_4/Li half cell will result in larger voltages for Li_xCoO_2/ Li_xC_6 full cell (V_2) than a Li_xFePO_4/ Li_xC_6 full cell (V_1). As stated before, increasing the voltage of a cell allows more energy

to be stored for the same amount of *capacity*. Thus, using a Li_xCoO_2 electrode over a Li_xFePO_4 electrode would increase the energy of the cell. However, operating a Li-ion cell at higher open circuit voltages can also induce various unwanted reactions inside the cell which can reduce its cycle life (see chapter 3). Thus based on the requirements of the full cell the potential difference between the electrodes needs to be carefully selected.

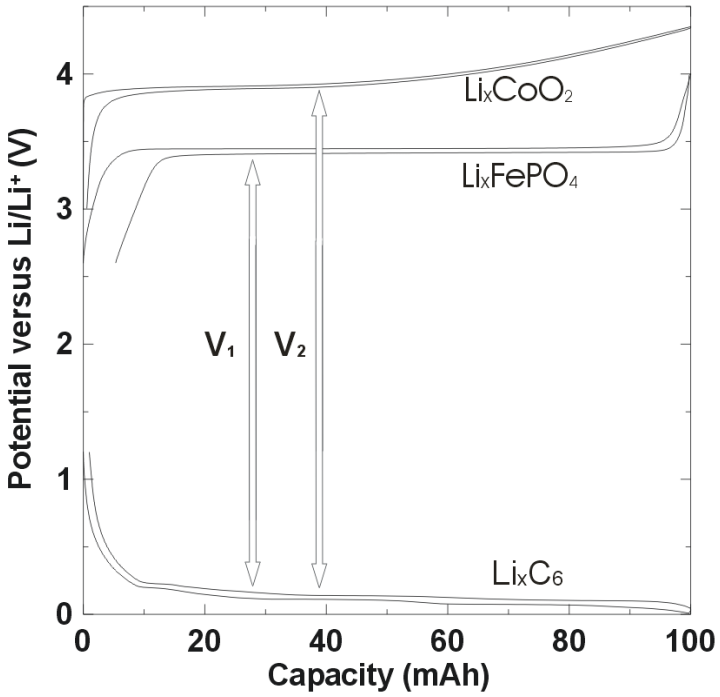

Figure 2.5 Potential versus capacity for Li_xCoO_2/Li, Li_xFePO_4/Li and Li_xC_6/Li half cells. The masses of the working electrodes have been balanced so the *capacities* of the cells would equal 100 mAh.

Chapter 3 Li-Ion Accounting

3.1 A Li Accounting Model

The cycle life of a Li-ion cell is not infinite because small fractions of cell materials are consumed by parasitic reactions during each cycle. These unwanted reactions can occur by a number of different processes.

1) Li loss at the negative electrode through SEI growth and repair.
2) Electrolyte oxidation at the positive electrode resulting in a salt depletion or producing a continuous shuttle mechanism.
3) Dissolution of transition metal ions from the positive electrode and subsequent deposition on the negative electrode.
4) Positive electrode damage resulting in trapped Li within the electrode.
5) Other

Each of these reactions affects the *capacity* fade and CE of a cell in different ways. Other authors, most notably Newman et al. [50,51], have suggested that with careful models one can determine how much active lithium the above reactions will consume. However, in their papers they use calculations to provide a general understanding of the different *capacity* loss mechanisms and then represent these losses, and how they relate to each other, in terms of visual models. Here a model for Li accounting is proposed, which follows **all** the active lithium that is passed between the positive and negative electrodes and lost to parasitic reactions in clearly defined equations and tables. The effect of these

reactions on the electrochemical behavior of a Li-ion cell is then quantified in parameters which can be measured by the High Precision Charger.

3.2 Solid Electrolyte Interphase Growth and Repair

During each charge – discharge cycle of the negative electrode a small amount of active Li in the cell is used to form (and thicken) a passivating layer on the surface of the electrode, known as the SEI. The exact nature of the SEI is dependent on a number of factors such as the active material in the electrodes [49], electrolyte composition [52–54], temperature of the cell [36,55,56], electrolyte additives [57,58], etc. Although the SEI can change dramatically depending on the parameters of the cell, there are two things that all SEIs have in common; the Li used to form the SEI is always consumed **irreversibly** and the SEI is considered to be an electronically insulating layer. Thus, in order for an electrolyte molecule to react with a Li^+ and an e^- it will have to come close enough to the Li_xC_6 to be within a tunneling range of an e^- [59]. This presumably requires an electrolyte molecule to diffuse through the SEI to get within a required range, significantly reducing the SEI growth rate as the SEI thickens.

Figure 3.1 shows four schematic diagrams depicting possible SEI formation routes on the negative electrode. Figure 3.1A shows that during discharge a Li^+ traveling through the electrolyte can help form a new SEI layer on the old SEI surface if an e^- can tunnel from the electrode to meet it. Figure 3.1B shows that a Li^+ and an e^- in the negative electrode can also react with electrolyte to form a new SEI layer. Figure 3.1C shows a situation where new SEI forms within the SEI due to diffusion of electrolyte within the SEI. The new SEI then pushes out the old SEI layer and increases the total

width of the layer. Figure 3.1D shows a situation where impurities in the electrolyte damage the surface of the SEI, requiring a fresh SEI layer to be formed to fill in the gaps. It really does not matter which scenario from Figures 3.1A-D (or other scenarios not shown) is chosen for the formation of the SEI as long as the Li atoms incorporated within the SEI are irreversibly lost from the total number of Li^+ which can be exchanged between the electrodes.

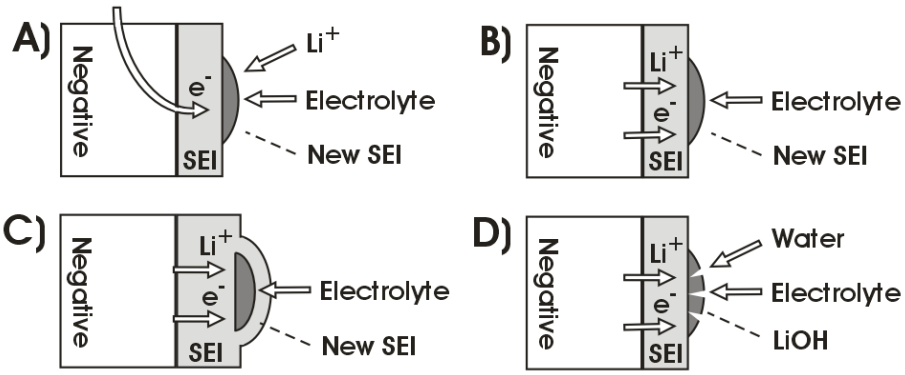

Figure 3.1 Schematic diagrams of different SEI formation routes.

There is an effective parasitic current, I_{Li}, which adds Li atoms to the SEI. During each half cycle, an amount of charge, q_{Li},

$$q_{Li} = \int I_{Li}\, dt = I_{Li}^{av}\, \Delta t \qquad 3.1$$

becomes inactive as it is consumed by the SEI. In this expression, I_{Li}^{av} is the average parasitic SEI-forming current. Normally, I_{Li} and q_{Li} decrease with cycle number as the SEI thickens [36,59].

Equations 3.1 and 2.3 are similar to each other in form but different because in Equation 3.1 I_{Li} is not known. However, Equations 3.1 and 2.3 can be solved to find

$$q_{Li} = Q_o \, I_{Li}^{av} / I_A. \qquad 3.2$$

3.3 Electrolyte Oxidation and Shuttle Mechanisms

Equation 2.1 and Figure 2.5 show that by increasing the potential difference between the positive and negative electrodes the open circuit voltage and energy density of the full cell could be increased. This is one reason why Li metal oxides such as $LiCoO_2$ (nominal potential of 4.0 V) and $LiMn_2O_4$ (nominal potential of 4.1 V) are often used as positive electrodes. However, these large potentials can cause electrolyte oxidation which can affect the lifetime of the cell. The rate of electrolyte oxidation in a Li ion cell can be affected by many different things; the type of positive electrode being used [13,60], the upper cutoff potential, the electrolyte chemistry [61], temperature of the cell [37] and the surface layers formed on both electrodes [62].

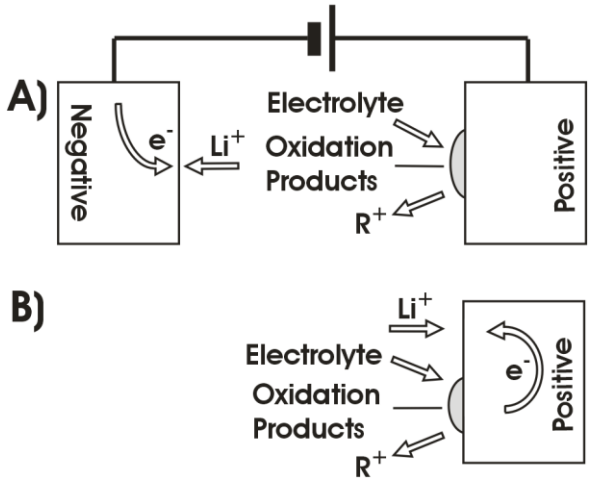

Figure 3.2 Schematic diagrams of electrolyte oxidation routes at the positive electrode.

Figure 3.2 shows schematic diagrams illustrating two possible electrolyte oxidation routes at the positive electrode. During each half cycle a certain amount of electrolyte oxidizes, possibly depositing insoluble reaction products on the surface of the positive electrode. The reactions products then transfer an equivalent amount of e^- and R^+ (could be H^+) to the positive electrode and electrolyte respectively. These e^- can remove Li^+ from the electrolyte by charge neutrality and transfer them into either the negative (Figure 3.2A) electrode if the cell is connected to a charger or the positive (Figure 3.2B) electrode if the cell is under open circuit conditions. Unlike the SEI formation, electrolyte oxidation as depicted in Figure 3.2 removes Li^+ ions from the electrolyte and adds them to the inventory of active Li in the cell as long as R^+ stays in solution. The related parasitic current and charge per half cycle are called I_{ox}^a and q_{ox}^a. I_{ox}^a is taken here to be the average oxidation current in the potential range during cycling. Continued electrolyte oxidation as in Figure 3.2 will eventually lead to a depletion of all the Li^+ in the electrolyte and as a consequence the cell will die. As in equation 3.2, the *capacity*, q_{ox}^a, can be related to the parasitic current, I_{ox}^a, by

$$q_{ox}^a = Q_o \, I_{ox}^a / I_A \qquad 3.3$$

Figure 3.3 shows five schematic diagrams of different electrolyte oxidation processes all known as shuttle mechanisms. As in Figure 3.2 electrolyte molecules in Figures 3.3A, 3.3B, 3.3C and 3.4D are oxidized at the positive electrode, but then the radical cations travel to the negative electrode where they are reduced again. In Figures 3.3A and 3.3B the reduction process is shown to be reversible and the electrolyte

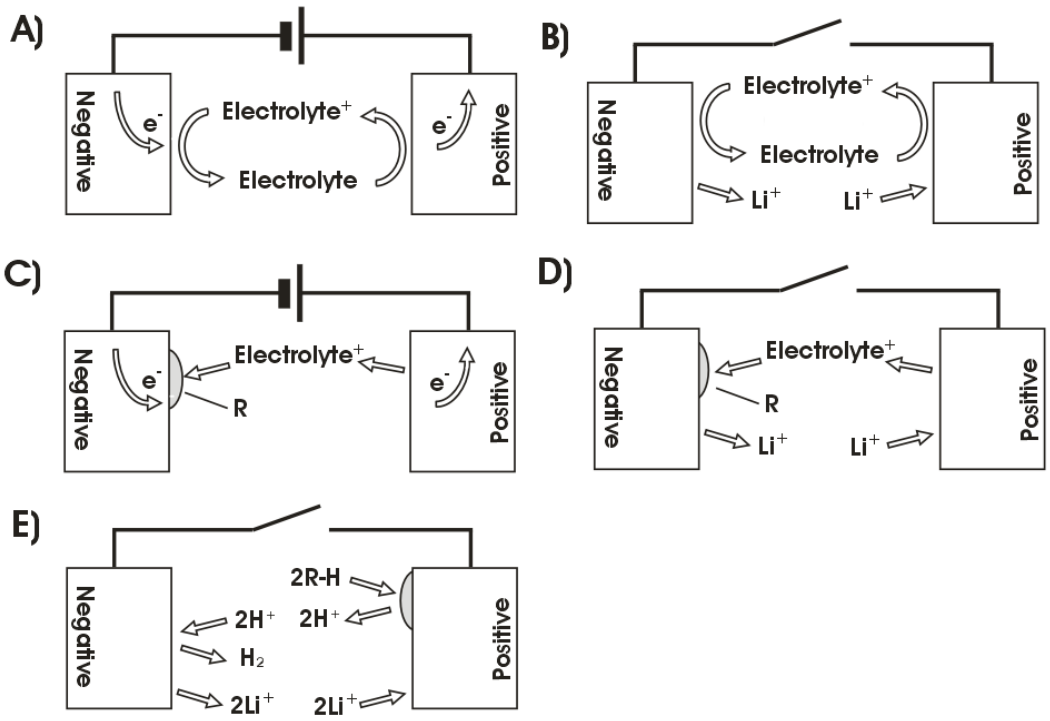

Figure 3.3 Schematic diagrams of different electrolyte shuttle mechanisms.

molecules are reformed. However, only for very special molecules is this highly reversible [61]. It is more likely that a reduction product, R, will remain at the negative electrode as in Figure 3.3C and 3.3D, hence consuming electrolyte. In Figure 3.3A and 3.3C this process does not result in a depletion of the Li^+ in the electrolyte or a change in the Li content of either electrode if the cell is held at a fixed potential. However, if the cell is under open circuit conditions, an electrolyte shuttle can remove Li from the negative electrode and add it to the positive electrode as shown in Figures 3.3B and 3.3D. Figure 3.3E shows an alternative situation where a polymerized species is formed by oxidation at the positive electrode. This reaction involves protons traveling through the electrolyte to the negative electrode to be reduced to hydrogen gas. The reaction is then balanced by moving an equivalent number of Li^+ to the positive electrode. I_{ox}^{b} is the

average current over a half cycle associated with shuttle mechanisms and q_{ox}^{b} is the associated charge, which can be related to each other by

$$q_{ox}^{b} = Q_o I_{ox}^{b}/I_A \qquad 3.3$$

3.4 Transition Metal Dissolution

The chemical and structural stability of a positive electrode can dramatically affect the cycle life and storage performance of a Li-ion cell. For example, at higher potentials transition metals in the positive electrode can be oxidized into cations which can dissolve into the electrolyte. Transition metal dissolution has been observed for many types of oxide materials, such as $LiCoO_2$ [63,64], $LiFePO_4$ [65], $Li[Ni_{1/3}Mn_{1/3}Co_{1/3}]O_2$ [66] and $LiMn_2O_4$ [67,68]. In the more severe cases of metal ion dissolution, these processes produce structural degradations of the oxide material and can result in positive electrode *capacity* loss.

Figure 3.4 shows a schematic diagram of two transition metal dissolution processes. During each half cycle a certain amount of transition metal ions, M^{2+}, are dissolved into the electrolyte and migrate towards the negative electrode. Upon arriving at the negative electrode the metal ions are reduced and are deposited as M atoms on the electrode surface. In order to reduce these ions an equivalent amount of the charge must also be transferred. This can be done in one of two ways: moving electrons from the positive to the negative electrode (Figure 3.4A) or moving Li^+ from the negative electrode into the vacancies left by the metal ions in the positive electrode (Figure 3.4B).

Like the shuttle mechanism above, described by Figure 3.3, this process moves charge without changing the amount of active Li in the cell. Therefore, the effects of this process are included in I_{ox}^{b} and q_{ox}^{b}.

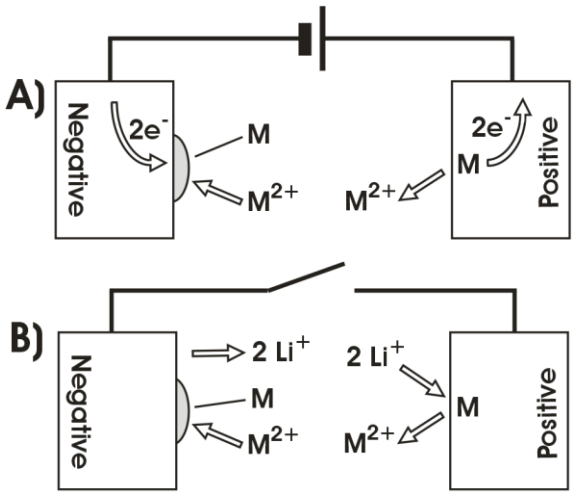

Figure 3.4 Schematic diagrams of transition metal dissolution in a Li ion cell.

3.5 Positive Electrode Damage

The insertion and extraction of Li^+ from Li metal oxides can lead to changes in the molar volume and phase of the positive electrode material [69]. Both of these processes have the ability to induce mechanical stress and strain on the crystal structure of the oxide particles. In severe cases this might lead to cracks and electrical isolation of some of the active material. Additionally, metal ion dissolution can also cause a *capacity* reduction in the positive electrode. In the case of $Li_{(1+x)}Mn_{(2-x)}O_4$, Mn ions can be dissolved from the positive electrode resulting in a phase with a larger lithium content and smaller *capacity* [69]. Both of these processes limit the ability of the positive electrode to deliver the same amount of Li^+ as it did during its initial charge. A *capacity*, q_p, of Li is assumed

to be trapped in the positive electrode during each half cycle. This *capacity* can be related to an average parasitic current, I_p, by

$$q_p = Q_o \, I_p / I_A \qquad 3.5$$

3.6 Li Accounting in a Li-Ion Cell

To keep track of the effects of the various parasitic processes described above, an inventory of all the active lithium in a Li-ion cell needs to be maintained. Figure 3.5 shows the potential versus capacity of the positive and negative electrodes in two hypothetical Li_xCoO_2 / Li_xC cells during the first cycle. The positive electrode in Cell A and the negative electrode in Cell B have larger irreversible *capacities* (IRC) than the other electrodes in the cells. These larger IRC also cause the potential-capacity profiles of the affected electrodes to shift to higher relative capacities and limit the *capacity* of the cell at the bottom of discharge. One possible example of a cell similar to Cell A is a $Li_x[Ni_{0.425}Mn_{0.425}Co_{0.425}]O_2/Li_xC_6$ cell. $Li_x[Ni_{0.425}Mn_{0.425}Co_{0.15}]O_2$/Li half cells have been shown to have IRC as large as 11% during the first cycle which is noticeably larger than the <7 % IRC for Li_xC_6/Li half cells [49,70]. However, Li_xCoO_2/Li half cells have been shown to have IRC as low as 5% which is smaller than the IRC of the Li_xC_6 electrode and thus Li_xCoO_2/Li_xC_6 would be a good example of Cell B [71].

Figure 3.6 shows the potential versus capacity of the same electrodes in Figure 3.5 after several cycles. It is assumed that the potential of the negative remains at about 0.15V during cycling, therefore changes in voltage profile of a full cell will be dominated

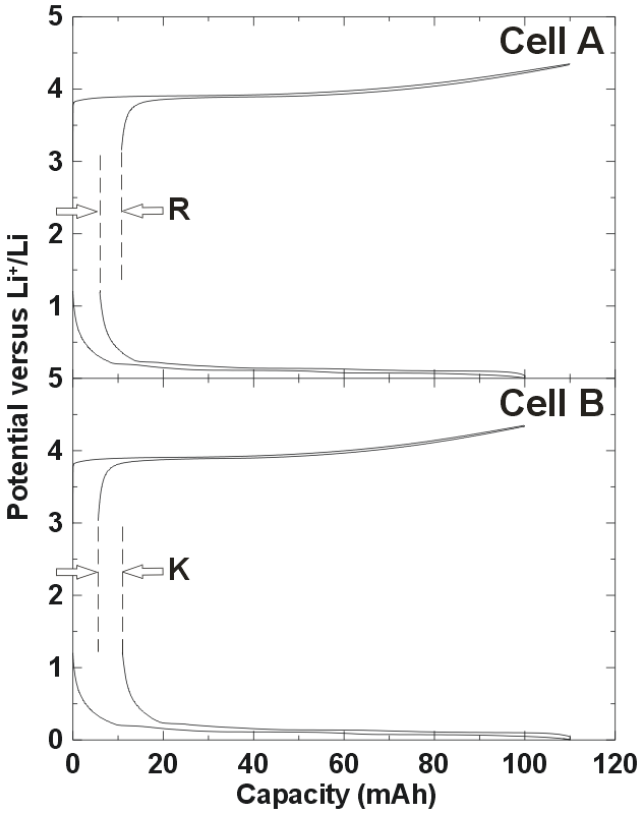

Figure 3.5 Potential versus capacity of the positive and negative electrodes in two hypothetical Li_xCoO_2 / Li_xC cells during the first cycle.

by the positive electrode. In both scenarios Q_o is equal to the amount of active lithium (i.e. *capacity*) the positive electrode will initially delithiate in order for the full cell to reach the upper voltage limit. The potential of the positive electrode at the top of charge should be fairly consistent with cycling, because the potential of the negative electrode has been assumed to be roughly constant. Figure 3.6 shows that because of the initial IRC in Cell A the Li_xCoO_2 is completely filled with active lithium at the bottom of discharge, leaving a *capacity*, R, of active lithium in the graphite electrode. Figure 3.6 also shows that at the bottom of discharge of Cell B the graphite electrode contains no active lithium and a *capacity*, K, is still available to receive additional active lithium in the Li_xCoO_2 electrode.

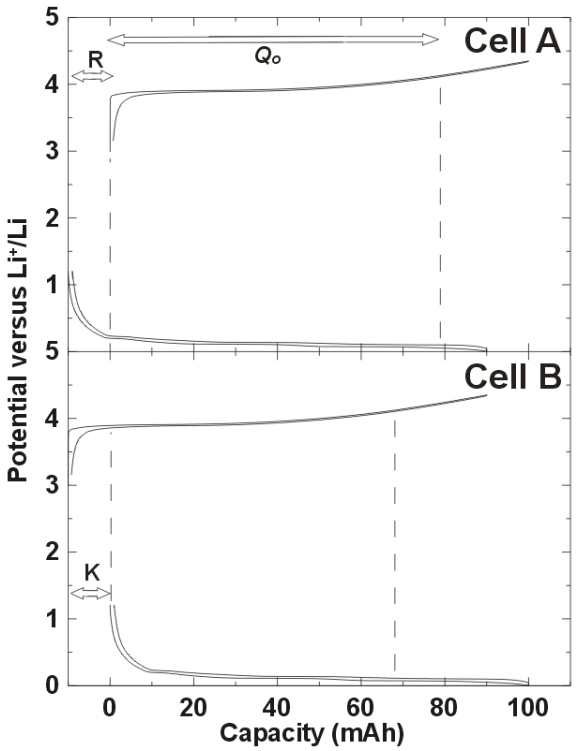

Figure 3.6 Potential versus capacity of the positive and negative electrodes in two hypothetical Li_xCoO_2 / Li_xC cells. When the full cell reaches the bottom of discharge; the negative electrode is completely emptied of active lithium (Cell A) or the positive electrode is completely full of active lithium (Cell B).

Figure 3.7 shows the potential versus capacity of the positive and negative electrodes in a hypothetical Li_xCoO_2 / Li_xC cell (Cell C) cycling between narrow voltage limits. As in Figure 3.6 it is assumed that the voltage of the full cell is dominated by the positive electrode, because the potential of the negative electrode remains fairly constant with state of charge especially over a narrow voltage range. It is also assumed that Q_o is equal to the *capacity* of the positive electrode when the upper voltage limit is reached. What is unique about Cell C is that the cell has no *capacity* limiting electrode at the bottom of discharge. When the lower voltage limit is reached a *capacity*, R, remains in

the negative electrode and a *capacity*, K, is still available in the positive electrode for additional lithium. Cell C can be considered a general case between Cell A and Cell B.

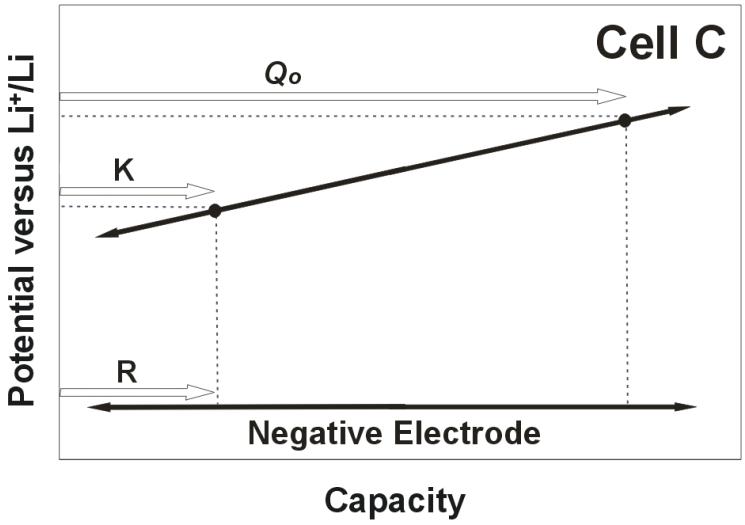

Figure 3.7 Potential versus capacity of the positive and negative electrodes in a hypothetical Li_xCoO_2 / Li_xC cell cycling between narrow voltage limits.

For the purposes of lithium accounting it is assumed that Cell A, B and C have completed a single formation cycle (i.e. the first charge and discharge of the cell) and have finished in a completely discharged state.

After the formation cycle is completed the number of Li atoms or Li^+ in the electrodes, SEI and electrolyte of Cell B are initialized with the values of:

Active Li in the positive electrode: Q_o - K

Li^+ in the electrolyte: E

Inactive Li in the SEI: S

Active Li in the negative electrode: 0

Sum: Q_o – K + E + S,

where E and S are the *capacities* (in coulombs or mAh) of Li^+ and Li in the electrolyte and SEI respectively. The *sum* shows that the total amount of Li found in Cell B is simply equal to Q_o – K + E + S.

Cell B is then charged, transferring most of the active Li from the positive electrode to the negative electrode. The remaining Li atoms or ions have been affected by one of the processes mentioned in sections 3.2, 3.3 or 3.4 and have been relocated accordingly. After this first charge is completed the Li is distributed as follows

Trapped Li in the positive electrode: q_p

Active Li in the positive electrode: 0

Li^+ in the electrolyte: E - q_{ox}^a

Inactive Li in the SEI: S + q_{Li}

Active Li in the negative electrode: Q_o – K – q_{Li} + q_{ox}^a - q_p

Sum: Q_o – K + E + S

Once again, the *sum capacity* is still equal to Q_o – K + E + S, showing that all of the Li atoms or ions in the cell can be accounted for. This allows the impact of the various parasitic processes to be quantified. Shuttle type mechanisms were not included in this *capacity* inventory because they do not add or remove Li atoms from the pool of active Li atoms. However, they will be included later because I_{ox}^b does affect coulombic efficiency and electrode *capacity* endpoint slippage.

Table 3.1 shows the continued Li inventory of Cell B for the first 1½ cycles. During each half cycle, the number of active Li atoms in the cell changes due to the

processes of SEI formation, electrolyte oxidation and positive electrode damage. The *sum* of all Li atoms or ions in the cell remains constant, as it must, even after continued cycling. Table 3.1 also shows the cycle *capacity* of the cell for each half cycle, to illustrate the effect that the different processes mentioned above have on the observed cell *capacity*.

Table 3.1 *Capacity* inventory of Cell B in Figure 3.6 for the first 1½ cycles

	Initial State	**First Charge (Q_c)**	**First Discharge (Q_d)**	**Second Charge ($Q`_c$)**
Electrolyte	E	$E - q^a_{ox}$	$E - 2q^a_{ox}$	$E - 3q^a_{ox}$
Pos. Electrode	$Q_o - K$	q_p	$Q_o - K - 2q_{Li} - 2q^a_{ox}$	$3q_p$
Active Li in Neg. Electrode	0	$Q_o - K - q_{Li} + q^a_{ox} - q_p$	0	$Q_o - K - 3q_{Li} + 3q^a_{ox} - 3q_p$
SEI	S	$S + q_{Li}$	$S + 2q_{Li}$	$S + 3q_{Li}$
SUM	$Q_o - K + E + S$	$Q_o - K + E + S$	$Q_o - K + E + S$	$Q_o - K + E + S$
Cycle *Capacity*		$Q_o - K + q^a_{ox} - q_p$	$Q_o - K - 2q_{Li} + 2q^a_{ox} - q_p$	$Q_o - K - 2q_{Li} + 3q^a_{ox} - 3q_p$

Table 3.2 shows the Li inventory of Cell A, in Figure 3.6, for the first 1½ cycles, compiled in manner similar to Cell B. As in Table 3.1, the *sum* of all the Li atoms or Li^+ in the cell remain constant throughout cycling. The Li inventories for the first and second charge change by consistent amounts between Tables 3.1 and 3.2. This suggests that as long as the positive electrode is the limiting electrode at the top of charge, the amount of active lithium lost from each electrode will be the same for each scenario. There are a few significant differences between the two tables. At the bottom of discharge, the negative electrode in Cell B is completely empty (Q = 0) and the positive electrode in Cell A is completely filled (a *capacity* of Q_o). This returns the amount of active lithium in

those electrodes to its initial state. However, the amounts of lithium in the opposing electrodes have changed by $2q^{a}_{ox} - 2q_{Li}$ after one cycle.

Table 3.2 *Capacity* inventory of Cell A in Figure 3.6 for its first 1½ cycles.

	Initial State	**First Charge (Q_c)**	**First Discharge (Q_d)**	**Second Charge ($Q`_c$)**
Electrolyte	E	$E - q^{a}_{ox}$	$E - 2q^{a}_{ox}$	$E - 3q^{a}_{ox}$
Pos. Electrode	Q_o	q_p	Q_o	$3q_p$
Active Li in Neg. Electrode	R	$Q_o + R - q_{Li} + q^{a}_{ox} - q_p$	$R - 2q_{Li} + 2q^{a}_{ox}$	$Q_o + R - 3q_{Li} + 3q^{a}_{ox} - 3q_p$
SEI	S	$S + q_{Li}$	$S + 2q_{Li}$	$S + 3q_{Li}$
SUM	$Q_o + R + E + S$	$Q_o + R + E + S$	$Q_o + R + E + S$	$Q_o + R + E + S$
Cycle *Capacity*		$Q_o + q^{a}_{ox} - q_p$	$Q_o - q^{a}_{ox} - q_p$	$Q_o + q^{a}_{ox} - 3q_p$

Table 3.3 *Capacity* inventory of Cell C in Figure 3.7 for its first 1½ cycles.

	Initial State	**First Charge (Q_c)**	**First Dis. (Q_d)**	**Second Charge ($Q`_c$)**
Electrolyte	E	$E - q^{a}_{ox}$	$E - 2q^{a}_{ox}$	$E - 3q^{a}_{ox}$
Pos. Electrode	$Q_o - K$	q_p	$Q_o - K$	$3q_p$
Active Li in Neg. Electrode	R	$Q_o - K + R - q_{Li} + q^{a}_{ox} - q_p$	$R - 2q_{Li} + 2q^{a}_{ox}$	$Q_o - K + R - 3q_{Li} + 3q^{a}_{ox} - 3q_p$
SEI	S	$S + q_{Li}$	$S + 2q_{Li}$	$S + 3q_{Li}$
SUM	$Q_o - K + R + E + S$	$Q_o - K + R + E + S$	$Q_o - K + R + E + S$	$Q_o - K + R + E + S$
Cycle *Capacity*		$Q_o - K + q^{a}_{ox} - q_p$	$Q_o - K - q^{a}_{ox} - q_p$	$Q_o - K + q^{a}_{ox} - 3q_p$

Table 3.3 shows the Li inventory of Cell C, in Figure 3.7, for the first 1½ cycles compiled in manner similar to Cell B. As was the case for Cells A and B the *sum* of all the Li atoms or Li^+ in the cell remain constant throughout cycling. A quick comparison of Tables 3.2 and 3.3 shows that Cell A is simply a limiting case of Cell C, where K = 0.

Tables 3.1 to 3.3 show that, unlike Cell B, the cycle *capacities* of Cell A and Cell C are not affected by q_{Li}. This suggests that if the negative electrode is not the limiting electrode at the bottom of discharge then the lithium lost to the SEI will not affect the cycle *capacity* of the cell, at least in the early cycles. Tables 3.1 to 3.3 also show that the effect of q_{ox}^{a} on cycle *capacity* is different for Cell B. As electrolyte oxidation adds lithium to the positive electrodes (Figure 3.2B) in Cell A and C this leaves a *capacity* of q_{ox}^{a} in the negative electrode which is no longer needed. This additional lithium extracted from the electrolyte also causes the charge *capacity* to increase and the discharge *capacity* to decrease by q_{ox}^{a} to compensate. However, when Cell B is completely discharged and the negative electrode is emptied, the extra *capacity* left in the negative electrode because of electrolyte oxidation can be recovered.

Figure 3.8 shows a schematic diagram of the potential-capacity relation of a Li-ion cell. The horizontal axis tracks the cumulative capacity of the cell. Therefore, if the charge and discharge *capacities* do not exactly match due to the parasitic currents above, the curves shift (referred to as endpoint slippage) sequentially from one cycle to the next. Generally, the more the curves slip to the right the more parasitic reactions have occurred. Figure 3.8 shows the slippages per cycle at the top of charge, Δ_C, and the bottom of discharge, Δ_D, for the first 1½ cycles of a Li-ion cell.

The following mathematical treatments will be in terms of Table 3.1, where the negative electrode in the cell is completely emptied of active lithium at the bottom of discharge. However, an equivalent mathematical treatment for Cell A and C will be included later in Appendix A.

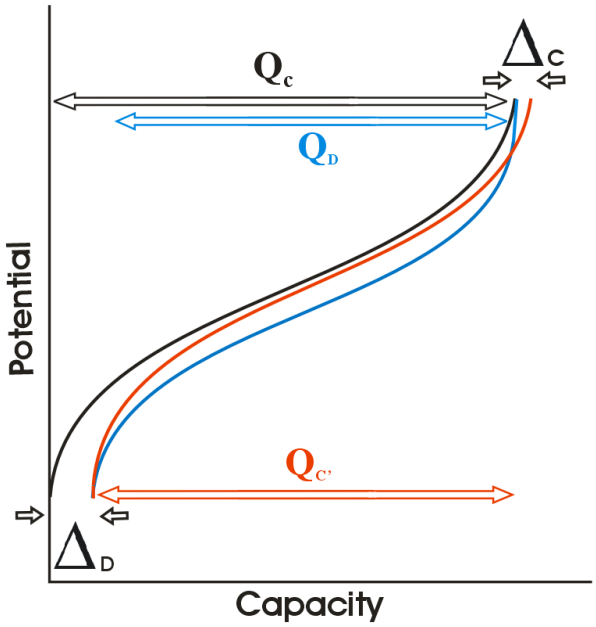

Figure 3.8 An illustration depicting the discharge endpoint slippage (Δ_D) and charge endpoint slippage (Δ_C) of a Li ion cell.

Using the calculated *capacities* in Table 3.1, Δ_C and Δ_D can be expressed as:

$$\Delta_C = Q`_c - Q_d = Q_o - 2q_{Li} + 3q_{ox}^a - 3q_p - Q_o + 2q_{Li} - 2q_{ox}^a + q_p$$

$$\Delta_C = q_{ox}^a - 2q_p \qquad (3.6)$$

and

$$\Delta_D = Q_c - Q_d = Q_o + q_{ox}^a - q_p - Q_o + 2q_{Li} - 2q_{ox}^a + q_p$$

$$\Delta_D = 2q_{Li} - q_{ox}^a \qquad (3.7)$$

where Q_d is the discharge *capacity* of the cell and Q_c and $Q`_c$ are the charge *capacities* immediately preceding and following Q_d, respectively. The *capacity* fade per cycle of a Li-ion cell can also be determined by subtracting Equation 3.6 from Equation 3.7, to give:

$$\text{Fade} = \Delta_D - \Delta_C = 2q_{Li} - 2q_{ox}^a + 2q_p \qquad (3.8)$$

Here we define the CE of a Li-ion cell as the discharge *capacity*, Q_d, divided by the charge *capacity*, Q_c, immediately preceding it. Using the information in Table 3.1, one obtains:

$$CE = \frac{Q_d}{Q_c} = \frac{Q_o - 2q_{Li} + 2q_{ox}^a - q_p}{Q_o + q_{ox}^a - q_p} \tag{3.9}$$

$$CE \approx 1 - \frac{2q_{Li}}{Q_o} + \frac{q_{ox}^a}{Q_o} = 1 - \frac{\Delta_D}{Q_o} \tag{3.10}$$

where Equation 3.10 is a first order approximation of Equation 3.9. Equation 3.10 also shows that CE can be directly related to Δ_D (Equation 3.7) of the cell. The effects of shuttles, involving I_{ox}^b, have not been included in this expression for the CE but will be included later.

Finally, using Equations 3.2 through 3.5 one can rewrite Equations 3.6, 3.7, 3.8 and 3.10 in terms of the parasitic currents:

$$CE = 1 - [2I_{Li} - I_{ox}^a + 2I_{ox}^b]/I_A \tag{3.11}$$

$$\Delta_C = Q_o [I_{ox}^a - 2I_p + 2I_{ox}^b]/I_A \tag{3.12}$$

$$\Delta_D = Q_o [2I_{Li} - I_{ox}^a + 2I_{ox}^b]/I_A \tag{3.13}$$

$$Fade = Q_o [2I_{Li} - 2I_{ox}^a + 2I_p]/I_A \tag{3.14}$$

The parasitic currents associated with I_{ox}^b do not change the amount of active Li in the cell so I_{ox}^b could be easily incorporated into equations 3.11 through 3.14. During each half cycle, they serve to increase the charge *capacity* by $Q_oI_{ox}^b/I_A$ and decrease the discharge *capacity* by $Q_oI_{ox}^b/I_A$. Unfortunately, equations 3.11 through 3.14 can be reduced to only two independent equations with 4 unknowns, thus it is not possible to

solve for the parasitic currents in the general case. However, adding additional information obtained from changes in the differential capacity versus potential of the cell as a function of cycle number allows some of the parasitic currents to be determined.

3.7 Coulombic Efficiency Measurements in Half Cells

When cells are made with a Li metal reference/counter electrode and working electrode which might be used as either the positive or negative electrode in a full cell they are referred to as "positive" or "negative" half cells, respectively. Since parasitic reactions affect the positive and negative half cells in different ways, some of the above equations, intended for full cells, can not be simply applied to them.

Figure 3.9 (top panel) shows the potential versus capacity of a $Li(Ni_{1/3}Mn_{1/3}Co_{1/3})O_2$ positive half cell cycling at a rate of C/10 between 3.0 V and 4.3 V and at a temperature of 30°C. As shown in Figure 3.2B, processes like electrolyte oxidation can cause excess lithium in the cell to be transferred into the positive electrode. As this lithium goes into the electrode it can cause the Q_c of the half cell to be artificially lengthened and Q_d to be shortened. This mismatch between Q_c and Q_d can than cause the voltage profile of the cell to slip to higher relative capacities. If there are no parasitic reactions then Q_c and Q_d would be identical to each other and there would be no electrode slippage. The CE of positive half cells are calculated in the same way as full cells (Equation 3.9)

$$CE_{Pos} = \frac{Q_d}{Q_c}. \tag{3.15}$$

In this way the CE of the positive half cell will always be less than 1.0000. As the CE of the half cell gets closer to 1.0000 this indicates that less electrolyte oxidation (or some other parasitic process) is occurring inside the cell.

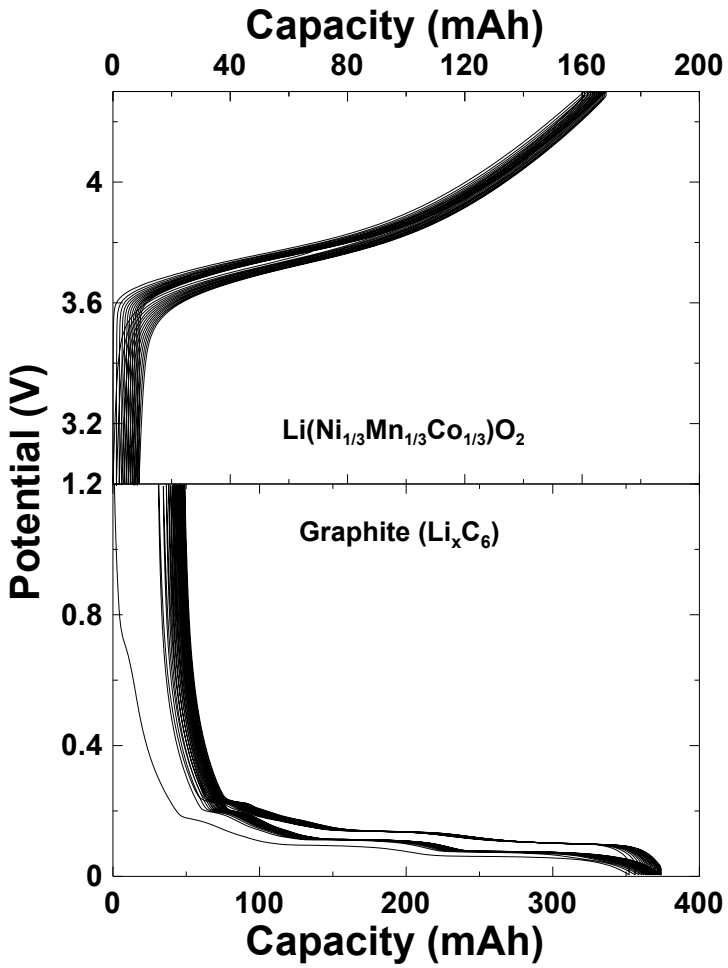

Figure 3.9 Potential versus capacity for the first 20 cycles of a $Li(Ni_{1/3}Mn_{1/3}Co_{1/3})O_2$/Li cell (Top Panel) and Li_XC_6/Li cell (Bottom Panel).

Figure 3.9 (bottom panel) shows the potential versus capacity of a Li_xC_6 negative half cell cycling at a rate of C/20 between 1.2 V and 0.005 V and also at a temperature of 30°C. Due to the low potentials of many negative electrodes, the most predominant parasitic reaction affecting negative half cells is the growth of the SEI. As shown in Figure 3.1 some of the Li^+ being transferred to or from the negative electrode will be

consumed by the SEI. This then requires more Li^+ and electrons to be transferred to the working electrode during discharge (lengthening Q_d) and less Li^+ and electrons being recovered from the working electrode during charge (shortening Q_c). Unlike positive half cells or full cells, the CE of negative half cells are calculated as

$$CE_{Neg} = \frac{Q_c}{Q_d} \tag{3.16}$$

This is a useful convention, ensuring that the CE of negative half cells will also be less than 1.0000.

Chapter 4 High Precision Coulometry

4.1 Requirements for Precision Coulometry Measurements

There are four experimental factors that need to be controlled in order to carefully measure the CE of a Li-ion cell during constant charge – discharge cycling between two voltage limits. These factors are indicated in Table 4.1: (i) error in the delivered current, (ii) error in the measured voltage, (iii) the length of time between voltage measurements and (iv) control of the cell temperature. In order for the CE measurements to be within ±0.01%, it is necessary that I, the measured V, the interval of time between voltage measurements, Δt, and the cell temperature, T, be within the levels outlined in Table 4.1. For estimation purposes in Table 4.1, dQ/dV has been assumed to be Q_o divided by 1 V and dV/dT has been assumed to be 100 μV/K [72].

Table 4.1 Factors which affect the ability to carefully measure coulombic efficiency. For the purposes of these estimates, dQ/dV has been assumed to be the full cell *capacity* in 1 volt and dV/dT has been assumed to be 100 μV/K. ΔQ is the percentage error in the cell *capacity*, ΔI is the percentage error in the current, ΔV is the error of the voltage measurement, Δt is the time interval between voltage measurements and ΔT is the error of the temperature control.

Parameter	Associated Error	Desired Error in Q	For C/10 rate measurements	For C-rate measurement
ΔI	ΔQ = ΔI t	< 0.01%	ΔI < 0.01%	ΔI < 0.01%
ΔV	ΔQ = dQ/dV ΔV	< 0.01%	ΔV < 0.0001V	ΔV < 0.0001V
Δt	ΔQ = I Δt	< 0.01%	Δt < 3.6 s	Δt < 0.36 s
ΔT	ΔQ = dV/dT dQ/dV ΔT	< 0.01%	ΔT < 1K	ΔT < 1K

Figure 4.1 shows an expanded view of the voltage versus time of a Li-ion cell approaching the lower voltage limit. The solid diagonal line represents the true voltage of the cell and the points represent the data as measured by the voltmeter, with the vertical error bars representing the error, ΔV, with which the voltmeter can measure. The data points are equally spaced by a time, Δt. Figure 4.1 demonstrates that the maximum error in measuring charge due to Δt and ΔV is $\Delta Q = I\Delta t$ and $\Delta Q = dQ/dV\ \Delta V$ respectively.

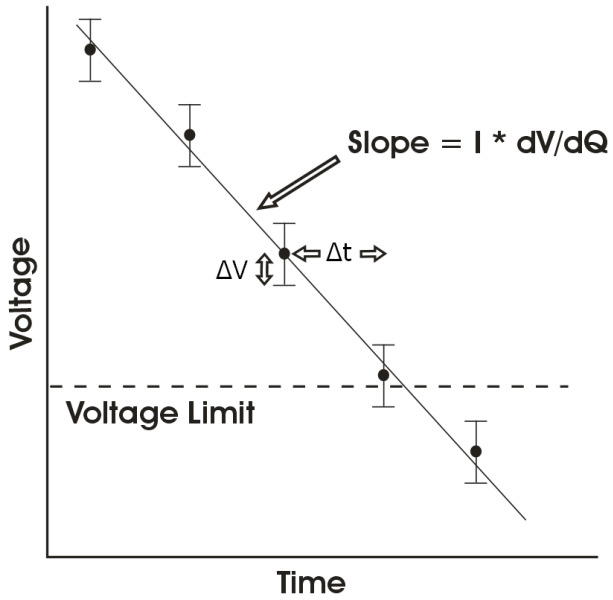

Figure 4.1 Voltage versus time of a Li-ion cell approaching its lower voltage limit. The values, Δt and ΔV, are the time between potential measurements and the precision of the voltage measurement, respectively.

4.2 Commercial Battery Testing Equipment

Table 4.2 compares the specifications of some of the most common battery testing equipment on the market today, which was gathered from either the manufactures websites, by phone or email contact. Table 4.2 suggests that none of the commercially available battery testing systems have the necessary specifications to measure CE to within ±0.01%. The commercial unit with the tightest specification is the Maccor 4000,

which unfortunately lacks the current accuracy required for this level of precision coulometry. In fact, the Maccor system has an error in potential of 153 μV (more than 50% larger than required ΔV suggested in Table 4.1). In fairness to the Maccor 4000, it was designed for a variety of testing protocols, including those which require extremely rapid voltage measurements making it difficult to measure voltage accurately. The remaining battery systems in Table 4.2 have specifications which are not as good as the Maccor 4000, and are thus less capable of accurately measuring CE. Interesting, the best CE measurements we found in the literature were also taken on a Maccor system [31].

Table 4.2 Specifications of commercial charge-discharge equipment obtained from manufacturer's web sites and through phone and e-mail exchange. A 16 bit resolution corresponds to 1 part in 65536 or 1 part in $10^{4.8}$. It is important to realize that even though a 16 bit device is used, the accuracy and stability may not be as good as 16 bits.

Manufacturer	Current Resolution	Voltage Resolution	Current Accuracy	Voltage Accuracy	Time Between Measurements	Error in CE (%)
Maccor 4000 series	16 bit	16 bit	0.02-0.05 % of full scale	0.02 % of full scale	0.01 sec	0.06
Arbin BT2000	16 bit	16 bit	0.02-0.05 % of full scale	0.05% of full scale	0.1 s	0.07
Bitrode MCV	100 nA	100 μV	0.1 % of full scale	0.1% of full scale	0.1 s	0.14
Neware BTS-5V1mA	16 bit	16 bit	0.1% of full scale	0.1% of full scale	1 s	0.14
Lisun PCBT-100-32D	0.10%	0.10%	< 0.5%	< 0.1%	1 s	1.13
Land CT2001	0.10%	0.10%	N/A	N/A	N/A	N/A
Moli	10μA	±10 μV	0.10%	0.01%	150 s	0.43
Biologic VMP	0.00%	16 bit	0.05%	0.10%	0.02 s	0.11
Dalhousie HPC	1 in 19999 (0.005%)	10 μV	0.05 % (over 1 year)	0.0025 % of full scale	< 1 s (by software interpolation)	0.01

4.3 Design of the Dalhousie High Precision Charger

The required specifications outlined in Table 4.1 were considered in our design of the HPC. It was decided to equip each channel with a dedicated precision current source made by Keithley Instruments. The preferred current source was the Keithley 220 despite the fact that it had been replaced by the more modern Keithley 6220. The Keithley 220, which is no longer for sale from Keithley, has the exact same specification as the Keithley 6220 but could be purchased at a quarter of the price. During the American economic down turn of 2009 numerous Keithley 220s were available from various online auction sites (such as www.ebay.com) and electronic refurbishing companies. After an extensive search we were able to purchase 54 Keithley 220s for an average price of $1000 to be used on 50 of the 60 channels used on our current HPC system. The remaining 10 channels were equipped with the more expensive brand new Keithley 6220. Both units communicate via an IEEE interface and have, $\Delta I = \pm 0.05\%$ over 1 year.

The Keithley 220 and 6220 current supplies were calibrated according to the procedures outlined in the instruction manual supplied with the instrument. One of the most important features of the Keithley current sources is that the equality between positive and negative current magnitudes could be carefully controlled. We ensured that the positive and negative currents matched to within 1 part in 10^5 during regular and careful calibrations. Figure 4.2 shows the absolute voltage across a resistor through which an alternating positive and negative current is passed before (top panel) and after (bottom panel) calibration. The red arrows indicate an error in current equality of 0.01%. Since CE is a ratio of the charge and discharge *capacities*, then careful calibrations of the charge and discharge currents are essential for good CE measurements. Keithley's

published specifications for the 220s and 6220s, used to generate the values for the Dalhousie HPC in Table 4.2, do not indicate this fact, which is actually the most important feature for a device designed to measure CE. Furthermore, the Keithley 220 has one current range per decade and the accuracy is ±0.05% of full scale for each range. Most commercial chargers are not equipped with this many current ranges.

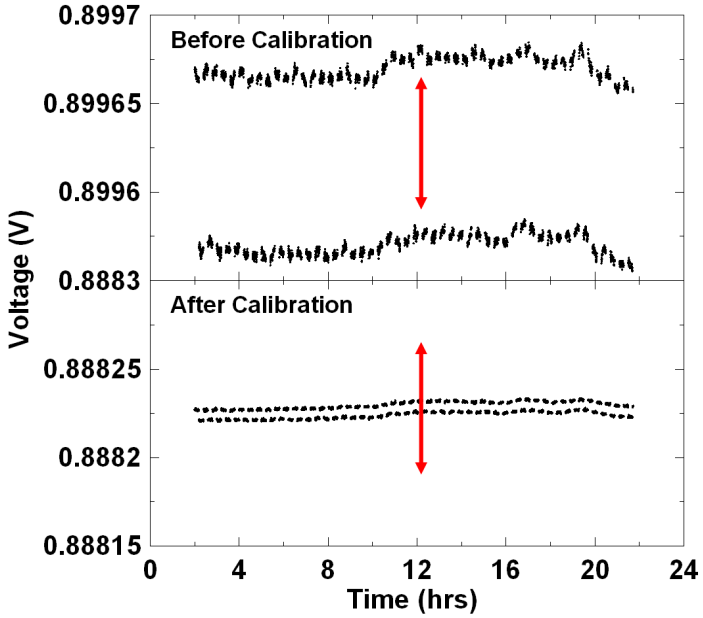

Figure 4.2 The absolute value of the voltage across a resistor with a positive and negative current of equal magnitude alternating every 6 minutes before (top panel) and after (bottom panel) calibration. The red arrows indicate an error in current equality of 1 part in 10,000.

Keithley 2000 scanning-voltmeters were used to monitor the voltage of the cells during cycling. Unlike the current sources which were each assigned to a single channel, the voltmeters were designed to sequentially scan over 10 channels. Thus our 60-channel system had 60 current sources and six Keithley 2000 multimeters. Figure 4.3 shows a photograph of the Dalhousie HPC system. These voltmeters measure 2 V < V < 5 V to a precision of 10 μV and 0.2 V < V < 1.99 V to a precision of 1 μV satisfying the requirements for ΔV given in Table 4.1.

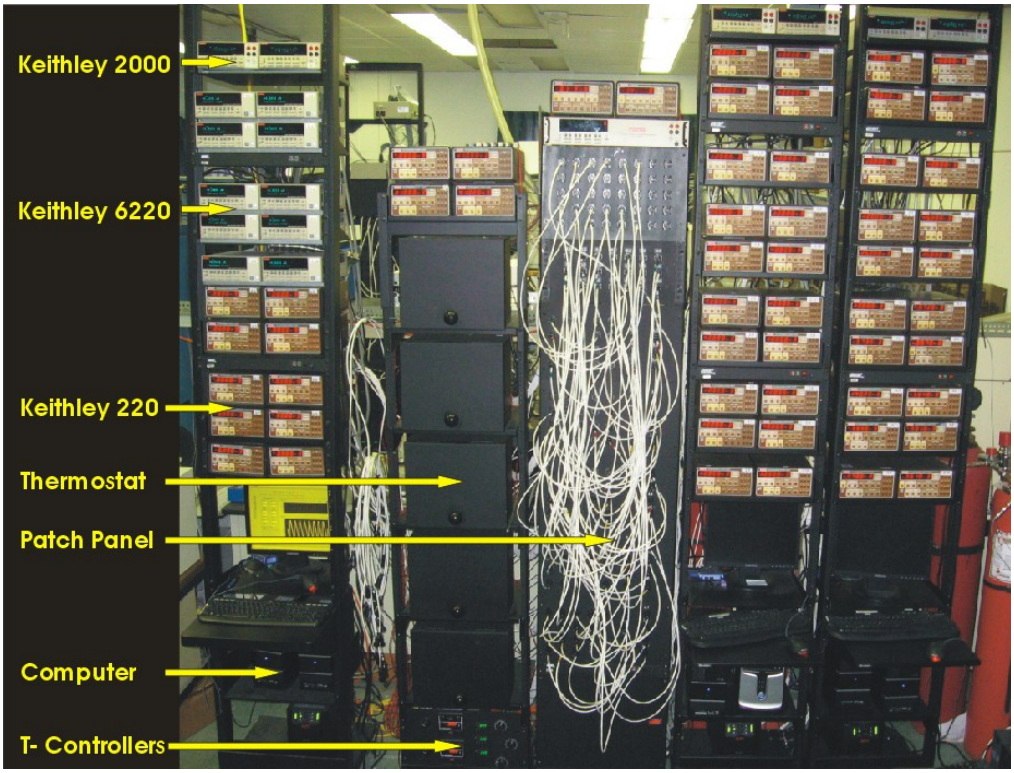

Figure 4.3 Photograph of the high precision charger at Dalhousie University. Major components are labeled.

The operating software program used to control the scanning voltmeters and the current sources was written in LabVIEW™. To achieve the highest voltage precision the Keithley 2000s needed more than 400 msec just to auto range and stabilize voltage readings. After these and other operations were completed, an average of 500 msec was spent per channel, heavily restricting the HPC sampling rate. Under these conditions each channel could only be monitored every 5 seconds. This rate was not fast enough to meet the goals set forth for Δt in Table 4.1. Therefore, post-processing software was used to linearly interpolate between the closest data points on either side of the voltage limit (two right-most points in Figure 4.1) to determine the exact time when the cell potential crossed the voltage limit. Figure 4.4 shows the CE vs cycle number for a graphite half

cell before and after the post-processing software. There is a significant reduction in the noise of the CE measurements, suggesting a noticeable improvement in Δt. We estimate the accuracy of the time determination by this method to be better than one second, sufficient for C/10 testing as shown in Table 4.1.

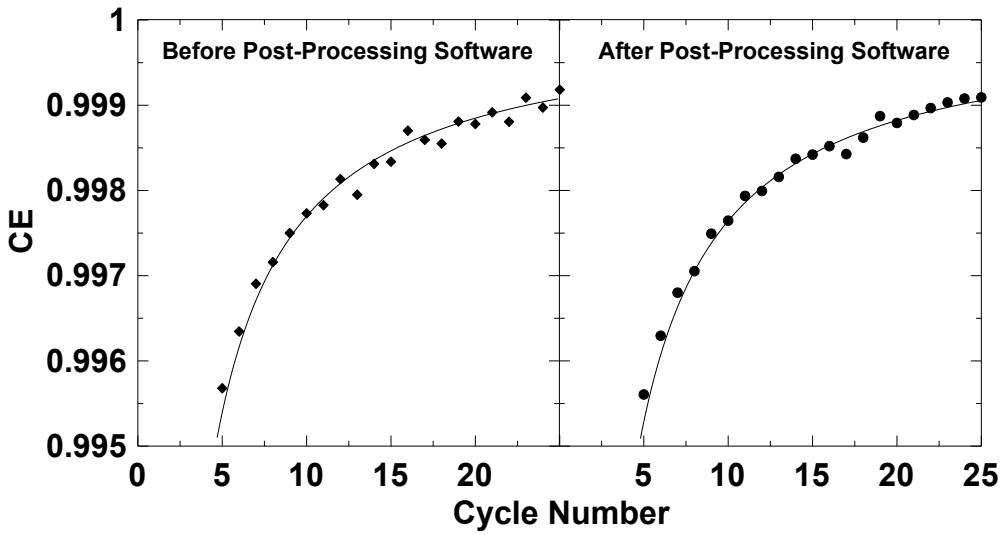

Figure 4.4 Coulombic Efficiency vs cycle data for a graphite half cell before and after the post-processing software. The graphite half cell was cycled at C/10 and at a temperature of 30^{o}C.

Figure 4.5 shows the inside of one of the thermostats in Figure 4.3. All cells tested on the HPC were placed into one of these home-built thermostats set at either 30.0, 40.0, 50.0 or 60.0^{o}C. All the cells are connected to the thermostats through the patch panel in Figure 4.3, so that any current source can be connected to any cell holder position. This allowed for full versatility in terms of operating any channel on the HPC at any temperature offered by the thermostats. All wiring to the cells was done using the "4-wire" method, with two wires carrying the current and two other wires used to monitor the voltage of the tested cell. The temperatures in the thermostats were controlled by either an Omega CNi3233 or Omega 4201A-PC2 temperature controllers.

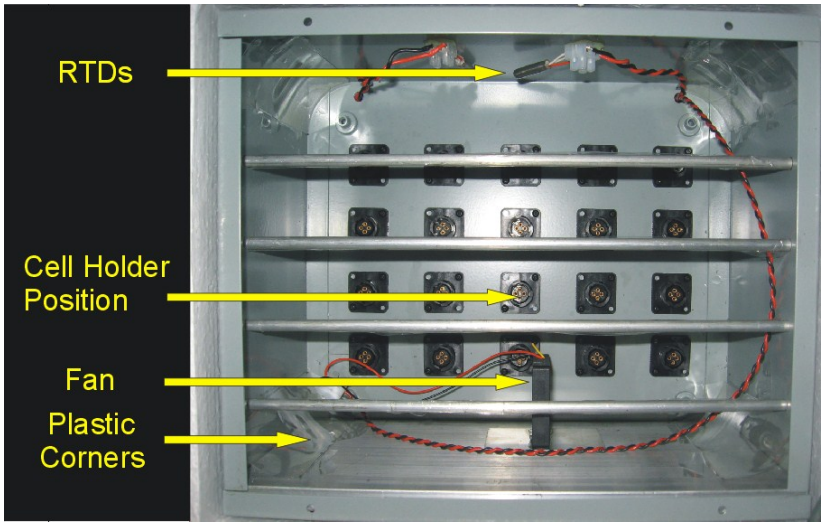

Figure 4.5 Photograph of the inside of one of the thermostats. Major components are labeled.

Each thermostat consists of a steel enclosure insulated and encased inside another steel enclosure. Inner enclosures are equipped with plugs mounted on the back for the cell holder positions, wrapped with a heating tape (~1/8" thick) and duct tape, than surrounded by ¾" of polyurethane insulation. This insulation not only serves to help maintain the temperature of thermostat, but allows the inner enclosure to fit snugly inside the outer enclosure which is 2" larger in each dimension. Lastly, an aluminum plate is placed on the bottom of the inner enclosure to act as a heat sink and a small fan is used to create convection and reduce thermal gradients inside the thermostat.

Figure 4.6 shows the temperature profile of a thermostat monitored by 9 thermocouples and heated to 60ºC. After an hour of heating, the temperature inside the thermostat stabilizes and shows a difference in temperature less then 1K between different locations inside the thermostat. This precision meets the specifications for ΔT given in Table 4.1. Although the temperature inside the thermostat does not reach

exactly 60.0ºC, the consistency in temperature between different locations is the most important detail in reducing cell to cell error caused by temperature.

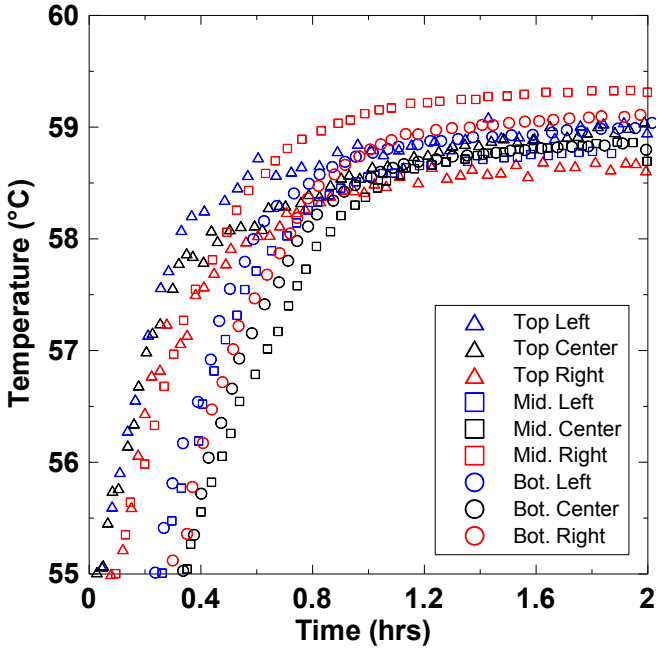

Figure 4.6 Temperature versus time of 9 different locations within the 60.0ºC thermostat as it heats. Minimal temperature variations were observed after 1 hour.

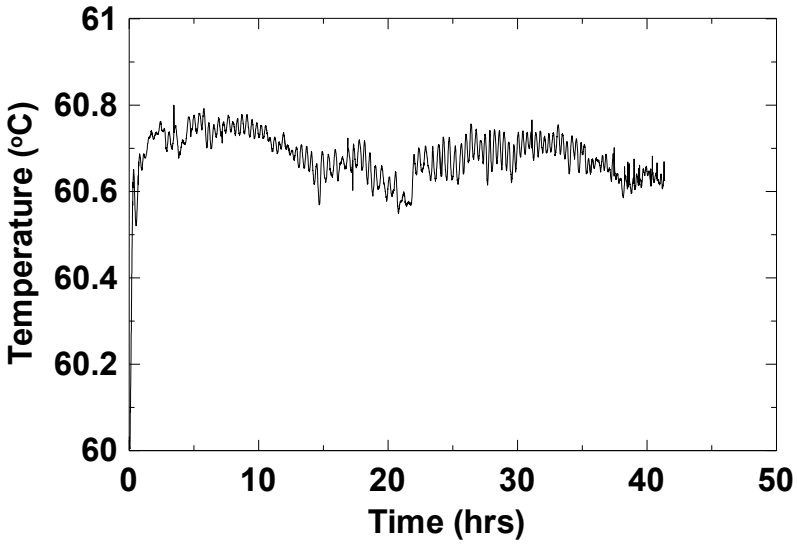

Figure 4.7 Temperature versus time of the 60.0ºC thermostat.

Figure 4.7 shows the temperature versus time of the 60.0ºC thermostat measured with a resistance temperature detector. After ~ 40 hours of testing the temperature in one location of thermostat varied by only 0.25 ºC. This is well within the < 1K specifications for ΔT outlined in Table 4.1. This long term stability in temperature is important because it helps to reduce errors caused by changes in cell temperature over time.

4.4 Reproducibility of the High Precision Charger

If all the experimental factors above are controlled to within the requirements outlined in Table 4.1, there will still be a small amount of error in the data. Figure 4.8 shows the CE versus cycle number of hypothetical Li-ion cells used to demonstrate the three different ways error can appear in high precision measurements. Figure 4.8A shows the CE versus cycle number of a single cell and a second order polynomial fit through the data set. There is scatter (or noise) in the CE measurements about the fitted trend line. The noise in the data is a result of imperfections in the HPC. In order to reduce this scatter, equipment with tighter specifications, than those listed in Table 4.1 need to be used. Figure 4.8B shows the CE versus cycle number for the hypothetical cycling of the same cell on two different channels. This "channel to channel error" results in a relative shift in the two data sets. Channel to channel error can be a result of differences between the current sources used as channels on the HPC. This error can be reduced by using careful techniques to calibrate the current sources. Figure 4.8C shows the CE versus cycle number for two supposedly identical cells cycling on the same channel. This "cell to cell error", caused by slight differences in the cells, can result in relative shifts between the two data sets. This error can be reduced by improving cell construction methods. At the

level of precision available at present discerning the difference between cell to cell and channel to channel errors can be difficult.

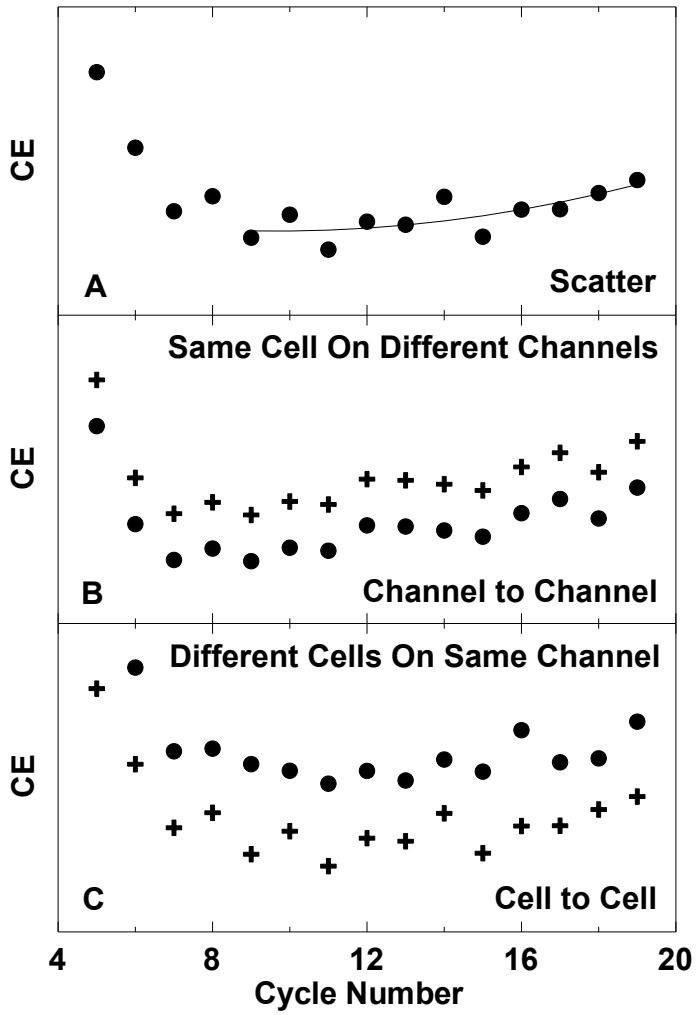

Figure 4.8 CE versus cycle number of hypothetical Li-ion cells used to demonstrate: A) scatter in CE measurements, B) channel to channel error and C) cell to cell error.

Commercially made Li-ion cells were the baseline test used to study the reproducibility of the HPC. Thirty 18650 sized $LiCoO_2$/Graphite cells (with a *capacity* of 2400 mAh) were cycled between 3.0 and 4.2 V with an applied current of 100.0 mA and at a temperature of 30.0^{o}C. The machine-assembled cells were provided by a reputable

supplier so any difference between the cells was assumed to have originated from the HPC.

Figure 4.9 shows the CE versus cycle number from the commercial Li-ion cell reproducibility test. A power failure caused by a hurricane resulted in an interruption of the second cycle of some of the cells and the data was lost. The left panel of Figure 4.9 shows the individual data points for each cell to demonstrate the small scatter of the HPC. The right panel of Figure 4.9 compares the CE of a cell tested 6 months earlier and the average CE from the 30 cells to the left. The error bars represent the standard deviation (SD) of the 30 cells about their average. The large scale of the CE axis and small scatter in the data suggests that the reproducibility of the HPC (including single channel scatter and cell to cell and channel to channel errors) is quite good and that further results can be trusted to at least ±0.0002.

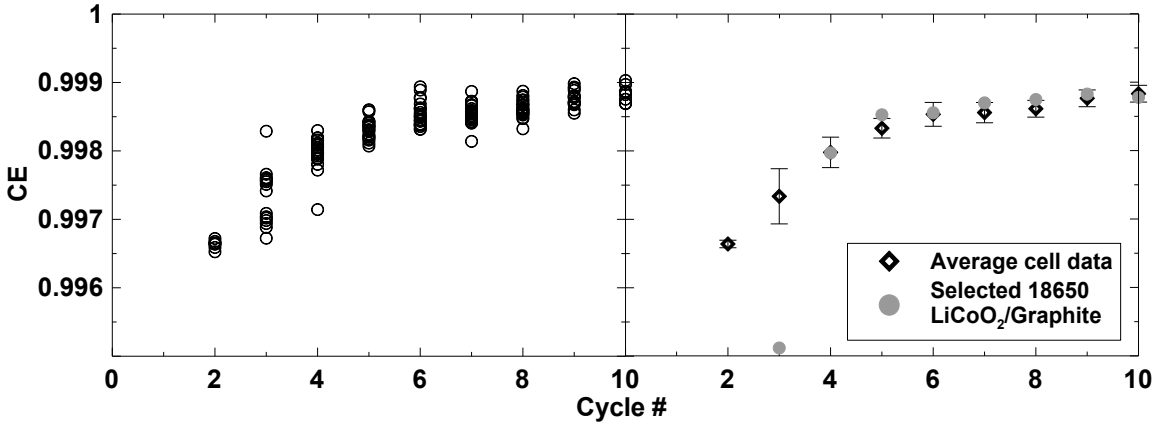

Figure 4.9 Left panel – Coulombic efficiency versus cycle number for 30 $LiCoO_2$/graphite 18650-size cells. All cells were charged and discharged at a C/24 rate at 30°C. The potential limits were 4.2 - 3.0 V for all cells. Right panel – Average coulombic efficiency of the 30 cells (error bars are standard deviation) compared to one cell selected for further charge-discharge cycling and further comparison to other cells.

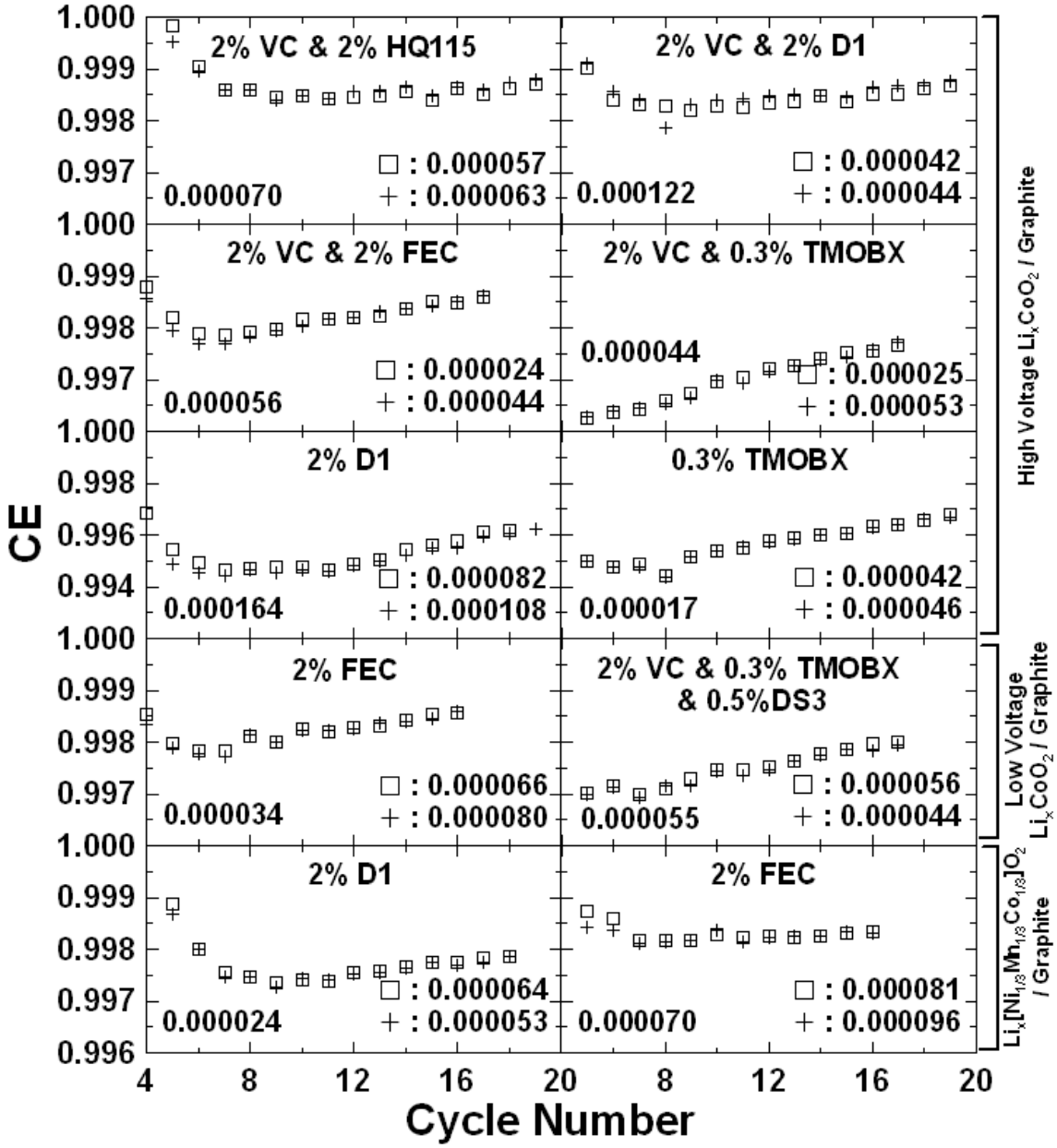

Figure 4.10 Coulombic efficiency versus cycle number of 20 prismatic Li-ion cells. Each panel shows 2 cells with identical cell chemistries. The electrodes used in each cell are shown on the far right and electrolyte additives are listed on the top of each panel. The root mean square of the scatter of the CE values for each cell is shown in the bottom right corner of appropriate panel. The combined root mean square error for cell to cell and channel to channel errors is shown in the bottom left corner of the appropriate panel.

Figure 4.10 shows the CE versus cycle number of 20 (wound) prismatic Li-ion cells cycling at a rate of C/12 and at a temperature of 40°C. The high and low voltage

$LiCoO_2$/Graphite and $Li[Ni_{1/3}Mn_{1/3}Co_{1/3}]O_2$/Graphite cells were charged and discharged between 3.400 - 4.175 V, 3.300 - 4.075 V and 3.300 - 4.225 V respectively. All of the cells were tested on different channels of the HPC. Each panel in Figure 4.10 shows 2 Li-ion cells made with the same electrode materials, electrolyte and electrolyte additives. The agreement between all 10 pairs of cells was very good. This suggests, as in Figure 4.9, that the HPC is able to measure CE very accurately. Figure 4.10 also shows that the noise in the CE measurements is very small. The scatter in the data was calculated by measuring the root mean square (RMS) between the last 10 data points for each cell and a second order polynomial fit to each data set. This allowed the noise in the CE measurements to be compared to a smooth trend line through the center of the data. The RMS scatter for each cell is shown in the bottom right corner of the appropriate panel. The average RMS scatter of all the cells was 0.000080 or 80 ppm scatter. The combined error of the cell to cell and channel to channel errors was calculated by measuring the RMS error between the polynomials used to fit nominally identical cells measured on different channels. The combined RMS error for cell to cell and channel to channel errors is shown in the bottom left corner of the appropriate panel. The average RMS error for the HPC was found to be 0.000072 or 72 ppm. Unfortunately, the cell to cell and channel to channel errors can not be separated by the measured performance.

Figure 4.11 shows the CE vs cycle number of 5 identical Li/Graphite coin cells made by the author. The agreement in the CE measurements was extremely good, and has an average SD of only ± 0.0001 (or 100 ppm – this includes cell to cell and channel to channel errors). In the author's opinion, these results are excellent and give confidence that carefully made coin cells can be used in high precision tests.

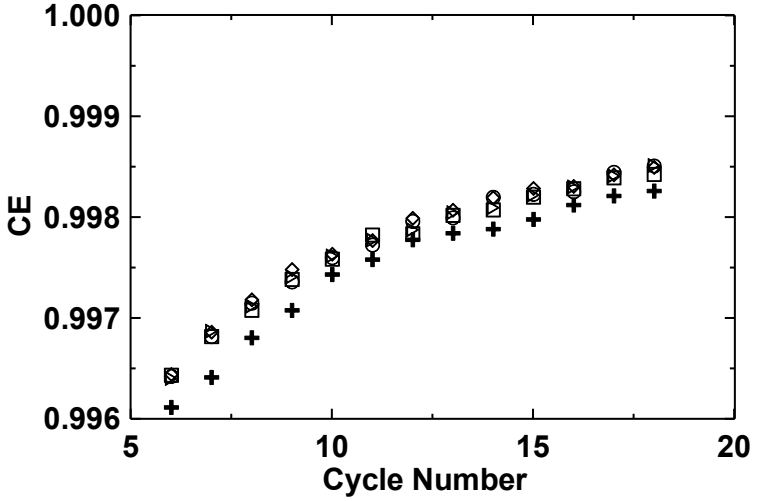

Figure 4.11 Coulombic efficiency versus cycle number of 5 Li/Graphite coin cells at a temperature of 30°C. All cells were charged-discharged between 1.2-0.005 V and at a rate of C/20.

Chapter 5 Automated Storage/Cycling System

5.1 Design of the Automated Storage/Cycling System

Capacity loss in Li-ion batteries occurs during storage and cycling. As discussed in Chapter 3 the loss of active lithium in a cell can occur through a number of different parasitic reactions. The HPC was introduced as an instrument that can carefully measure the impact these undesirable reactions have on *capacity* loss during cycling. However, such high precision equipment is not yet widely available. Here a relatively simple instrument designed to perform automated storage/cycling experiments is described.

Storage experiments are easily carried out and often lead to the same conclusions as test performed on the HPC [73]. Unfortunately, most cell storage studies are performed in a cumbersome way [60,74]. Initially, the cells are cycled a few times on a traditional battery tester to measure some initial cell characteristics like *capacity*, impedance and cycling rates. The cells are then disconnected from the battery tester and moved to another location for storage at some temperature. The open circuit voltages of the cells before and after storage are recorded by hand. After a certain amount of time the cells are returned to the battery testers for a few more cycles to evaluate the effect that the storage period had on the cells. This is done by comparing the cycling results of the same cell before and after storage. In order to improve upon these traditional storage studies it was necessary to automate this procedure. Automating this procedure also gave us the ability to monitor the open circuit voltage of the cell during storage. The precision current sources, accurate voltage measurements and thermostats described in Chapter 4

were also used. This was done so that the voltage of the cell and cell *capacity* before and after storage could be accurately measured.

Figure 5.1 shows a photograph of the 40 channel automated storage/cycling system at Dalhousie University. The Keithley 2000 scanning voltmeters were designed to sequentially scan over 20 channels, measuring the voltage of each cell every ¼ seconds while the cells are cycling and every six hours while the cells are on storage. Each Keithley 220 precision current source supplies service to 10 channels. The Keithley 705 scanner switches the current supplied by the Keithley 220s to which every cell requires cycling. When that particular cell is finished cycling the Keithley 705 switches the current to the next cell in that group of 10. An important feature of the Keithley 2000 and Keithley 705 is that they use mechanical relays which allow the cells to be under true open circuit conditions during storage. The storage/cycling system is controlled by the computer running an in-house software program written in VisualBasic.NET. This system was built and improved on by a collection of different collaborators in the Dahn lab including Chris Burns, Dillon Coyle, Jackson Dahn, Nupur Sinha, Hannah Dahn, David Stevens and the author of this thesis.

Figure 5.2 shows a schematic of a typical storage/cycling test. Before a cell is put on storage it is cycled a few times and the initial discharge *capacity* (D_0) of the cell is measured. The cell is then discharged to a predetermined voltage and the Keithley 705 scanner opens a mechanical relay leaving the cell electrically isolated for storage. During this period the cell is kept at a fixed temperature and the open circuit voltage of the cell is measured briefly (less then 1 sec) every 6 hours. After the storage period is completed the open circuit voltage is measured one last time to observe how much the voltage of the

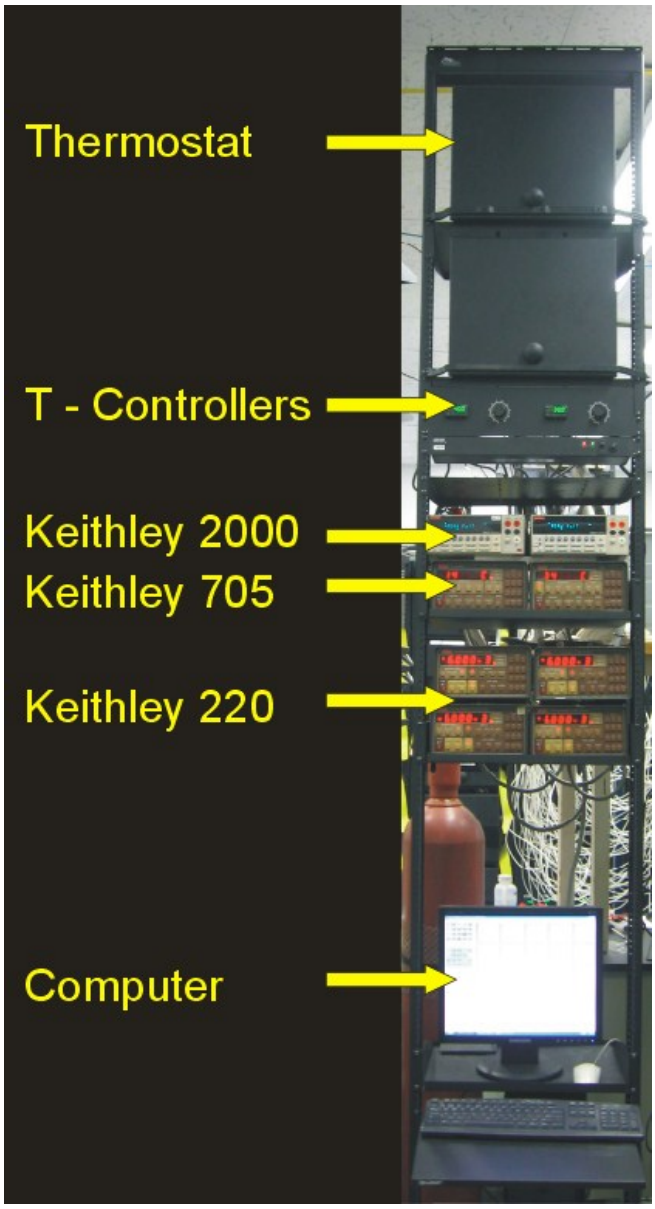

Figure 5.1 Photograph of an automated storage/cycling system at Dalhousie University. Major components are labeled.

cell has changed during storage (V_{drop}). The cell is than connected to a current source for additional cycling. The discharge *capacity* immediately after storage (D_1) and the discharge *capacity* of the fully charged cell after storage are noted (D_2). The storage/cycling test can be repeated as necessary.

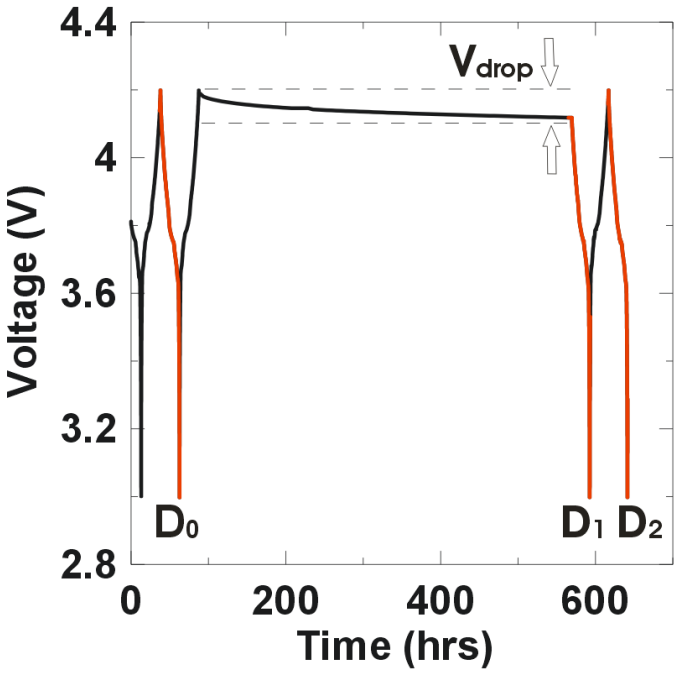

Figure 5.2 Schematic of the testing protocols used for storage/cycling tests and an illustration of D_0, D_1, D_2 and V_{drop}.

Figure 5.3 shows the potential - capacity curves of the positive and negative electrodes in a hypothetical Li_xCoO_2 / Li_xC_6 cell. As stated in Equation 1.1, the open circuit voltage of a Li-ion cell is determined by the potential difference between the positive and negative electrodes. When the cell is fully charged the potential – capacity curve of the Li_xC_6 electrode will be in a region that is fairly flat. Therefore, any process which removes active lithium from a Li_xC_6 electrode during storage will have a minimal effect on the open circuit voltage of the cell. By contrast, the potential-capacity curve of the $LiCoO_2$ electrode changes significantly in this region. Therefore, during storage changes in the potential difference between the electrodes of a fully charged cell are mostly caused by processes occurring at the positive electrode. For example, transition metal dissolution (q_{ox}^{b} – Figure 3.3) and electrolyte oxidation (q_{ox}^{a} – Figure 3.2) can cause excess lithium in the electrolyte to be added to the positive electrode and thus

reduce the open circuit voltage of the cell. Conversely, lithium lost from the Li_xC_6 due to SEI growth (q_{Li} – Figure 3.1) will not affect the open circuit voltage of the cell. Electrolyte oxidation can also affect the lithium content of the negative electrode, because as excess lithium is put into the positive electrode from the electrolyte less lithium needs to be sent from the negative electrode and is left here.

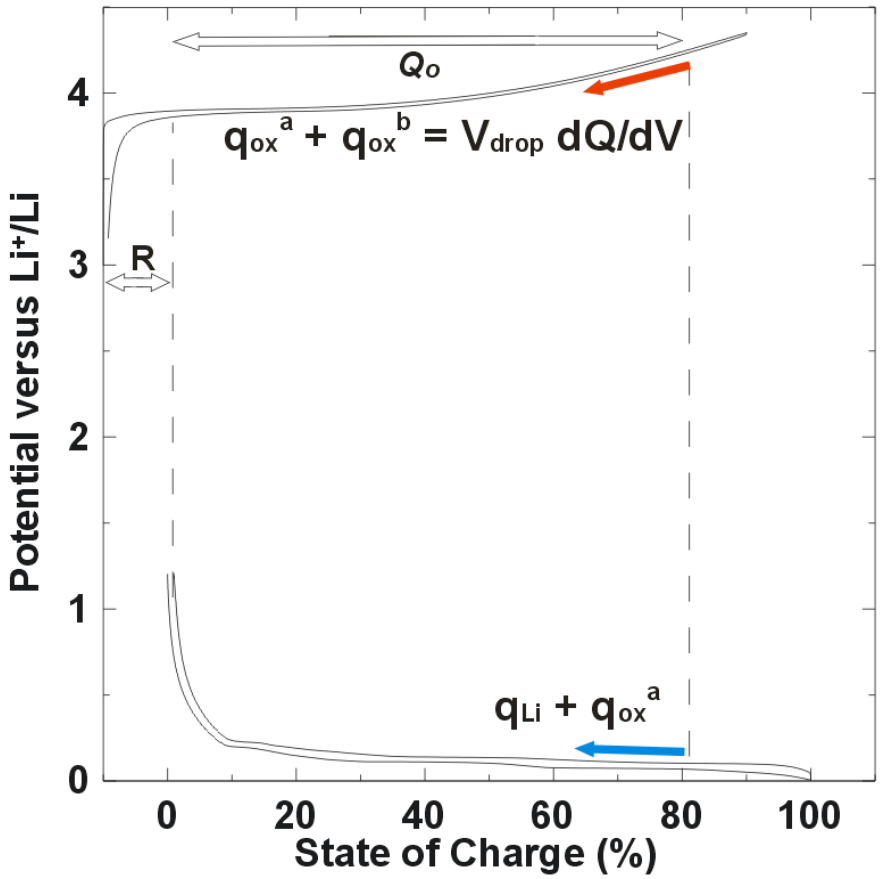

Figure 5.3 Potential versus capacity of the positive and negative electrodes in a hypothetical Li_xCoO_2 / Li_xC_6 cell. The parasitic currents which affect the Li content of the positive and negative electrode during storage are shown.

5.2 Li Accounting for Storage/Cycling Experiments

To understand how D_1, D_2 and V_{drop} depend on the parasitic reactions discussed in Chapter 3, a Li inventory model for storage/cycling experiments is introduced. As in

Tables 3.1, 3.2 and 3.3, the storage/cycling inventory model in Table 5.1 follows all the active lithium in the cell during the different periods. For the purposes of this model it is assumed that the cell has completed a single formation cycle and has finished in a fully charged state just before storage. It is also assumed, as shown in Figure 5.3, that the negative electrode is the limiting electrode at the bottom of discharge, similar to Cell B in Figure 3.6. Thus, when the cell is fully discharged, the negative electrode is completely emptied of active lithium and a *capacity*, K, is still available to receive additional lithium in the Li_xCoO_2 electrode. Before storage (the second column of Table 5.1) the number of active lithium atoms and ions in the electrodes, SEI and electrolyte are initialized to:

Active Li in the positive electrode: 0

Li^+ in the electrolyte: E

Inactive Li in the SEI: S

Active Li in the negative electrode: Q_o - K

Sum: Q_o - K+ E + S,

where E and S are the initial *capacities* of Li^+ and Li in the electrolyte and SEI respectively. The *sum* shows that the total number of Li atoms in the cell is simply equal to Q_o – K + E + S.

The cell is then put on storage (third column of Table 5.1) for a certain amount of time and various parasitic reactions take place which relocate the active lithium. After the storage period is completed, the Li is distributed as follows

Active Li in the positive electrode: $q_{ox}^{a} + q_{ox}^{b}$

Li^{+} in the electrolyte: $E - q_{ox}^{a}$

Inactive Li in the SEI: $S + q_{Li}$

Active Li in the negative electrode: $Q_o - K - q_{Li} - q_{ox}^{b}$

Sum: $Q_o - K + E + S$,

The labeled arrows in Figure 5.3 show how parasitic reactions change the content of the active Li in the electrodes during storage. After storage, the *sum* of active lithium is still equal to $Q_o - K + E + S$, showing that all of the Li atoms or ions in the cell can be accounted for.

Typically, the time taken by a cell for a single charge or discharge will be considerably shorter than the time spent on storage. Therefore, the amount of Li lost to side reactions during cycling is neglected in this analysis. Table 5.1 shows the *capacity* of Li in the electrodes, electrolyte and SEI for D_1, first charge after storage (C_1) and D_2 in the 4th, 5th and 6th columns, respectively. Table 5.1 also shows the cycle *capacity* of the cell for each period.

Table 5.1 *Capacity* inventory of a storage cell in Figure 5.3 for one storage period and 1 ½ cycles

	Initial State (D_0)	**After Storage**	**First Discharge After Storage (D_1)**	**First Charge After Storage (C1)**	**Next Discharge (D2)**
Electrolyte	E	$E - q_{ox}^{a}$	$E - q_{ox}^{a}$	$E - q_{ox}^{a}$	$E - q_{ox}^{a}$
Pos. Electrode	0	$q_{ox}^{a} + q_{ox}^{b}$	$Q_o - K - q_{Li} + q_{ox}^{a}$	0	$Q_o - K - q_{Li} + q_{ox}^{a}$
Active Li in Neg. Electrode	$Q_o - K$	$Q_o - K - q_{Li} - q_{ox}^{b}$	0	$Q_o - K - q_{Li} + q_{ox}^{a}$	0
SEI	S	$S + q_{Li}$	$S + q_{Li}$	$S + q_{Li}$	$S + q_{Li}$
SUM	$Q_o - K + E + S$	$Q_o - K + E + S$	$Q_o - K + E + S$	$Q_o - K + E + S$	$Q_o - K + E + S$
Cycle *Capacity*			$Q_o - K - q_{Li} - q_{ox}^{b}$	$Q_o - K - q_{Li} - q_{ox}^{a}$	$Q_o - K - q_{Li} + q_{ox}^{a}$

As discussed above, changes in the open circuit voltage of a cell during storage are caused by reactions which add Li into the positive electrode. As shown in Figure 5.3, if the differential capacity, dQ/dV, of the positive electrode is mostly constant for the range of potentials during V_{drop} then

$$V_{drop} \cdot dQ/dV = q_{ox}^{a} + q_{ox}^{b} \tag{5.1}$$

The difference in cell *capacity* directly before and after storage is:

$$D_0 - D_1 = q_{Li} + q_{ox}^{b} \tag{5.2}$$

$D_0 - D_1$ shows the total *capacity* lost while the cell was on storage. This is often referred to as the self discharge of a cell.

The difference in cell *capacity* before storage and after the cell has been fully charged after storage is:

$$D_0 - D_2 = q_{Li} - q_{ox}^{a} \tag{5.3}$$

$D_0 - D_2$ is known as the irreversible *capacity* loss during storage.

The difference in cell *capacity* after the cell has been charged after storage and the *capacity* of the cell directly after storage is:

$$D_2 - D_1 = q_{ox}^{a} + q_{ox}^{b} = (V_{drop} dQ/dV) \tag{5.4}$$

$D_2 - D_1$ is the reversible *capacity* loss of the cell. Equation 5.4 also suggests that $D_2 - D_1$ can be related to Equation 5.1. Therefore, the product of the differential capacity and voltage drop of the cell during storage can be related to the reversible *capacity* loss during storage.

Initially, it may appear that Equations 5.2 – 5.4 can be solved to find q_{Li}, q_{ox}^{a} and q_{ox}^{b} in terms of D_0, D_1 and D_2. Unfortunately, the three equations are not independent of each other. However, these equations can still be used to give insights into how different parasitic reactions affect the life times of Li-ion cells.

The quantities measured during storage can also be related to high precision charger measurements. Chapter 3 showed that CE, *capacity* fade and charge and discharge endpoint slippage are all affected by the same parasitic reactions which affect the storage experiments. For example, Equation 3.12 shows that the charge endpoint slippage (ΔC) is also caused by electrolyte oxidation (I_{ox}^{a}) and shuttle mechanisms (I_{ox}^{b}). Therefore, since the measurements of V_{drop} and $D_2 - D_1$ are dependent on the same variables correlations between the storage and high precision cycling measurements can be found.

Chapter 6 Differential Analysis Techniques

6.1 Differential Capacity and Voltage Analysis

A common technique for observing gradual changes in Li ion cells is differential (incremental) capacity, dQ/dV(V, n), and differential voltage, dV/dQ(Q, n), analysis, as a function of cycle number, n [34,35,75–81]. Differential measurements versus cycle number offer greater sensitivity than those based on traditional V(Q, n) measurements and can probe cell degradation over a cycle-life test. Most notably, Duberry et al., have shown that with some thoughtful considerations, many sources contributing to *capacity* fade can be identified using dQ/dV(V, n) analysis [79–81]. However, in their papers relatively large changes in dQ/dV(V, n) with cycling were observed. Had they studied a cell chemistry which was more stable, such changes would not have been so easily measured.

Figure 6.1 shows dQ/dV and dV/dQ plotted versus voltage or capacity of a commercial $LiMn_2O_4$/Graphite cell. In this thesis, for the i^{th} data point of a charge-discharge cycle dV/dQ(i) was calculated as,

$$\frac{dV}{dQ}(i) = \frac{V_{i+1} - V_{i-1}}{Q_{i+1} - Q_{i-1}} \tag{6.1}$$

and dQ/dV(i) was taken as the inverse of Equation 6.1. Thus, in spread sheets, for example, columns of i, V_i, Q_i, dV/dQ(i), and dQ/dV(i) could be created for each cycle easily. The advantage to using differential analysis is that plateaus and slopes in the voltage versus capacity curve, V(Q, n), of a Li-ion cell can appear as clearly identifiable

peaks in dQ/dV and dV/dQ, respectively. The main difference between the two is that peaks in dQ/dV represent phase transitions and peaks in dV/dQ represent single phase regions in the lithiated state of the electrode material. Differential analysis curves can also be plotted versus voltage or capacity depending on what needs to be observed. Plotting versus voltage allows differential peaks to be identified by the characteristic onset potentials and changes in the peaks from one cycle to next can help detect problems in the electrode materials and the growth of cell impedance. Differential analysis versus voltage is especially useful in half cells where the lithium reference/counter electrode maintains a constant potential of 0.00 V versus Li+/Li with cycling. Thus, changes in the location of the differential peaks originate from the working electrode. Alternatively, differential curves plotted versus capacity allow changes in the *capacity* of the positive and negative electrodes to be measured with greater sensitivity.

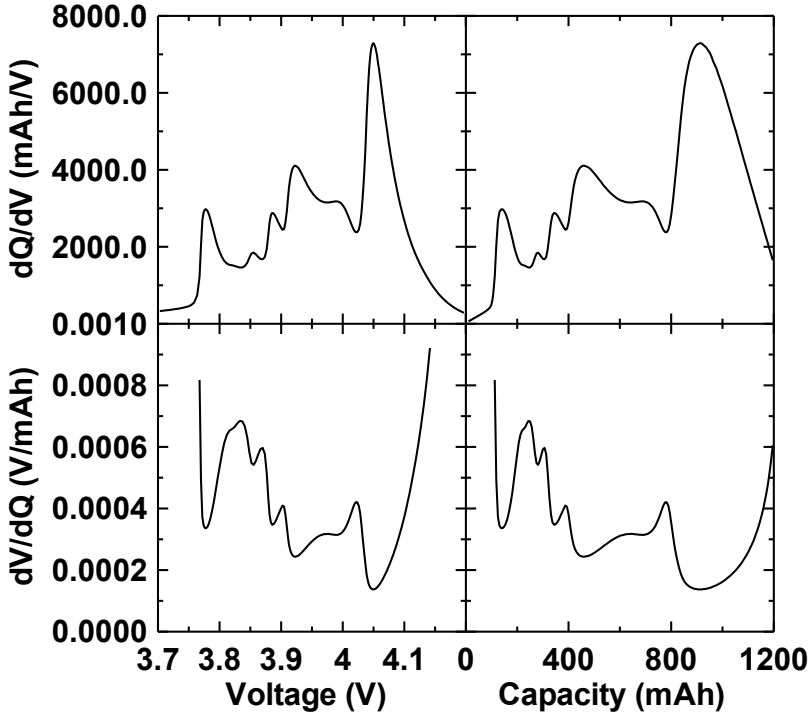

Figure 6.1 dQ/dV and dV/dQ versus voltage and capacity for a $LiMn_2O_4$/Graphite 18650 sized cell.

6.2 Delta Differential Capacity Analysis

Even the best lithium-ion cells degrade **slightly** from one charge-discharge cycle to the next and these degradations can be studied using high quality differential analysis. Unfortunately, typical battery test equipment, availably commercially, cannot make such measurements, even after many cycles. In order to increase the sensitivity to small amounts of cell degradation "delta dQ/dV analysis" is introduced here as the difference between the differential capacities of the n^{th} and m^{th} cycles, i.e. $\Delta dQ/dV(V, n, m) = dQ/dV(V, n) - dQ/dV(V, m)$. $\Delta dQ/dV(V, n, m_o)$ was calculated using a simple in-house program which measures the difference between the differential capacities of the n^{th} and m_o^{th} cycles (i.e. $dQ/dV(V, n) - dQ/dV(V, m_o)$), where m_o is the number of formation cycles. This was done by taking each data point from $dQ/dV(V, n)$ and determining, by linear interpolation, what $dQ/dV(V, m_o)$ would have been for the same V. No averaging or smoothing was used in any of the $dQ/dV(V, n)$ or $\Delta dQ/dV(V, n, m_o)$ calculations, only finite differences between data points collected 0.005 V apart. This was done so fine features were not smeared out in potential. $\Delta dV/dQ(V, n, m_o)$ could also be used in delta differential analysis, however $\Delta dV/dQ(V, n, m_o)$ would produce similar results as $\Delta dQ/dV(V, n, m_o)$. Therefore, only $\Delta dQ/dV(V, n, m_o)$ is used in this thesis for consistency.

Figure 6.2 shows $dQ/dV(V, n)$ vs. V (top row) and $\Delta dQ/dV(V, n, 2)$ vs. V (bottom row) for three commercial $LiCoO_2$/Graphite 18650 cells being cycled on 3 different battery testers at a rate of C/24 and a temperature of 30°C. The three battery testers used in this experiment were a Maccor series 4000 battery tester (right column),

an E-one Moli Energy computer-controlled battery tester (middle column) and the HPC (left column). A review of Table 4.2 shows that the HPC has the best specifications of the three battery testers described here. The small insets in Figures 6.2D and 6.2E show an expanded view of the ΔdQ/dV(V, n, 2) vs. V measurements on the HPC and Moli tester respectively. The top row of Figure 6.2 suggests that the commercial cells are very stable for the first 20 cycles since dQ/dV(V, n) are virtually indistinguishable as a function of n on the plotted graphs. Figure 6.2D shows the HPC was able to measure dQ/dV(V, n) with enough resolution so that clear noise-free changes could be observed in ΔdQ/dV(V, n, 2) for n = 5, 10, 15 and 20. The ΔdQ/dV(V, n, 2) vs. V results measured

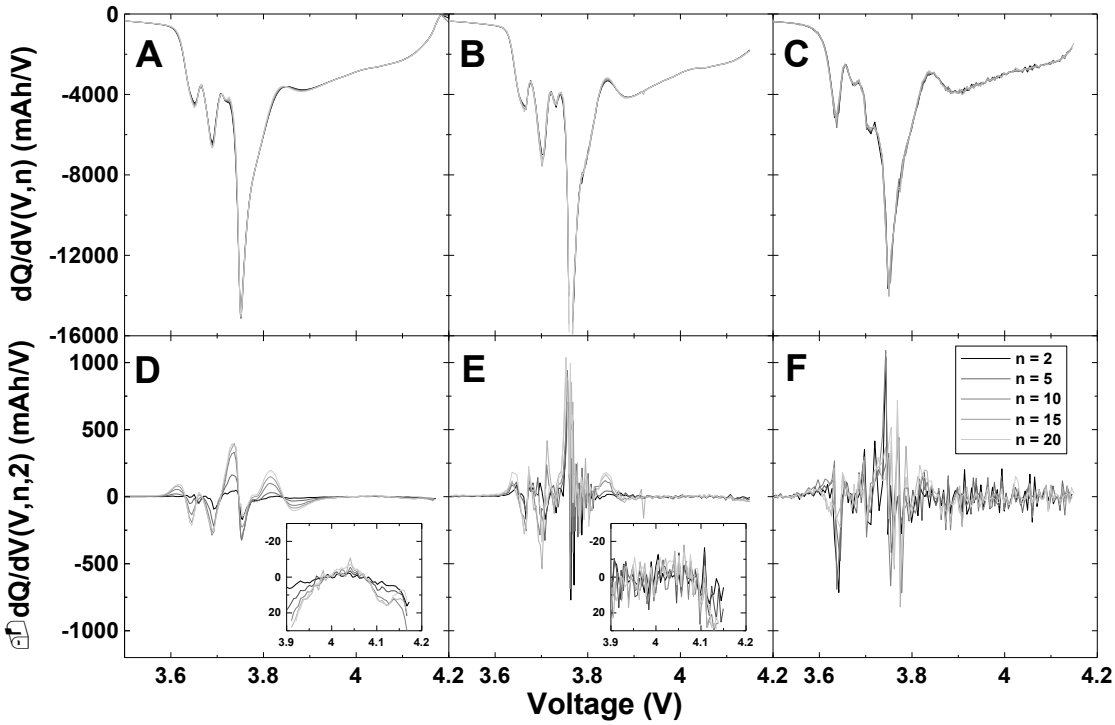

Figure 6.2 dQ/dV(V, n) versus V (Top Row) and ΔdQ/dV(V, n, 2) versus V (Bottom Row) for three $LiCoO_2$/Graphite 18650 cells being cycled on three different battery testers at a rate of C/24 and at 30°C. The three battery testers are the High Precision Charger at Dalhousie University (left column), an E-One Moli Energy computer controlled battery tester (middle column) and a Maccor series 4000 battery tester (right column). The insets show an expanded view of the ΔdQ/dV(V, n, 2) vs. V panel.

by the Moli charger and the Maccor tester, Figures 6.2E and 6.2F respectively, are so noisy as to be unusable.

Figure 6.3 shows dQ/dV(V, n) vs. V (top row) and ΔdQ/dV(V, n, 1) vs. V (bottom row) of two hypothetical cells experiencing two common changes in dQ/dV(V, n) vs. V. Figure 6.3A shows a dQ/dV peak fading with continued cycling, an event that might be associated with active material loss. Figure 6.3B shows a dQ/dV peak shifting to higher potentials with cycling possibly because of a relative slip in capacity of the two electrodes in the cell, caused by SEI growth and/or electrolyte oxidation. Figure 6.3C shows ΔdQ/dV vs. V for the cell in Figure 6.3A. As the dQ/dV peak gets smaller with cycling, the ΔdQ/dV peak grows by an equivalent amount. Figure 6.3D shows ΔdQ/dV vs. V for the cell in Figure 6.3B. As the dQ/dV peak shifts to higher potentials, peak-valley pattern emerges in the ΔdQ/dV vs. V curves centered about the average potential of the dQ/dV vs. V peak. Figure 6.2D shows the same peak-valley shape in the experimental ΔdQ/dV(V, n, 2) vs. V curves that is shown in Figure 6.3D. These peak-valley shapes are associated with the dQ/dV(3.75V, n) peak and dQ/dV(3.85V, n) dip shifting to higher potentials with cycling. This is because the negative electrode slipped to higher relative capacities than the positive electrode, causing the negative electrode features in dQ/dV(V, n) vs. V to shift to higher potentials. This slippage to higher relative capacities also caused the ΔdQ/dV vs. V features below 3.70 V. However, due to the close proximity of the dQ/dV(3.65V, n) and dQ/dV(3.69V, n) peaks, these ΔdQ/dV vs. V peaks interfered with each other and did not produce a clear peak-valley shape as cycling proceeded.

Figure 6.4 shows the voltage across a 1500 Ω resistor vs. time by applying a constant current of 0.2000 mA from each of the three battery testers. The resistor test on the HPC was the most stable and showed the least noise over time. The Moli tester had approximately the same amount of noise as the HPC, but required more time to settle to a constant value. The resistor test on the Maccor showed the most noise of the three

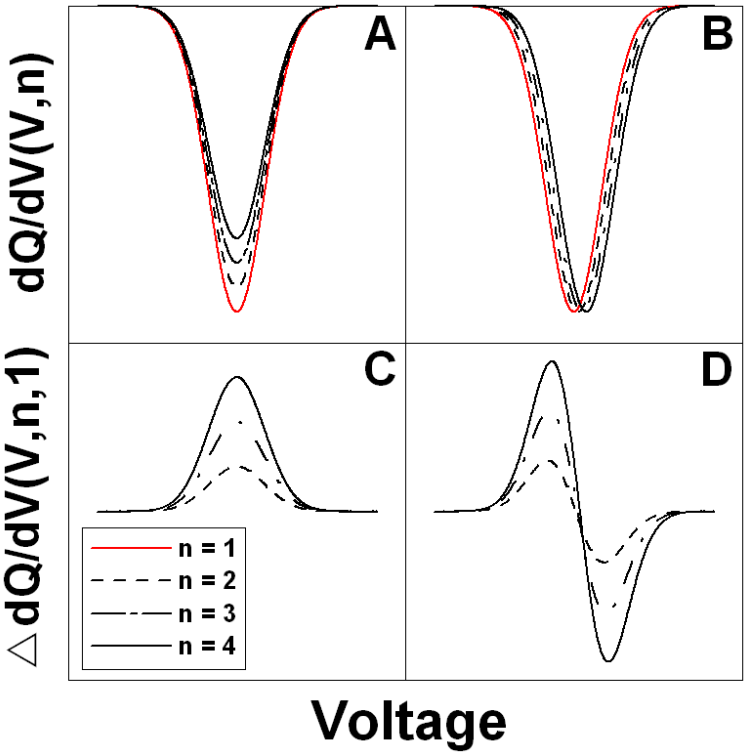

Figure 6.3 dQ/dV(V, n) versus V (top row) and ΔdQ/dV(V, n, 1) versus V (bottom row) for two hypothetical cells as described in the text.

battery testers but was still within the ±0.02% specification of the system, based on 0.02% of the full scale current of 5.00 mA. Figure 6.2 also shows less noise in ΔdQ/dV(V, n, 2) vs. V measured by the Moli tester than by the Maccor. In calculations of dQ/dV(V, n) and ΔdQ/dV(V, n, m_o), not only does the charge passed between adjacent data points need to be accurately measured, but so does the potential. The Maccor has a smallest bit resolution in voltage of 153 μV, so the error in dQ/dV will be at least 3% if

data is recorded every 5.00 mV. By contrast, the Moli tester and the HPC measure to a smallest voltage step of 10 μV. This suggests that good voltage resolution is very important in order to have high resolution dQ/dV(V, n) and ΔdQ/dV(V, n, m_o) data.

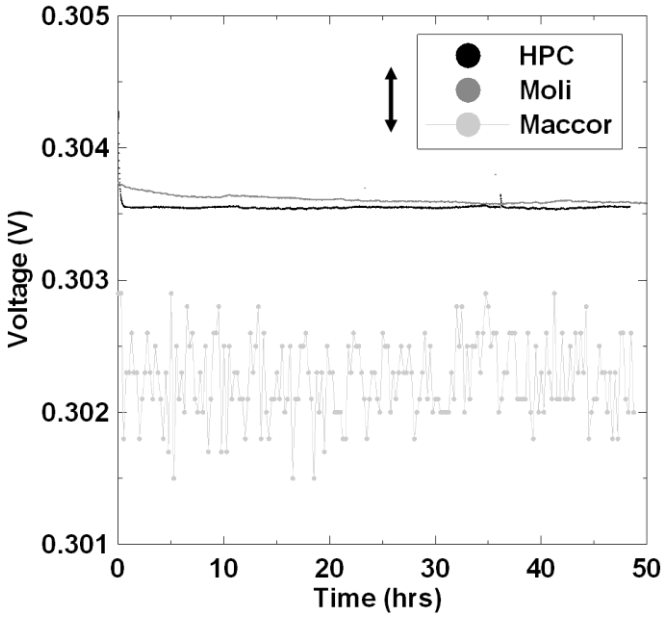

Figure 6.4 Voltage versus time across the 1500 Ω resistors with a constant current of 0.2 mA applied by the three different battery testers. The double headed arrow indicates an error of 0.1%

We suggest that delta dQ/dV analysis can serve as an excellent quality control method for Li-ion cells destined to long-lived applications. Cells exhibiting no degradation at all would have ΔdQ/dV(V, m_o+n, m_o) = 0 for all V and n. Thus, in a single cycle or in a few cycles, manufacturers and purchasers could ensure that no unexpected advanced degradation was occurring. Unlike many other analysis methods that require long term cycling in order to observe changes in a cell, high resolution ΔdQ/dV(V, n, m_o) vs. V measurements can observe even small effects in only a few cycles.

6.3 Computational Differential Voltage Analysis

Many different techniques have been developed to study how Li-ion cells age and ultimately lose *capacity*, including the incorporation of a Li reference electrode into the cell [82–89]. The insertion of a reference electrode, which allows the potential versus capacity curves for each electrode to be measured, into commercially available Li-ion cells is not a trivial task. In fact, some authors believe an inserted reference electrode interferes with cell behavior and may provide misleading information [89]. Therefore, a less intrusive approach must be taken in order to obtain reliable measurements of the potential versus capacity relations of each individual electrode versus Li, as the full Li-ion cell is charged and discharged repeatedly. Such measurements can lead to a detailed understanding of cell degradation mechanisms.

One technique proposed by Bloom et al, showed that dV/dQ(Q) analysis could be used to understand changes in Li-ion cells [90–92]. They showed that dV/dQ(Q) data from positive ($dV/dQ(Q)_p$) and negative ($dV/dQ(Q)_n$) half cells made from electrode materials used in full cells could be used to calculate the $dV/dQ(Q)_f$ for a "theoretical" Li-ion cell,

$$dV/dQ(Q)_f = dV/dQ(Q)_p - dV/dQ(Q)_n \tag{6.2}$$

Figure 6.5 shows the dV/dQ(Q) versus capacity of a real $LiMn_2O_4$/graphite full cell, a $LiMn_2O_4$/Li half cell, a graphite/Li half cell and the $dV/dQ(Q)_f$ of a theoretical $LiMn_2O_4$/graphite full cell calculated using Equation 6.2. For clarity the dV/dQ of the graphite/Li half cell has been inverted. Figure 6.5 shows that the calculated $dV/dQ(Q)_f$ curves could be matched to experimental data from a real full cell made with the same

electrode materials. The fit was made by adjusting the relative shift and *capacities* of the half cells, thus it is a reflection of the condition of the positive and negative electrodes in the real full cell.

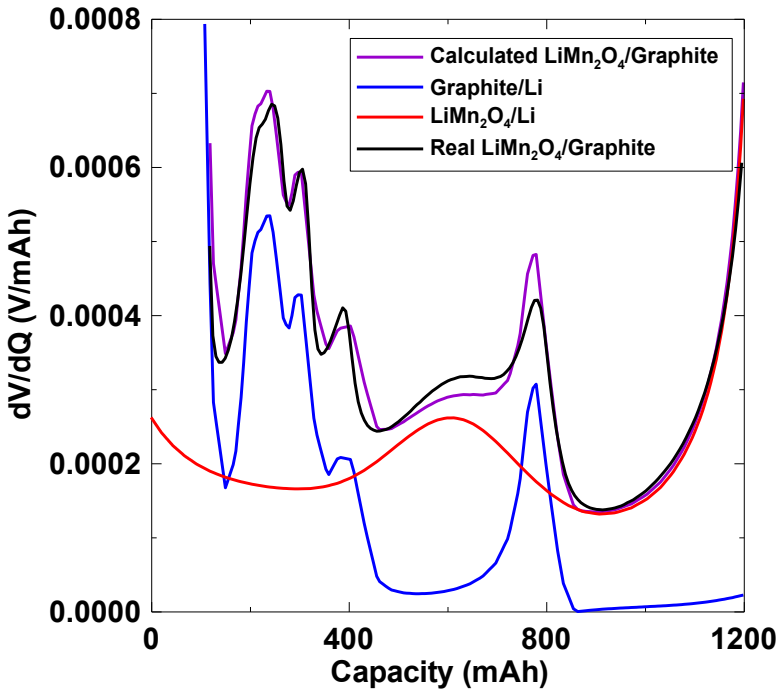

Figure 6.5 dV/dQ versus capacity of a real $LiMn_2O_4$/Graphite full cell (black), a calculated $LiMn_2O_4$/Graphite full cell (purple), a $LiMn_2O_4$/Li positive half cell (red) and a Graphite/Li negative half cell (blue).

Using differential capacity analysis a researcher could improve their understanding of the different aging and *capacity* fade mechanisms in their Li-ions cells. In the experiment performed by Bloom et al. all their calculations were done manually in Microsoft Excel and their dV/dQ(Q) data was noisy because of the poor testing equipment used. Here an automated dV/dQ analysis program written in VB.NET which uses high quality dV/dQ(Q) data from the HPC is introduced [34]. Using this program it was possible to identify different aging mechanisms in Li-ion cells much faster and with superior fits than the work preformed by Bloom et al.

Initially, half cells were made with electrodes identical to the positive and negative electrodes used in the full cells of interest. The half cells are then cycled slowly on the HPC at the same temperature as the full cell. Cycling the half cells at the same temperature as the full cell is important, because new phases and phase transitions can emerging in the active material at different temperatures which can impact the dV/dQ(Q) curve of the electrode and subsequently the Li-ion cell [93]. It is not necessary for the full cell results to be collected on the HPC, however, the more pristine the dV/dQ(Q) results are the better the fits will be.

The dV/dQ analysis program takes the measured half cell potential versus specific *capacity* (q) data cycled on the HPC and produces a "reference" dV/dQ(Q) curves for the positive and negative electrodes

$$dV/dQ(Q)_p = 1/m_p \, dV_p/dq_p \tag{6.3}$$

$$dV/dQ(Q)_n = 1/m_n \, dV_n/dq_n \tag{6.4}$$

where m_p and m_n are the active masses of the positive and negative electrodes in the Li-ion cell, respectively. The values of $dV/dQ(Q)_p$ and $dV/dQ(Q)_n$ are calculated at equally-spaced values of Q using linear interpolation. A resolution of 10,000 Q points was used for each reference curve. No data smoothing or averaging was done. A calculated full cell dV/dQ(Q) curve was calculated, using Equation 6.2, by subtracting the dV/dQ(Q) reference curve of the negative electrode from that of the positive electrode. The Qs of the positive and negative electrodes in the Li-ion cell were calculated by

$$Q = q_p m_p + \delta_p \quad (6.5)$$

$$Q = q_n m_n + \delta_n \quad (6.6)$$

where δ_p and δ_n are the positive and negative electrode slippages, respectively. The relative *capacity* of a Li-ion cell at the bottom of discharge was taken to be Q = 0 for each cycle. This can be accomplished by fixing the δ of the limiting electrode at the bottom of discharge and changing the δ of the opposing electrode to adjust the relative slippage between the electrodes. The absolute capacity of a Li-ion cell moves to higher relative capacities with each successive cycle. In this case both δ_p and δ_n must increase with cycling. The user and software package can then adjust m_p, m_n, δ_p and δ_n to give the best agreement, in a least squares sense, between the measured and calculated dV/dQ(Q) for each cycle of the cells. Confidence in the interpretation of the degradation mechanisms of cells can be achieved when a match is made between theory and experimental data, such as in Figure 6.5.

Figure 6.6 shows V(Q) versus the relative (Figure 6.6A) and absolute (Figure 6.6B) capacities of a commercial $LiMn_2O_4$/graphite Li-ion cell cycled at a rate of C/56 and at a temperature of 60.0°C. Arrows are added to indicate the general direction of the charge and discharge endpoints from one cycle to the next. The capacity axis in Figure 6.6A assumes that the capacity of the cell starts at Q = 0 at the bottom of discharge. As the relative slippage between the electrodes increases and m_p decreases, the *capacity* of the cell shrinks and the charge endpoint moves to smaller capacities. The capacity axis in Figure 6.6B tracks the accumulated capacity of the cell, assuming that the *capacity* of the cell after the first discharge was 0.00 mAh. The V(Q) curve of the cell moves to the

higher relative capacities as δ_p and δ_n increase. Figures 6.6A and 6.6B show that the *capacity* of the $LiMn_2O_4$/graphite cell drops rapidly with cycle number at 60°C.

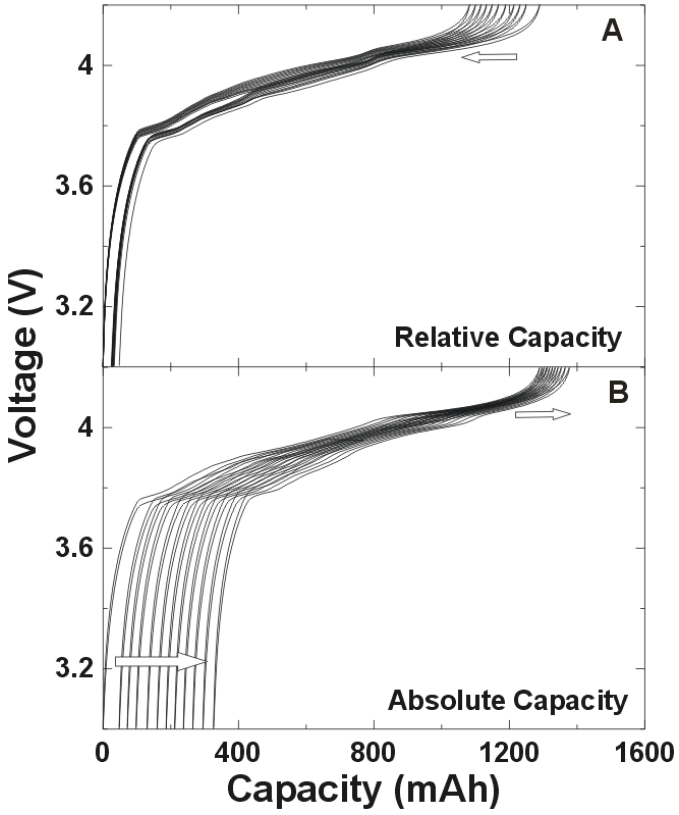

Figure 6.6 Voltage versus relative (A) and absolute (B) capacity of a $LiMn_2O_4$/graphite Li-ion cell charged and discharged at C/56 and 60°C.

Figure 6.7 shows dV/dQ(Q) versus relative capacity (top row) for the experimental data (red line) and the theoretical fit (black line) for n = 1, 3, 6 and 9 of a $LiMn_2O_4$/graphite cell. The theoretical dV/dQ(Q) curves match the experimental curves very well. This suggests that the model is good and that the electrode slippage and *capacity* reduction rates are correct. Figure 6.7 also shows the voltage vs capacity of the theoretical full cell (2nd row of panels). The reference V(Q) curves of the positive and negative electrodes versus Li are shown in the 3rd and 4th rows of panels in Figure 6.7. These curves have been positioned so that the calculated dV/dQ(Q) match the

experimental dV/dQ(Q) curves. In these calculations, the *capacity* of the graphite negative electrode has not been reduced by cycling, while the *capacity* of the positive electrode has been uniformly reduced by 0.5% per cycle (implemented by multiplying the capacity axis of the reference curve by 0.995 in each successive cycle). These calculations also showed that the relative slippage between the electrodes increased linearly by 0.99% of the initial *capacity* with each successive cycle. This can be seen in 3rd row of Figure 6.7 which shows the positive electrode reference curve slipping to lower relative capacities than the negative electrode.

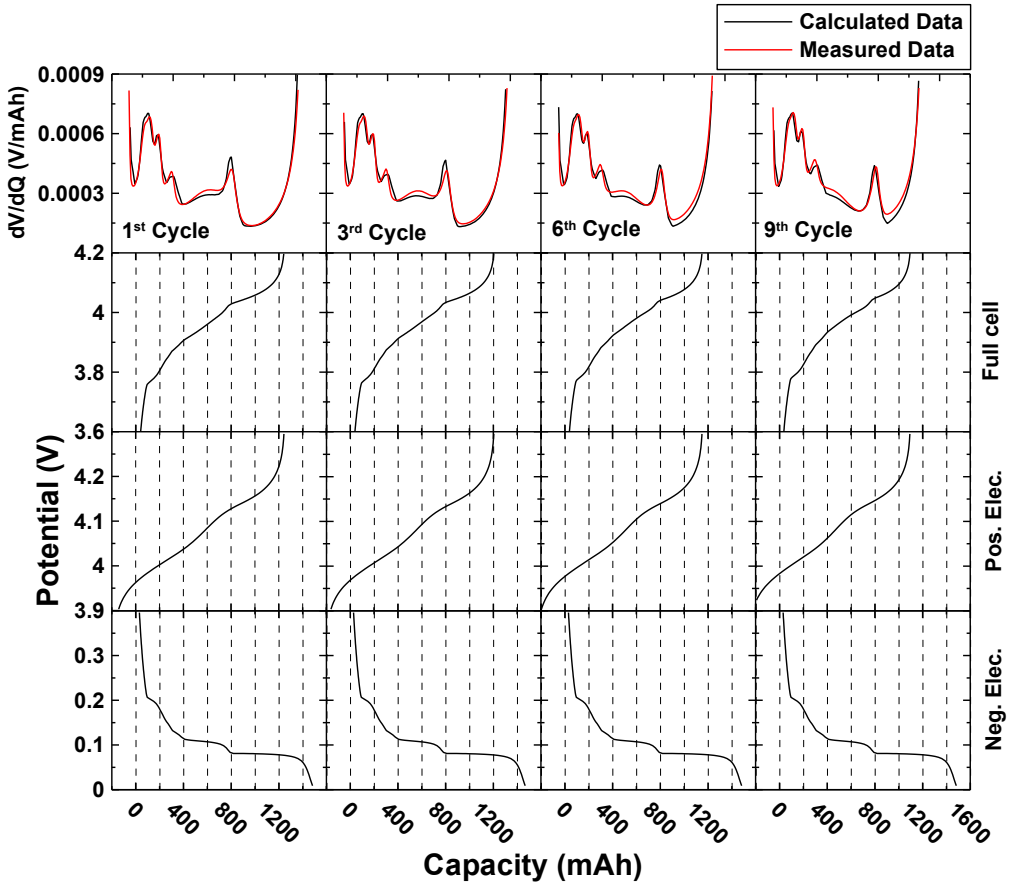

Figure 6.7 (Top Row) Experimental dV/dQ(Q) data for the $LiMn_2O_4$/graphite cell (red line) and the theoretical fit (black line) for the indicated cycles. (Bottom Three Rows) Potential difference versus capacity for the fitted theoretical full cell and the positive and negative electrodes versus Li^+/Li.

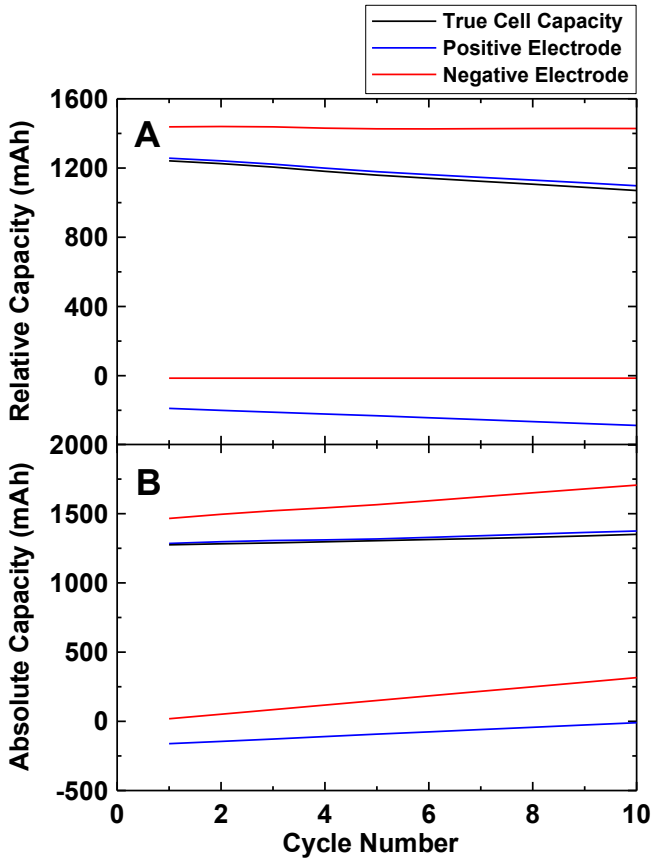

Figure 6.8 The relative (A) and absolute (B) capacities of: the reference graphite electrode when it was empty and full of lithium (red curves); the reference $Li_xMn_2O_4$ electrode when it reached 4.3 V and when it was full of lithium (blue curves); and the *capacity* of the experimental cell in the charged state (black curve).

Figure 6.8 shows the relative (Figure 6.8A) and absolute (Figure 6.8B) capacities of: the reference graphite electrode when it was empty and full of lithium (red curves); the reference $Li_xMn_2O_4$ electrode when it reached 4.3 V and when it was full of lithium (blue curves); and the *capacity* of the experimental cell in the charged state (black curve), all plotted versus cycle number for the same reference electrodes and cell data in Figure 6.7. In Figure 6.8A, Q = 0 represents the capacity of the experimental cell in a fully discharged state at 3.0V. Figure 6.8 shows that the Li-ion cell becomes fully charged (reaches the upper voltage limit of 4.2 V) before the positive electrode reaches 4.3 V vs.

Li (upper blue curve in all panels) and before the negative electrode is completely filled (upper red curves in all panels). This is by design to ensure that lithium does not plate on the negative electrode and that the positive electrode is not charged to excessively high potentials. Figure 6.8 shows, as in Figure 6.7, that the *capacity* of the positive electrode decreases slowly with cycling (capacity difference between the two red curves) and that the *capacity* of the negative electrode remains constant for the first ten cycles.

A $LiMn_2O_4$/graphite cell at 60°C was deliberately picked to illustrate this dV/dQ analysis, because the electrode slippage and *capacity* loss in the cell is dramatic over a few charge-discharge cycles. This method can also be applied with success to more stable cell chemistries like $LiCoO_2$/graphite cells using the principles of delta dQ/dV analysis described above. However, in the case of $\Delta dQ/dV(V, n, m_o)$ analysis full cell data would also have to be measured with an HPC.

High precision constant current chronopotentiometry and coulometry coupled with a dV/dQ analysis program can be used to eliminate or reduce the need for reference electrodes in full Li-ion cells. With this method, various battery aging mechanisms such as SEI growth, electrolyte oxidation and positive electrode *capacity* loss can be differentiated and measured. Such a straightforward and non-intrusive method offers an exceptional way to observe the natural behaviors and aging of many battery chemistries. There may be no better way to determine cell health in commercial cells.

Chapter 7 Material Analysis

7.1 X-ray Diffraction

Powder X-ray diffraction (XRD) is a non-destructive technique used to study the solid state structure of a sample. The application is particularly sensitive to small changes in the crystal structure of a series of samples. For more information about powder X-ray diffraction please refer to Cullity [94] and Warren [95].

All XRD patterns were collected with a Siemens D5000 powder diffractometer equipped with a Cu target X-ray tube and a diffracted beam monochromator. The D5000 is designed such that the powder samples are positioned on a fixed plate and the tube and detector arms are set at an angle θ with respect to the sample and an angle 2θ from each other. The slit widths used on the diffractometer were 0.5° divergence, 0.5° anti-scatter and 0.6 mm receiving, which provided XRD patterns with a resolution of about 0.12° full width half maximum at $2\theta > 50°$.

In this study, all of the XRD samples were air sensitive electrode materials recovered from cells that had cycled many times. In order to prevent the samples from air exposure they were carefully prepared in a He-filled glove box. To protect the samples outside the glove box, a special air-tight container was used, equipped with a zero background holder (ZBH) [96]. The ZBH was made from a single crystal of silicon cut along the 510 plane, which produces no coherent scattering during XRD. The 510 plane of silicon produces of no coherent scattering because it has a structure factor of zero.

7.2 Surface Area Measurements

The basic principle of a single-point Brunauer–Emmett–Teller (BET) surface area measurement is that gas, at a certain partial pressure and temperature, will form a monolayer on the surface of a solid. The surface area of the solid can then be measured by counting the number of adsorbed molecules. The BET surface area analyzer used in this experiment was a Micromeritics Flowsorb II 2300. Please refer to the classic paper by Brunauer, Emmett and Teller for more information about BET [97].

Figure 7.1 shows a schematic diagram of the Micromeritics Flowsorb II 2300 surface area analyzer. In this study the surface area of mesocarbon microbeads (MCMB), carbon black and three graphite electrodes (with different weight to weight ratios of the active material, carbon black and binder) were determined with BET surface area measurements. Before each measurement the test samples were carefully weighed (~500 mg) and then placed in an air tight glass container connected to the BET. The samples were then degassed by heating to 160°C for at least 1 h. After degassing, a constant flow of the mixed gas was passed over the test samples and the glass container holding the sample was submerged in a bath of liquid nitrogen. The matched thermal conductivity cells on the Flowsorb were then used to measure the difference in concentration of N_2 before and after the gas was passed over the test sample. Assuming a constant flow of gas, the volume of N_2 being absorbed by the sample can be integrated from the difference measured by the conductivity cells. The volume of N_2 being desorbed from the sample can also be measured by heating the test sample to room temperature in a bath of lukewarm water. For calibration purposes, a syringe can be used to introduce a known quantity of N_2 gas through the septum on the analyzer and into the inline gas flow. The

Flowsorb uses a gas mixture of N_2:He (30:70 mol%) which is cooled in the in-line cold trap which helps to reduce impurities in the initial gas mixture. The filter is used to prevent the sample from contaminating the rest of the apparatus. The flow meter is used to ensure the desired flow rate and the back diffusion restrictor acts to reduce changes in the flow rate due to changes in the back pressure.

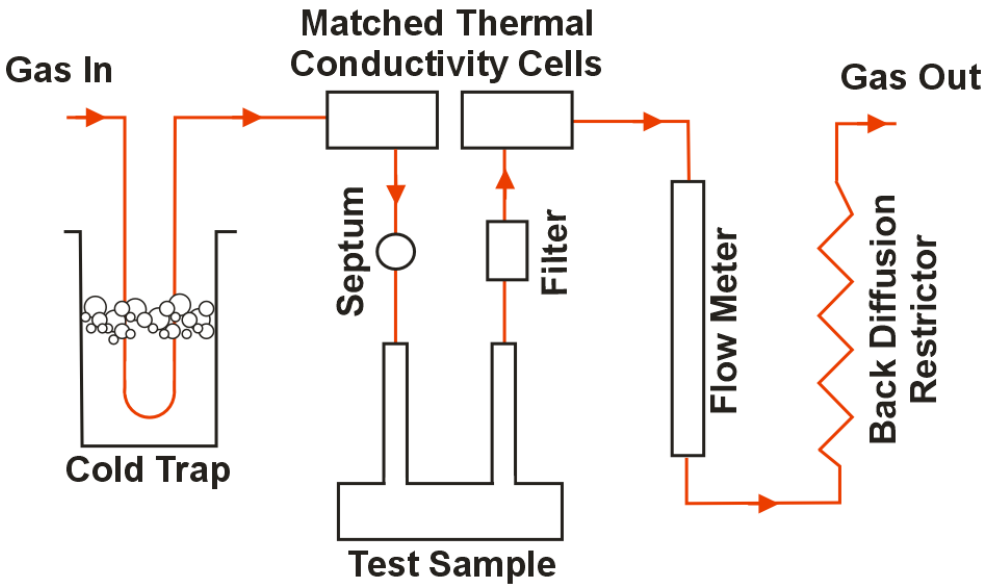

Figure 7.1 Schematic diagram of the Micromeritics Flowsorb II 2300 surface area analyzer

7.3 Atomic Absorption Spectroscopy

Atomic Absorption (AA) spectroscopy is an analytical technique which uses the absorption of light by free atoms in a gas to determine the variety and quantity of the absorbing elements. For a more detailed explanation of AA spectroscopy please refer to Salvin [98].

In this work, metal ion dissolution from the working electrode of half cells was measured with AA spectroscopy. After cells had been cycled many times they were carefully dissembled to recover the spacer (which contacts the Li foil), Li electrode and the separator closest to the Li electrode. These were then put into a Nalgene bottle containing 10 ml of 0.1 M HCl in distilled water. After the Li electrode finished reacting with the water, the separator and spacer were removed and the solution was sent away for AA analysis. AA analysis was performed at the Mineral Engineering Centre of Dalhousie University.

Chapter 8 SEI Growth in Li/Graphite Cells

One of the greatest challenges in improving the calendar and cycle life of Li-ion batteries at elevated temperatures is to improve the stability of the SEI on the negative electrode. Over the past three decades the formation of this film has been extensively studied by many researchers [9,52,57,99–105]. Most notably Aurbach et al. have studied the effect of different additives and electrolytes on SEI composition [9,52,57,105]. Despite these advancements, fully stable SEI layers on the negative electrode have not yet been created and thus the lifetime of Li-ion batteries is not infinite.

Here, the HPC was used to study the CE and charge and discharge endpoint *capacities* of Li/graphite coin cells cycled at various rates and temperatures. CE is a sensitive measure of the amount of Li consumed by the growth of the SEI each cycle. The charge and discharge end point *capacities* directly track the total irreversible *capacity* and the total *capacity* transferred to the graphite electrode, respectively, with cycling. A high precision charger is required to perform these types of measurements – small errors in currents lead to large cumulative errors after many cycles.

8.1 Experiment

All Li/graphite cells used in this experiment were made with MCMB (Osaka Gas, heated to ~2650°C), Super-S carbon black (MMM Carbon, Belgium) and a PVDF (Kynar 301F Elf-Atochem) binder. The weight to weight ratios of the active material, carbon black and binder used in the graphite electrodes were 86:7:7, 90:5:5 or 95:3:2, and are referred to as such here. All of the electrodes were dried under vacuum at 90°C overnight. The

electrolyte used in all of the cells was 1 M $LiPF_6$ in an ethylene carbonate/diethylcarbonate [1:2 v/v, Novolyte Technologies] solution. Coin-type cells, as shown in Figure 2.4, were made with two Celgard 2300 separators, a lithium foil common counter and reference electrode and the graphite electrodes described before. All cells were charged and discharged with a constant current between 1.2 and 0.005 V.

In order to observe the behaviour of Li/graphite cells cycled at different temperatures and rates, six cells were made with 86:7:7 electrodes. These cells were then cycled at either C/10 or C/24 and at temperatures of 30.0, 40.0 and 50.0^{o}C. To observe if these trends held over long times, one 95:3:2 electrode was also cycled at a rate of C/20 and a temperature of 40.0°C for ~1100 hrs.

Lastly three cells made with either 86:7:7. 90:5:5 or 95:3:2 electrodes were cycled at C/26 and at a temperature of 30.0^{o}C. Carbon black has a much larger surface area than graphite so comparing the three electrodes allowed for the impact of total surface area to be studied. BET surface area measurements for MCMB, carbon black and the three electrodes materials were made using the Micromeritics Flowsorb surface area analyzer described in Chapter 7.2.

All Li/graphite cells were tested on the HPC.

8.2 Results

A simple model for SEI growth can be formulated similarly to the growth of oxides on metals. A metal exposed to air reacts to form an oxide which helps passivate the surface and slows further reaction. Similarly, lithiated graphite exposed to electrolyte reacts to form an SEI which helps passivate the surface and slows further reactions. Lawless

reviewed numerous models of oxide growth on metals which he showed followed a huge variety of rate laws [106]. The simplest of these is the "parabolic growth law" which assumes that the rate of increase in the thickness of the passivating layer, x, is inversely proportional to the thickness of the layer:

$$dx/dt = k/x \tag{8.1}$$

where k is a proportionally constant. Equation 8.1 is similar to the findings of Phoehn et al. [59] who showed that k is proportional to the product of the specific conductivity of the SEI and the surface area of the negative electrode. Thus, Equation 8.1 postulates that the growth rate of the SEI (or how much Li is consumed by the growth of the SEI) is proportional to the conductance of the SEI, which decreases as the SEI thickens. Equation 8.1 can be rewritten as:

$$x\,dx = k\,dt$$

and integrated to give:

$$½x^2 = k\,t + C.$$

If the thickness is taken to be x = 0 at t = 0, then the constant, C is zero and one can write:

$$x = (2k\,t)^{1/2}. \tag{8.2}$$

The rate of change of the thickness of the passivating layer is given by combining equations 8.1 and 8.2, to give:

$$dx/dt = (½k)^{1/2}\, t^{-1/2} \tag{8.3}$$

In a Li/graphite cell, it is believed that the SEI begins to form as lithium is transferred electrochemically to the graphite electrode. With continued cycling more and more Li is irreversibly consumed as the SEI thickens. The total amount of Li consumed is directly proportional to the SEI thickness (which might be described by Equation 8.2) and the amount of lithium consumed by SEI growth is directly proportional to the irreversible *capacity* each cycle (which might be described by Equation 8.3). Therefore, it is important to carefully measure the total accumulated irreversible *capacity* and the irreversible *capacity* per cycle and compare them to the predictions of Equations 8.2 and 8.3. Many researchers studying the failure of Li-ion batteries have identified this *capacity* loss versus $t^{1/2}$ (or equivalent) relationship and have demonstrated that their models fit experimental data very well [54,107–109].

The HPC can accurately monitor the growth in the irreversible *capacity* of the cell over many cycles. After 10 C/10 cycles, the total error in accumulated irreversible *capacity* is only 0.2 %. After 100 C/10 cycles it is only 2 %. In the case of negative electrode half cells the CE can be related to the irreversible *capacity* per cycle ,or charge endpoint slippage (Δ_C), by:

$$\Delta_C = (1 - CE)\, Q_o, \tag{8.4}$$

Equation 3.10 showed that the CE of a full cell is related to the irreversible *capacity* (discharge endpoint slippage, Δ_D) of the cell at the bottom of discharge, or when the negative electrode is completely empty. Equation 8.4 measures the irreversible *capacity* at the top of charge which in the case of negative half-cells is also when the negative electrode is completely empty. Therefore, the two equations are similar because they both measure the *capacity* lost during one cycle of a cell in terms of the limiting electrode.

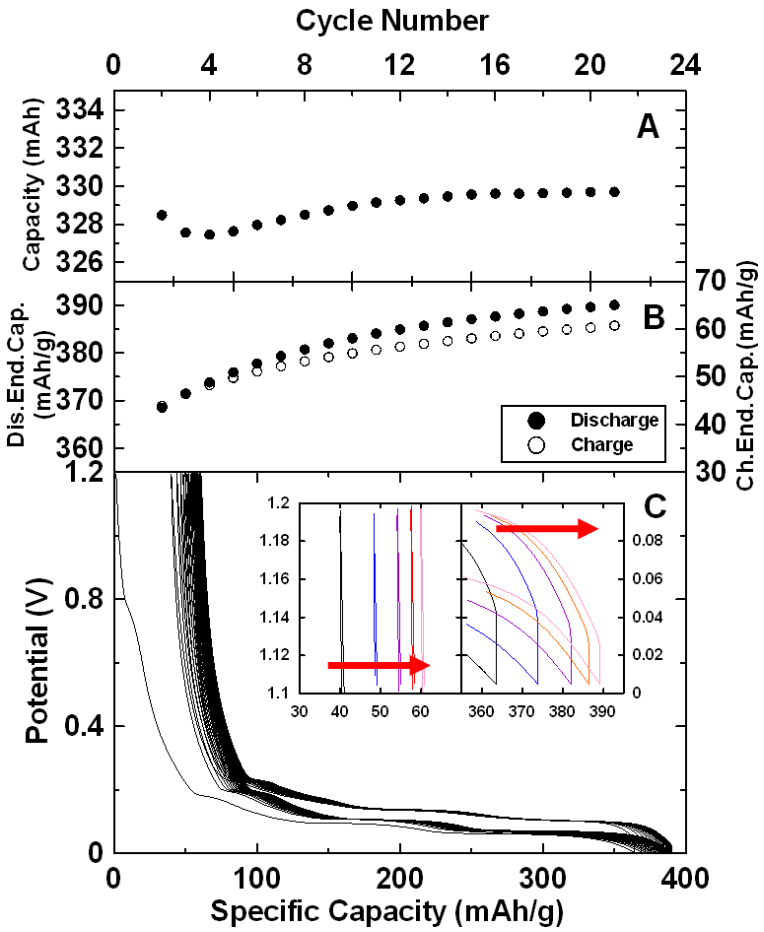

Figure 8.1 A) *Capacity* versus cycle number of a Li/graphite coin cell charged and discharged at C/24 and at a temperature of 40°C. B) Charge and discharge *capacity* endpoints versus cycle number. C) Potential versus specific *capacity*. The inset shows an expanded view of the charge and discharge endpoints, left and right panels respectively, for the 2nd, 4th, 6th, 8th and 10th cycles.

Figure 8.1A shows the *capacity* versus cycle number for a 86:7:7 cell cycling at C/24 and at a temperature of 40°C. The *capacity* of the cell changes by <1% after 20 cycles. Figures 8.1B and 8.1C show the charge and discharge endpoint *capacities* versus cycle number and the cell potential versus specific capacity, respectively, for the same cell. The smaller insets in Figure 8.1C show an expanded view of the bottom of discharge (left side) and top of charge (right side) for the 2^{nd}, 4^{th}, 6^{th}, 8^{th} and 10^{th} cycles (arrows expressing the direction of motion). All endpoints move to the right with cycling. The total accumulated irreversible *capacity* versus cycle number is given by the charge and discharge endpoint *capacities* plotted in the top panel of Figure 8.1B.

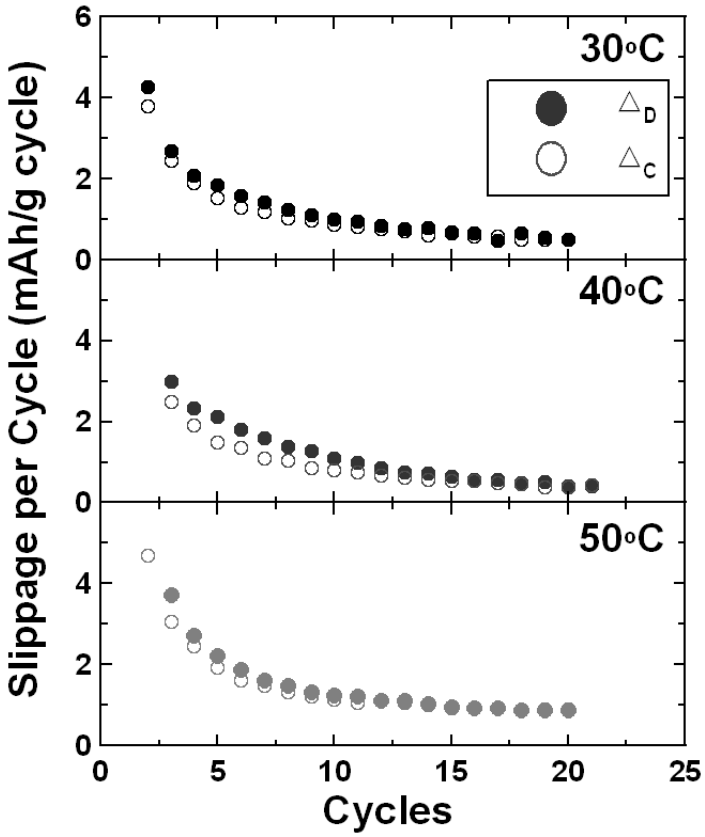

Figure 8.2 Slippage per cycle versus cycle number for the charge and discharge endpoints of Li/graphite coin cells charged and discharged at C/10 and at temperatures indicated.

Figure 8.2 shows Δ_D and Δ_C versus cycle number for the Li/graphite 86:7:7 cells cycling at C/10. The slippage per cycle of all of the cells decreased with increased cycling number, but never reached 0.00. This is because the SEI growth rate slows with time but never becomes zero, as predicted by Equation 8.3. Figure 8.2 also shows that Δ_D and Δ_C match closely. This is because the reversible cell *capacity*, as in Figure 8.1A, is fairly constant for these cells. Δ_C is equal to the growth in irreversible *capacity* per cycle and is proportional to the amount of lithium consumed by the SEI in each cycle. In a case where an excess of Li is not available, such as in a full cell, this effect would produce a loss in *capacity* each cycle.

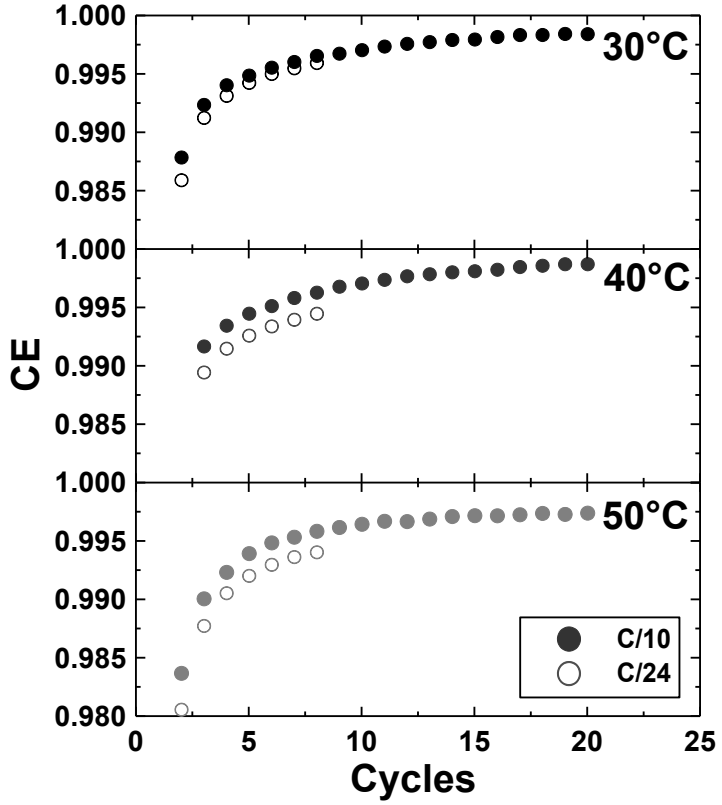

Figure 8.3 Coulombic efficiency versus cycle number for Li/graphite coin cells charged and discharged at the C-rates and temperatures indicated.

Figure 8.3 shows the CE vs cycle number for the Li/graphite 86:7:7 cells cycling at C/10 and C/24 and at temperatures of 30.0, 40.0 and 50.0°C. The CE of the cells cycling at faster rates was closer to unity than the CE of cells cycling at slower rates. This is because when cells cycle at slower rates, there is more time during each cycle for the SEI to grow and consume charge. Figure 8.3 also shows that the CE of the cells gets closer to unity with cycling. This is due to the same effect observed in Figure 8.2; the SEI thickens and slows the rate of reaction between intercalated lithium and the electrolyte. Thus, as less Li was lost to the SEI each cycle, the cycling efficiency of the cells was improved. Figure 8.3 also shows that the CE of the cells was affected by temperature. As the temperature was increased, the CE of the cells decreased. This is because parasitic reactions, like SEI growth, are amplified with increased temperatures.

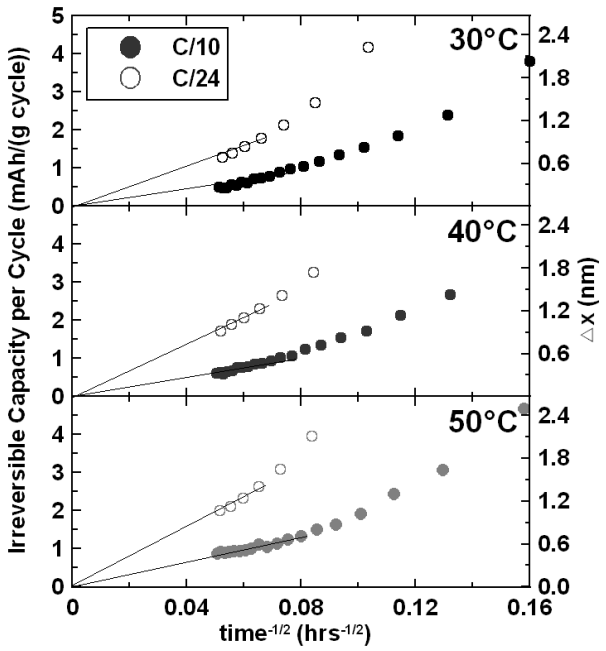

Figure 8.4 Irreversible *capacity* per cycle (left hand y-axis) and the increase in the SEI thickness for N^{th} cycle (right hand y-axis) plotted versus $t^{-1/2}$ for Li/graphite coin cells cycled at C/10 and C/24 rates at the indicated temperatures. The solid lines are extrapolations to the origin for the reader's convenience.

Figure 8.4 shows the irreversible *capacity* per cycle plotted versus $t^{-1/2}$ for the same cells in Figure 8.3. The results for all cells become quite linear at large times and appear to extrapolate to the origin at infinite time, as predicted by Equation 8.3. At small times, the data appears to deviate somewhat from the linear trend. This is a result of the growth rate of the SEI changing significantly during a single charge-discharge cycle, but the experimenter only recording the data at the end of the cycle. This causes the average irreversible *capacity* to appear larger than it should be during the early cycles. The cells which cycle at C/24 have larger irreversible *capacities* per cycle by about 2.4 times than the cells which cycle at C/10, due to the additional time that SEI thickening reactions can occur in the slowly cycling cells.

Figure 8.5 shows the irreversible *capacity* per hour, derived from the data in Figure 8.4 by dividing by the time of one cycle, plotted versus $t^{-1/2}$. Figure 8.5 illustrates that the loss of lithium per unit time in cells cycled at the same temperature is independent of the cycling rate. This suggests that the SEI formation reactions occur at the same rate independent of whether the cells are cycled or not. This $t^{1/2}$ dependence on the growth of the SEI has also been observed by other researchers [7,54–56,107,108,110,111], most notably Colclasure et al. [112]. In a theoretical study they showed that this time dependence was a result of the electron diffusion in the SEI layer being the rate determining reaction [59,99,113].

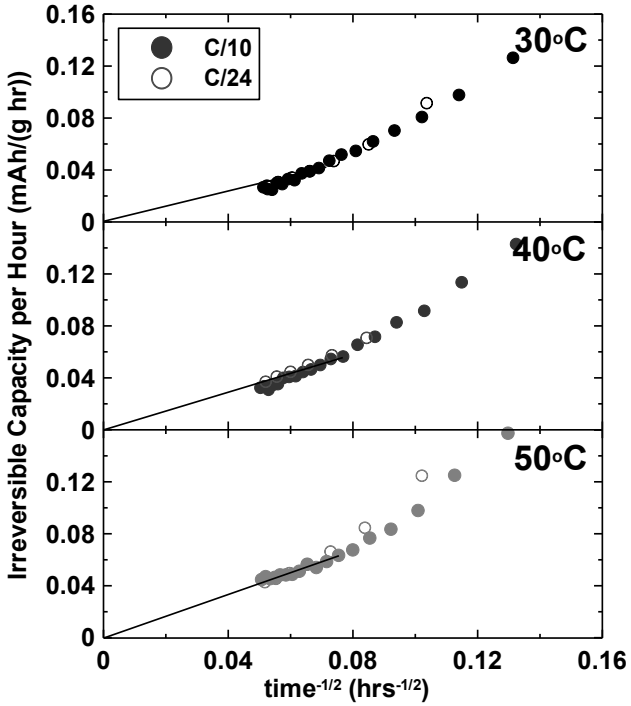

Figure 8.5 Irreversible specific *capacity* per hour plotted versus $t^{-1/2}$ for Li/graphite cells cycled at C/10 and C/24 rates at the indicated temperatures. The solid lines are extrapolations to the origin for the reader convenience.

If it is assumed that the charge consumption in a Li/graphite cell goes into the thickening of the SEI then, with high quality measurements, one should be able to roughly calculate its growth rate. However, these calculations should only be considered approximations, because assumptions about the average molar volume of the Li bi-products forming the SEI, V_m, need to be made. Assume that the majority of the SEI is formed from Li_2CO_3, (or a similar product) which has a measured molar volume, V_m, of 3.5 x 10^{-5} m^3/mole. The increase of the SEI thickness for the N^{th} cycle, Δx, can then be expressed as follows:

$$\Delta x = \frac{3600\,{}^{C}\!/_{Ah}\,\Delta_C V_m}{A_E F}, \tag{8.5}$$

where A_E is the specific surface area of the electrode and F is Faraday's constant. The specific surface areas of MCMB and carbon black were measured to be 0.7 m^2/g and 43.0 m^2/g respectively. Table I shows that the measured specific surface area of the electrodes did not equal the expected values based on the ratio of the electrode components. Presumably the PVDF had the effect of reducing surface area. Thus the measured A_E for the 86:7:7, 90:5:5 and 95:3:2 electrodes were found to be 2.6 m^2/g, 2.4 m^2/g and 1.8 m^2/g respectively.

Table 8.1 The expected and measured specific surface areas (SSA) of three graphite electrodes. The weight to weight ratios of the active material (MCMB), carbon black and binder used in the graphite electrodes were 86:7:7, 90:5:5 or 95:3:2. Presumably the PVDF reduces the surface area of the electrodes.

Electrode blending Ratio	**Expected SSA (m^2/g)**	**Expected SSA divided by SSA of 95:03:02**	**Measured SSA (m^2/g)**	**Measured SSA divided by SSA of 95:03:02**
86:7:7	3.61	1.85	2.64	1.48
90:5:5	2.78	1.42	2.41	1.35
95:3:2	1.96	1	1.78	1

Figure 8.4 (right hand y-axes) shows the variation of Δx vs $t^{-1/2}$. Although there are some major assumptions made about the molar volume of the SEI products, Figure 8.4 certainly gives the correct SEI thickness growth rate per cycle to within a factor of three or so. After 400 hours of testing ($t^{-1/2}$=0.05), the SEI is still growing at about 0.8 nm per cycle for the cell cycled at C/24 (30^{o}C), or at about 17 pm per hour. The growth rate is larger at 50^{o}C as expected.

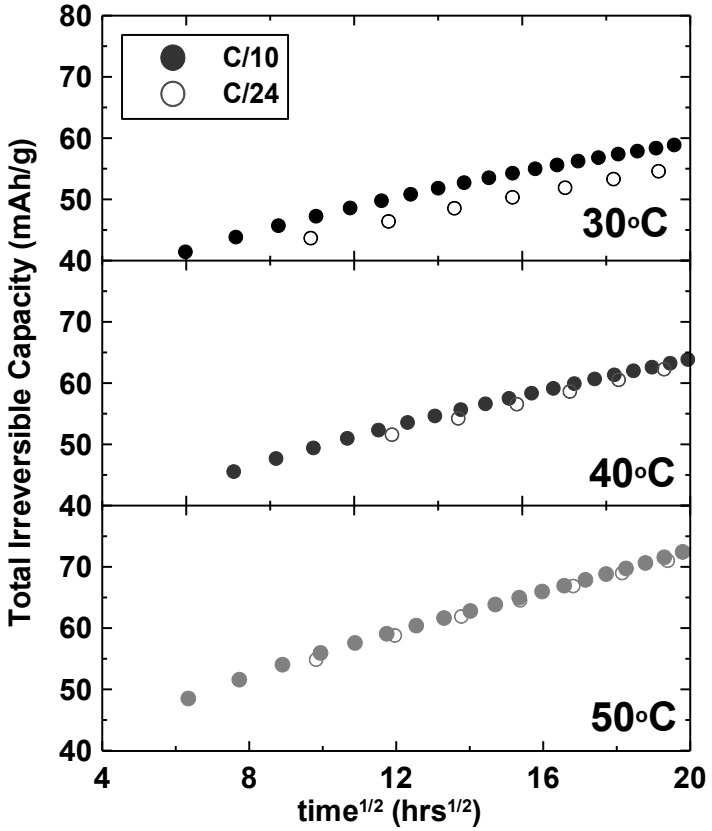

Figure 8.6 The total irreversible *capacity* plotted versus $t^{1/2}$ for the Li/graphite cells charged and discharged at the C-rates and temperatures indicated.

Figure 8.6 shows the total accumulated irreversible *capacity* for the cells described by Figures 8.3, 8.4 and 8.6 plotted versus $t^{1/2}$ according to the predictions of Equation 8.2. The data is quite linear when plotted versus $t^{1/2}$ and the results for cells cycled at either C/10 or C/24 are equivalent, again suggesting that time, not cycle count, is the dominant factor controlling SEI thickening. However, this experiment took only 400 hrs to complete. It might be suggested that this test was too short to observe the true trends of Li consumption by SEI growth. Figure 8.7 shows the irreversible *capacity* per cycle plotted versus $t^{-1/2}$ for a 95:3:2 cell cycling at a rate of C/20 and a temperature of 40°C for 1100 hrs. As in Figure 8.4 the results for the cell are quite linear. Despite the extra time the cell has been cycling the irreversible *capacity* of the cell continues to

extrapolate to the origin at infinite time. The cell was not cycled any longer than this, due to the limited channels available on the HPC.

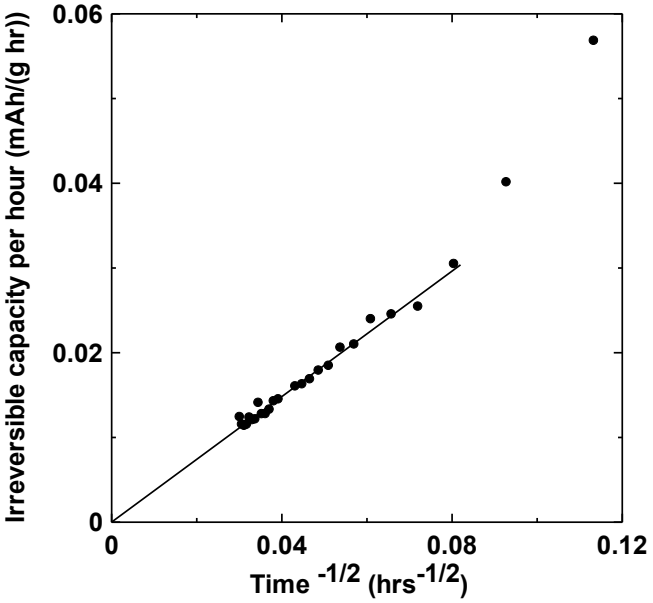

Figure 8.7 Irreversible *capacity* per cycle plotted versus $t^{-1/2}$ for Li/graphite coin cells cycled at a rate of C/20 and a temperature of 40°C for 1100 hrs. The solid lines are extrapolations to the origin for the reader's convenience.

To explore the impact of adding carbon black to graphite electrodes, Figure 8.8 compares precision cycling results of 86:7:7, 90:5:5, and 95:3:2 electrodes cycling at a rate of C/26 and a temperature of 30°C. Figure 8.8A shows the total accumulated irreversible *capacity* versus $t^{1/2}$ (top x-axis). Figure 8.8B shows the irreversible *capacity* per cycle plotted versus $t^{-1/2}$ (bottom x-axis) and Figure 8.8C shows the irreversible *capacity* per cycle per unit surface area versus $t^{-1/2}$. The 95:3:2 electrode shows less irreversible *capacity* (Figure 8.8A) and a slower growth in irreversible *capacity* (Figure 8.8B). However, when the irreversible *capacity* growth rate is normalized for the active electrode surface area (Figure 8.8C), all the electrodes are equivalent. Therefore, the SEI growth occurs on the graphite and carbon black surfaces at approximately the same rates.

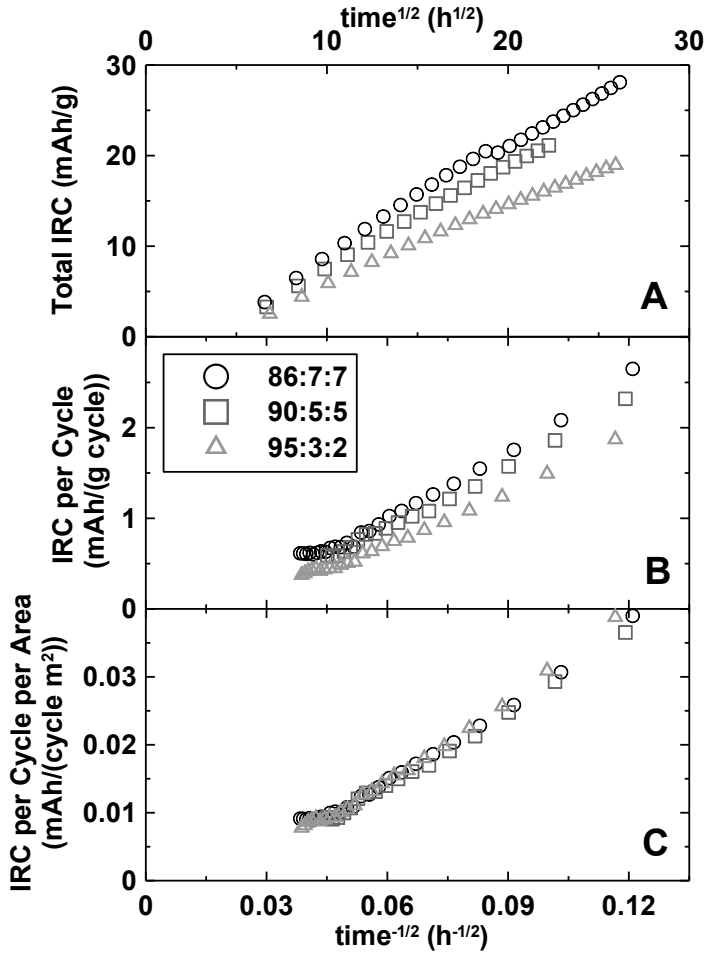

Figure 8.8 Precision coulometry results for Li/graphite cells with 86:7:7, 90:5:5 and 95:3:2 electrodes cycled at C/26 and at a temperature of 30°C. A) The total accumulated irreversible *capacity* versus $t^{1/2}$ (top x-axis); B) The irreversible *capacity* per cycle plotted versus $t^{-1/2}$ (bottom x-axis); C) The irreversible *capacity* per cycle per unit surface area versus $t^{-1/2}$.

The results in Figure 8.8 strongly show that negative electrode specific surface area should be minimized in Li-ion cells destined for long-life applications. This, in turn, suggests that much of the "hype" in the literature about the importance of carbon nano tubes, Si nanowires [114,115], etc. for advanced negative electrodes for Li-ion batteries is simply unfounded.

High Precision Coulometry allows the loss of lithium to the SEI on graphite electrodes to be effectively studied in a relatively short time frame by contrast to the

extended storage and cycling experiments normally used in the literature. It is our opinion that the effects of electrolyte additives on a single electrode can be conveniently studied in simple experiments like those described here, eliminating the need for extensive storage and/or cycling tests. Our results were shown to be similar to literature results collected on cells that were stored and monitored for long time periods.

The $t^{1/2}$ model has worked well in explaining the growth of the SEI on graphite electrodes for the period of one month. However, under certain conditions this simple parabolic model may not hold as well. In the case where a negative half cell is cycled for an infinitely long time it is believed that the irreversible *capacity* will not reduce to zero. Parasitic reactions inside the cell may cause continual damage the SEI and require additional active Li to repair it. This will cause the irreversible *capacity* to level out at some value greater than zero. Damage to the SEI can also be caused by large changes in the volume of the active material, such as in Si and Sn based electrodes [116]. When the volume of the electrode changes greatly, the SEI can become cracked and deformed and thus Li products will be used to repair it. A similar effect could also be observed during the high rate cycling of electrode materials which experience small over-all changes in volume, so long as the volume of the material changes so quickly that the SEI is deformed. Precision coulometry methods could also be used to study these scenarios.

Chapter 9 Short and Long-Term Cycling of Li-Ion Cells

Here, the HPC was used to study the *capacity* retention and CE of commercial $LiCoO_2$, $LiFePO_4$, $Li[Ni_{1/3}Mn_{1/3}Co_{1/3}]O_2$ and $LiMn_2O_4$/graphite cells cycled at low rates and at various elevated temperatures. It is shown that the parasitic reactions that take place within Li-ion batteries consume charge at a fixed (temperature dependent) rate at all temperatures studied, independent of the cycling rate. Consequently, cell life at elevated temperatures is controlled by the time of exposure, so long as the cells are being cycled. After this study the $LiCoO_2$/graphite cells were moved to a traditional battery testing system where they began long term cycling. This was done to confirm that their *capacity* versus time plots, not *capacity* versus cycle number plots, were identical. dV/dQ analysis was then used to understand the different failure mechanisms occurring inside the cell.

9.1 Experiment

Four types of commercial Li ion cells were obtained from reputable suppliers to perform these tests. Twelve each of 18650-size $LiCoO_2$/graphite cells (2400 mAh) and $LiMn_2O_4$/graphite (1400 mAh) cells were cycled between 3.0 and 4.2 V. Twelve 26700-size $LiFePO_4$/graphite cells (2200 mAh) were cycled between 2.7 and 3.8 V. Twelve 18650-size $Li[Ni_{1/3}Mn_{1/3}Co_{1/3}]O_2$/graphite cells (2000 mAh) were cycled between 3.0 and 4.1 V. Each type of cell was cycled on the HPC using applied currents of 100, 50 or 25 mA at temperatures of 30.0, 40.0, 50.0 or 60.0^{o}C. This provided a wide selection of temperatures and rates to observe trends in the behavior of the cells.

After approximately 1000 hours of testing on the HPC the $LiCoO_2$/graphite cells were moved to an E-One Moli Energy computer-controlled battery tester. The cells continued to cycle on the Moli battery tester with the same voltage limits and applied currents as before, but the controlled temperature of the cells was changed to 55°C due to the available thermostats attached to the Moli battery tester. The long term cycling test lasted approximately 12500 hours or ~17.5 months. After the long term cycling test was completed, all of the cells were cycled once more with an applied current of 25 mA so that the cells could be compared without impedance-related differences

The half cells for dV/dQ analysis were made from a fresh $LiCoO_2$/Graphite 18650 cell which was discharged to 1.0 V and held there for several hours before recovering its electrodes. Discharging the cell to 1.0 V allowed for the positive and negative electrodes to become as lithiated ($LiCoO_2$) or delithiated (graphite) as possible, respectively, without damaging the negative electrode copper current-collector. The recovered electrodes were washed in dimethyl carbonate and one side of the double-sided electrodes was carefully wiped clean to remove the electrode material from the current collector. 12.6 mm diameter electrodes were cut with a precision punch from the cleaned electrodes and used to construct Li/graphite and Li/$LiCoO_2$ coin cells. The half cells were cycled at a rate of C/50 between 1.2 and 0.005V for the Li/graphite cell and 4.3 and 3.0 V for the Li/$LiCoO_2$ cell, both at a temperature of 60.0^{o}C. As discussed in Chapter 6 the dV/dQ analysis program could then use the measured dV/dQ(Q) from the positive and negative half cells as "reference" data for the positive and negative electrodes.

9.2 Short Term Cycling Results

Figure 9.1 shows the cell voltage versus capacity of the four types of commercial cells cycled with an applied current of 100 mA at a temperature of 40°C. The larger panels for each cell show the 1st, 5th, 10th, etc. cycles over the entire voltage window. The smaller insets on the left and right show expanded views of the discharge and charge endpoints, respectively, for the 2nd, 4th, 6th, 8th and 10th cycles. The capacity axis tracks the accumulated capacity of the cells, assuming that the capacity of the cell after the very first discharge was 0.00 mAh. All endpoints continually move to the right as Li-ion cells are tested.

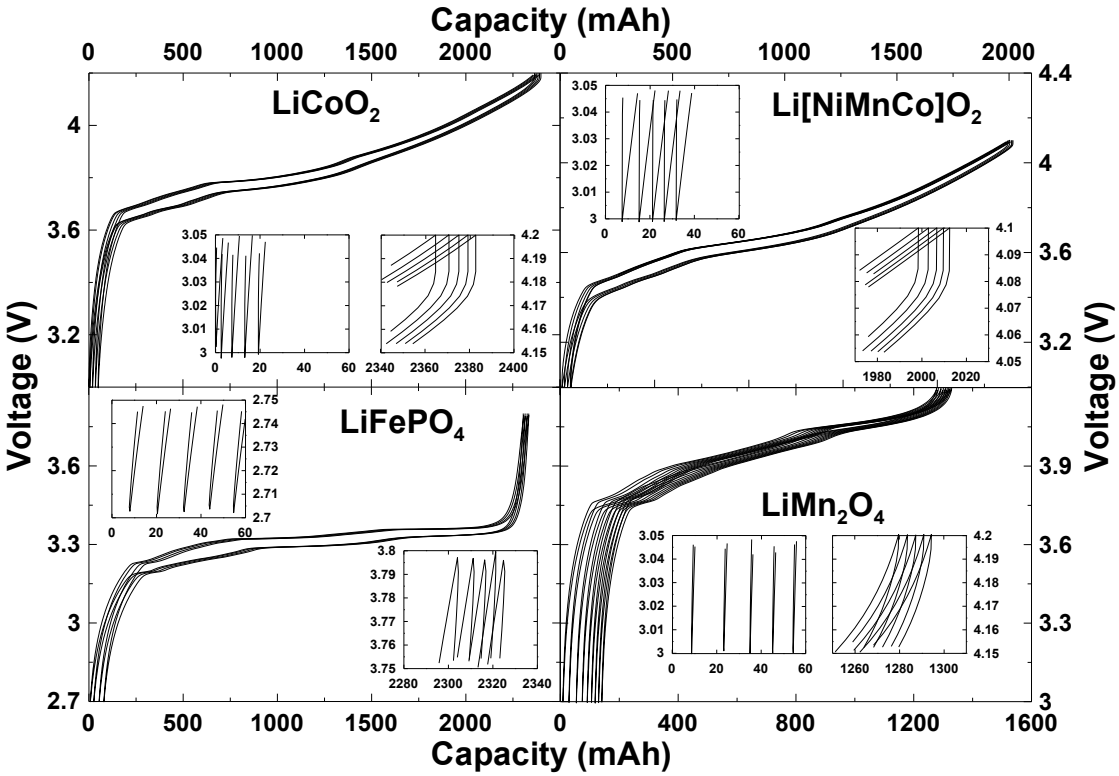

Figure 9.1 Voltage-capacity graphs for $LiCoO_2$, $Li[Ni_{1/3}Mn_{1/3}Co_{1/3}]O_2$, $LiFePO_4$ and $LiMn_2O_4$/graphite Li-ion cells charged and discharged with a current of 100 mA and at a temperature of 40°C. The insets show the motion of the charge and discharge endpoints for every second cycle.

Figure 9.2 shows the normalized *capacities* for all of the cells plotted versus cycle number. The *capacity* fade of all the cell chemistries increases as the temperature increases. The $LiMn_2O_4$ and $LiFePO_4$ cells cycled at lower C-rates lose *capacity* faster than those cycled at higher C-rates. The $LiCoO_2$ and $Li[Ni_{1/3}Mn_{1/3}Co_{1/3}]O_2$ cells, on the other hand, are less affected by cycling rate, showing similar *capacity* fade versus cycle count for the different C-rates at the same temperature.

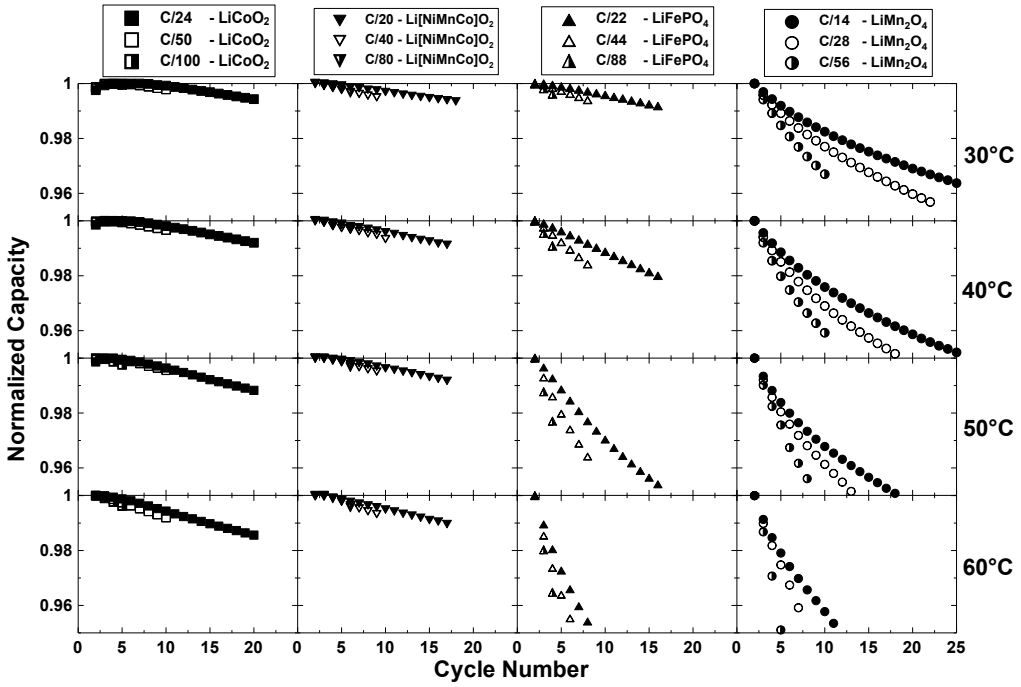

Figure 9.2 Normalized *capacity* versus cycle number of the 48 Li-ion cells charged and discharged at the C-rates and temperatures indicated.

Figure 9.3 shows the CE versus cycle number for the same cells described by Figure 9.2. The CE is strongly affected by temperature for all the cells, so that as the temperature increases, the CE departs more and more from unity. This is because parasitic reactions like electrolyte oxidation and loss of Li to SEI growth are amplified as temperatures are elevated. Figure 9.3 shows that cells cycled at lower rates had CEs which departed further from unity than cells cycled at faster rates. This is because cells

cycling at lower rates have more time per cycle for parasitic reactions to occur and consume charge.

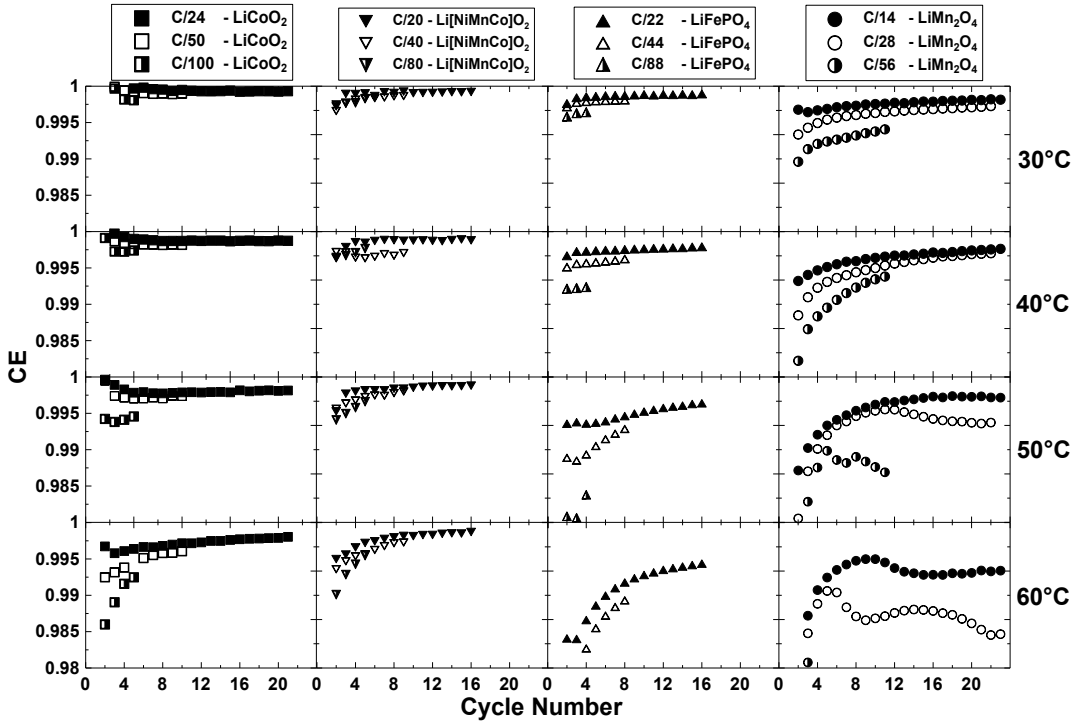

Figure 9.3 Coulombic efficiency versus cycle number for the 48 Li-ion cells charged and discharged at the C-rates and temperatures indicated.

Figure 9.4 shows the coulombic inefficiency (1.0000 - CE) divided by the time of one charge-discharge cycle plotted versus time, for the same cells described by Figures 9.2 and 9.3. The coulombic inefficiencies per hour for cells at a given temperature are almost exactly the same at any given time, irrespective of the cycling rate, suggesting that time, not cycle count, is the dominant contributor to charge loss. This suggests that at a given temperature parasitic reactions that cause coulombic inefficiency are occurring in the cells at a reaction rate that is independent of the cell cycling rate. Therefore the amount of parasitic reactions that occur for a given cycle is simply the parasitic reaction

rate multiplied by the time of one cycle. This leads to a general expression for the coulombic inefficiency of any given cycle:

$$(1.0000 - CE) = b(T,t)*(\text{time of one cycle}) \qquad 9.1$$

where b(T,t) is the parasitic reaction rate that depends on the cell temperature, T and calendar time, t.

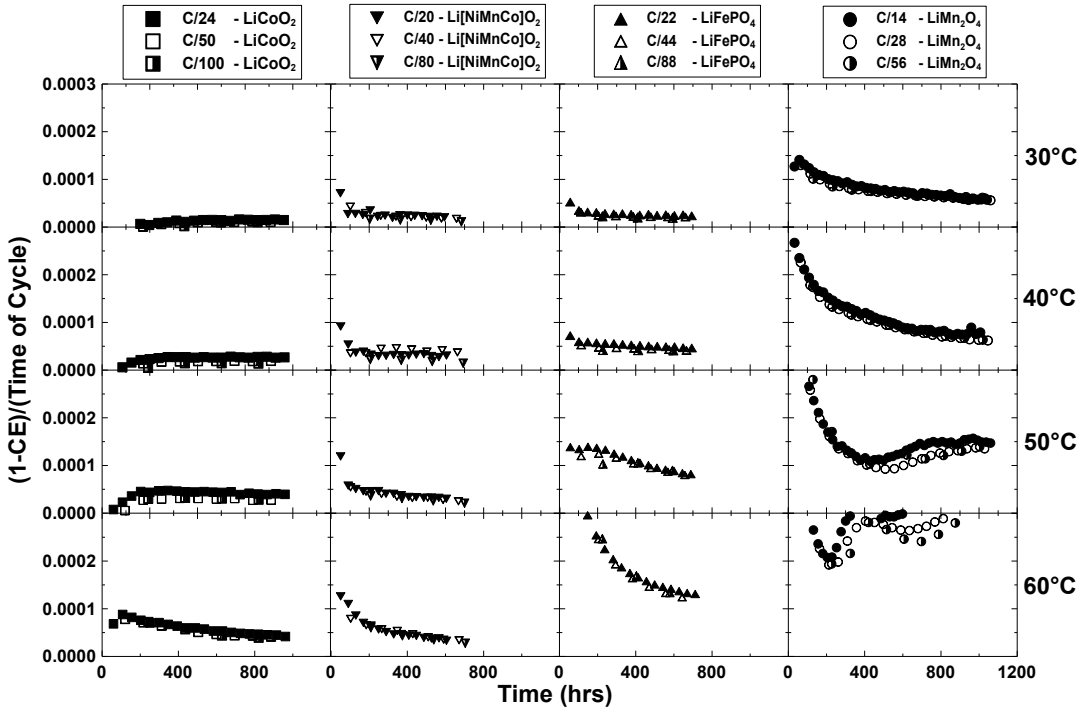

Figure 9.4 Coulombic inefficiency (1.0000 - CE) divided by time of a cycle plotted versus time for the 48 Li-ion cells charged and discharged at the C-rates and temperatures indicated

Impedance growth, which can lead to *capacity* loss during high-rate cycling, is not monitored in such low-rate experiments. This is because the voltage drop associated with the internal impedance in the cell will be small for such low currents. However, we believe the power fade in cells tested at the same temperature for the same time

(described by Figures 9.2, 9.3 and 9.4) will be very similar because those cells each have had the same amount of parasitic loss, leading to the formation of decomposition products on electrode surfaces.

To test the model described by equation 9.1, the CE, for the 4 types of cells after ~600 hrs, is plotted versus the log of C-rate in Figure 9.5. As shown in Figure 9.3, the CE of the cells departed more strongly from unity as the cell temperature was raised or as the cycling rates were decreased. The solid lines in Figure 9.5 are curves fitted to the data using equation 9.1, where it was assumed that b is constant with time for a given temperature. These curves fit the experiments extremely well. Table 9.1 gives the values of b as a result of the curve fitting for the 4 cell types at the 4 temperatures studied. However, one cannot simply assume that increasing cycling rates indefinitely will continue to improve CE. At a significantly high charge rate, physical phenomena like Li plating and impedance changes will reduce *capacity* retention and CE of the cells.

Table 9.1 Parasitic reaction rate, b, ($hours^{-1}$) versus temperature for $LiCoO_2$, $LiFePO_4$, and $Li[Ni_{1/3}Mn_{1/3}Co_{1/3}]O_2$ and $LiMn_2O_4$/graphite Li-ion cells as determined from Figure 9.5. The constant, b, relates the coulombic efficiency (CE) to the time of one cycle by: (1.0000 - CE) = b (time of one cycle).

Temperature /°C	**Cell Types**			
	$LiCoO_2$ b (h^{-1})	**$LiFePO_4$ b (h^{-1})**	**$LiMn_2O_4$ b (h^{-1})**	**$Li[NiMnCo]O_2$ b (h^{-1})**
30	0.0000110	0.0000221	0.0000600	0.0000195
40	0.0000187	0.0000448	0.0000746	0.0000220
50	0.0000296	0.0000886	0.0001122	0.0000278
60	0.0000465	0.0001318	0.0002135	0.0000355

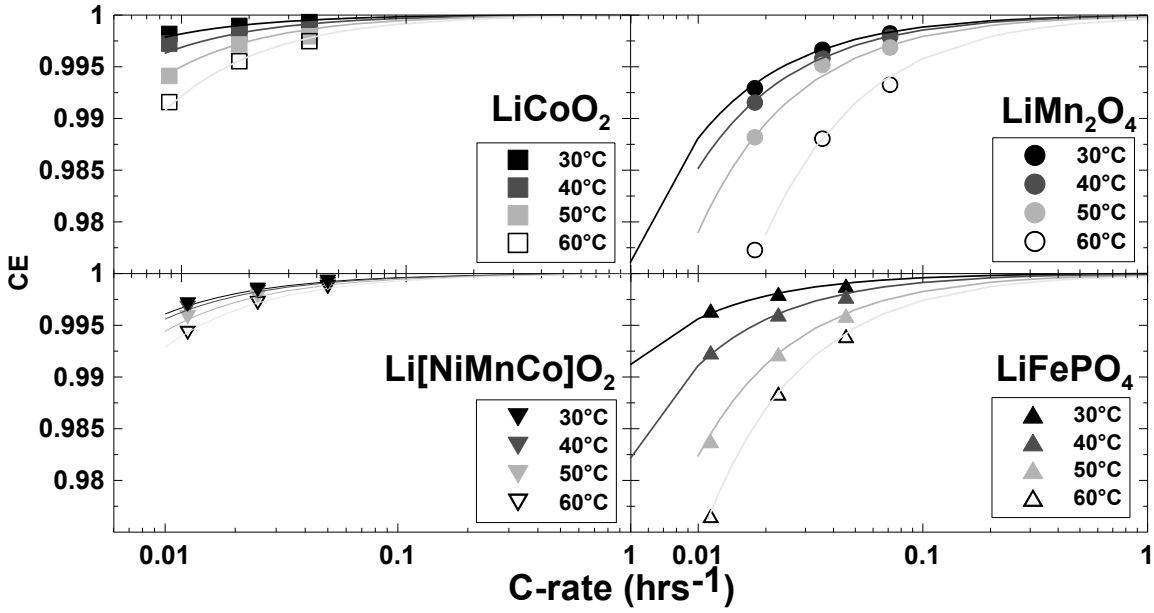

Figure 9.5 Coulombic efficiency versus C-rate for the 48 Li-ion cells tested at 30, 40, 50 and 60°C. The CE data were selected after 600 hours of testing. The solid lines are fits of: (1.0000 - CE) = b*(time of one cycle), to the data, where b is a constant. b increases with temperature as shown in Table 9.1.

9.3 Long Term Cycling Results

Figure 9.6 shows the fractional *capacity* versus cycle number for the $LiCoO_2$/Graphite cells that were cycled on the HPC at 60°C during the ~12500 hr test on the Moli battery tester. Cells cycled at lower rates displayed a larger *capacity* loss per cycle than cells cycled at faster rates, as predicted by the short term cycling test in Figures 9.2. The noise in the data was caused by multiple power outages over the ~17.5 months of testing. Arrows in Figure 9.6 mark the location of a change of slope in the *capacity*-cycle number plots.

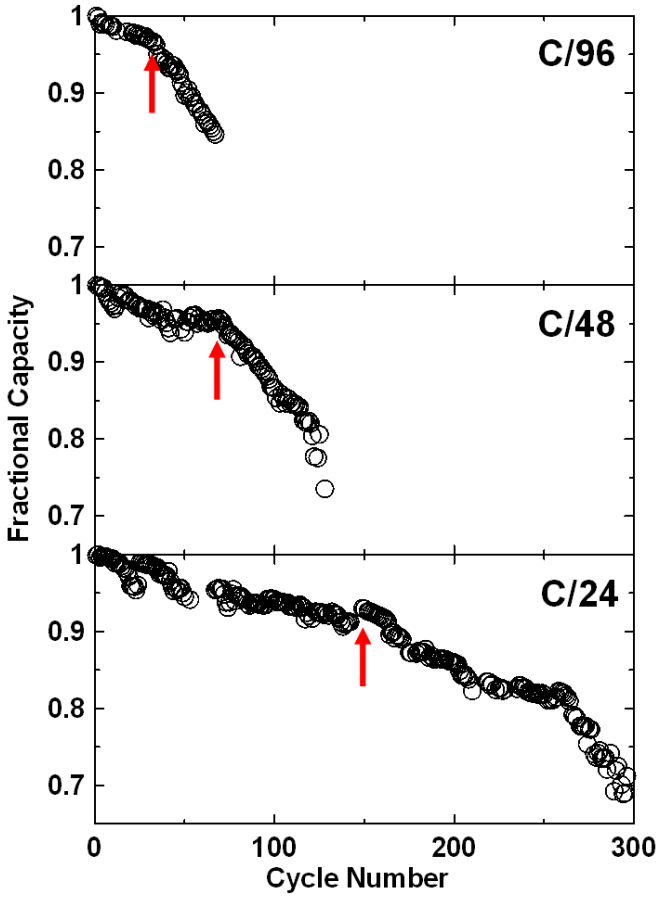

Figure 9.6 Fractional *capacity* versus cycle number for the three $LiCoO_2$/graphite cells cycled at 55°C and at rates of C/24, C/48 and C/96 as indicated. The arrows mark a change in slope in the *capacity* versus cycle number plots.

Figure 9.7 shows the fractional *capacity* versus time for the same cells in Figure 9.6. When plotted versus time, the three cells cycling at different rates show almost identical behaviors. In fact, the arrows in Figure 9.7, indicating the change of slope in the *capacity* loss of the cells (see Figure 9.6), occur at almost exactly the same time. This confirms the predicted results based on Figure 9.4 that time is the principal parameter affecting the degradation of these cells tested at low rates at 55°C. Figure 9.7 also shows the *capacity* of all three cells cycling at a rate of C/96 for the final cycle (star-shaped data point). The *capacity* of the two fastest cycling cells increased when the rate was reduced

and the *capacity* of all three cells was very similar. This suggests that impedance-related effects were responsible for some of the *capacity* loss in these cells after long times.

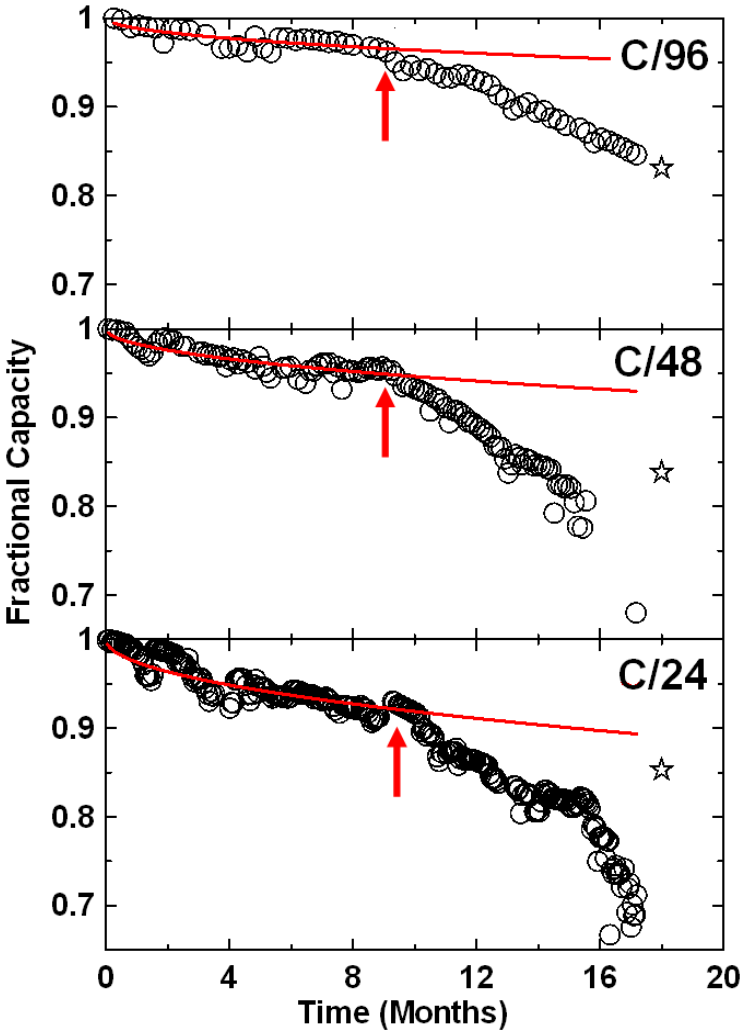

Figure 9.7 Fractional *capacity* versus time for the three $LiCoO_2$/graphite cells cycled at 55°C and at rates of C/24, C/48 and C/96 as indicated. The arrows mark a change in slope in the *capacity*-time plots. The arrows are positioned at the same cycle numbers as in Figure 9.6. The solid curves are fits of equation 9.2 for the first nine months of the data.

The results in Figure 9.7 **do not** show *capacity* loss versus time behavior that can be described as:

$$Q = Q_o(1 - At^{1/2}) \tag{9.2}$$

over the entire cycling history**.** As discussed in Chapter 8 the $t^{1/2}$ behavior is characteristic of the parabolic growth of the SEI [36,117]**.** In a situation where the graphite electrode is the limiting electrode at the bottom of discharge, the lithiated state of the positive electrode becomes less and less as cycling proceeds since there is less lithium available to be extracted from the negative electrode. If only the data for the first nine months is considered, the $t^{1/2}$ law fits the data relatively well as shown by the solid curves in Figure 9.7**.** It will be shown later below why the $t^{1/2}$ law does not fit the entire data sets. Additionally, and importantly, **the prediction that these cells would all fail at the same time**, based on the CE measurements in Figure 9.4, **does not rely on any particular model of *capacity* loss**.

Figure 9.8 shows the voltage versus *capacity* of the $LiCoO_2$/Graphite cell cycling at a rate of C/24 for the 200th (12 months), 250th (15 months), 275th (16.5 months) and 296th (17.5 months) cycles measured during the recharge half-cycle. The voltage profiles of the 200th cycle and 250th cycles were very similar apart from some *capacity* loss. This suggests that the cell was able to cycle for about 15 months without any significant increase in impedance before the onset of its steep *capacity* fade. The voltage profiles of the 250th, 275th and 296th cycles show a steady increase in the average voltage of the cell. This confirms that the steep *capacity* fade observed in Figure 9.7 after 15 months of testing was a result of an increase in impedance. Most likely the electrolyte in the cell had become severely depleted by continual oxidation reactions at the positive electrode or the positive electrode had been severely damaged by the continual oxidation occurring there.

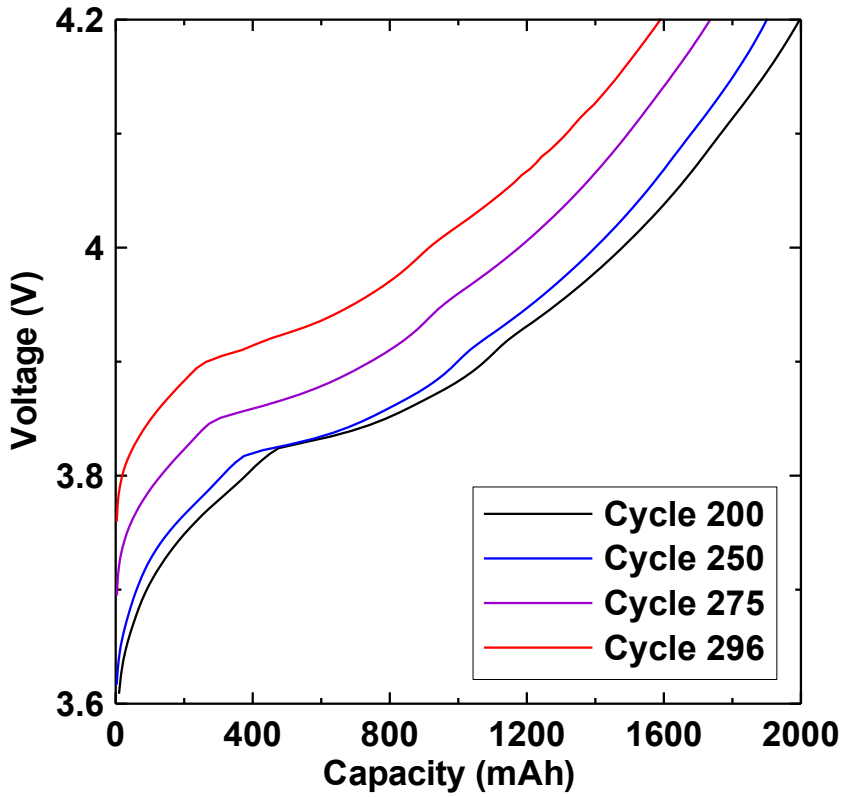

Figure 9.8 Voltage versus capacity plots for cycles 200, 250, 275 and 290 measured during the charge cycle of the cell cycled at C/24 at 55°C. An impedance increase is observed after cycle 250.

Figure 9.9 shows dV/dQ versus Q for the experimental data (black) and that calculated using Equation 6.2 (red) for selected cycles of the same $LiCoO_2$/graphite cells shown in Figures 9.6 and 9.7. The calculated dV/dQ versus Q curves match the experimental curves quite nicely over the entire testing period.

Figure 9.10 shows positive and negative electrode reference potential-capacity curves and the resulting calculated Li-ion cell voltage-capacity curve for selected cycles of the cell cycled at a C/24 rate. The electrode masses and slippages used in Figure 9.10 are those that gave the best fits in Figure 9.9. As a reminder, the point Q = 0 is taken as the point where the **experimental** cell reaches the fully discharged state. Figure 9.10 shows that the fitted V(Q) curve (top panel) reaches the 3 V discharge cutoff within

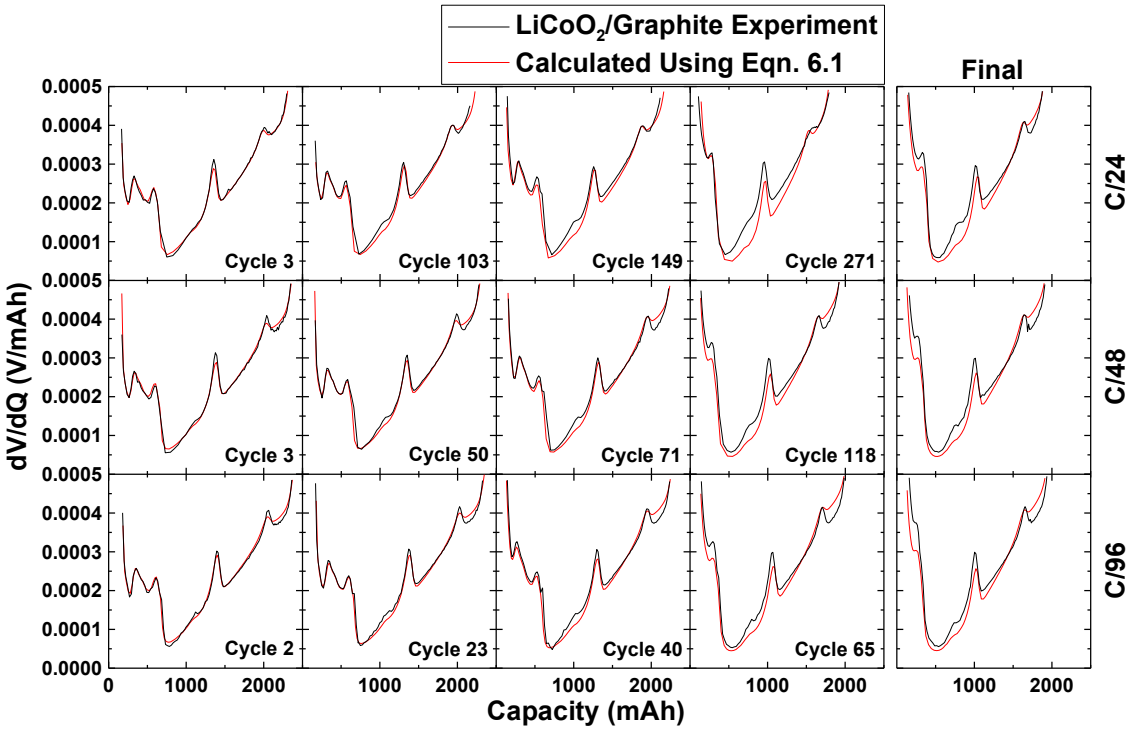

Figure 9.9 Experimental and calculated dV/dQ versus Q for $LiCoO_2$/graphite cells at the cycle numbers indicated for the cells cycled at C/24 (top row), C/48 (middle row) and C/96 (bottom row) at 55°C. The red curves are the fits to the data using Equation 6.2 and the procedure described in Chapter 6. In all cases the final cycle (last column) was collected at a rate of C/96.

40 mAh, (or within 2% of the total cell *capacity*) for all the cycles considered, demonstrating the quality of the fits. Figure 9.10 (see the right panels) shows that for cycles 1-150, the negative electrode is the limiting electrode at the bottom of discharge. During this period the relative slippage of the positive electrode slips to higher relative capacity faster than the negative electrode. By cycle 150, the negative electrode and the positive electrode are almost empty and almost full of lithium, respectively, when the cell is fully discharged. For cycles 150 – 300, the negative electrode is no longer emptied and the positive electrode is filled when the Li-ion cell is fully discharged.

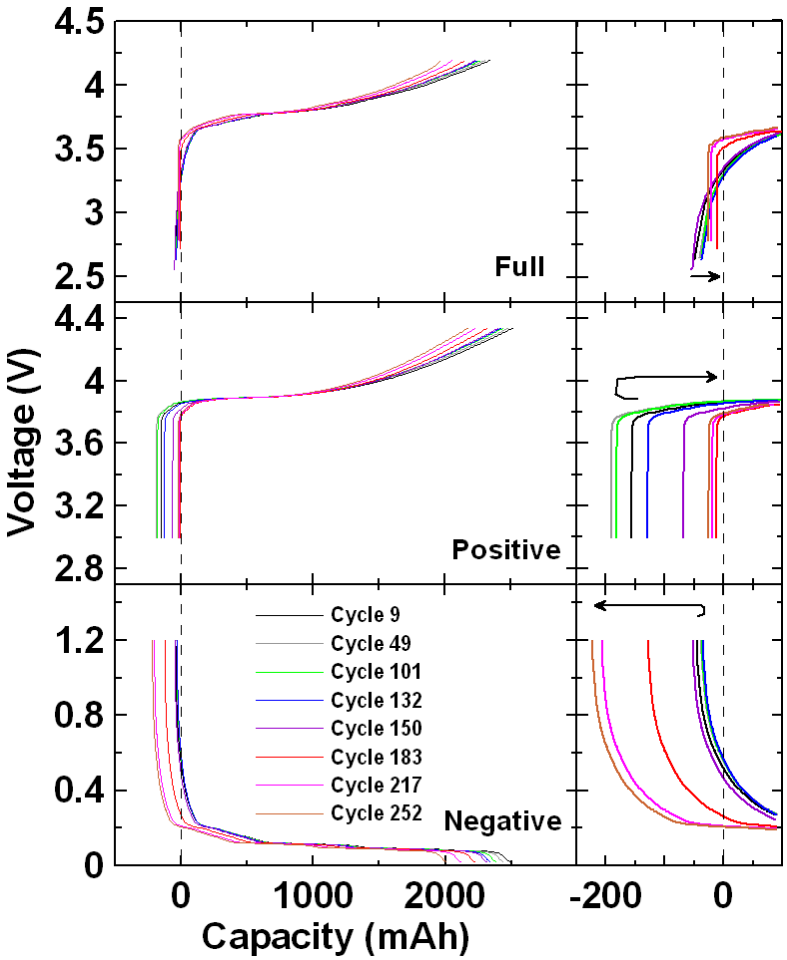

Figure 9.10 Top panel) Calculated $LiCoO_2$/graphite V(Q) curves for the cell cycled at C/24 at 55°C during the indicated recharge cycles. Middle and bottom panels) Extracted V(Q) curves for the positive and negative electrodes, respectively, from the dV/dQ analysis software which developed the fits shown in Figure 9.9. The right inset panels show an expanded view of the region near Q = 0 to demonstrate the change in behaviour that occurs near cycle 150.

Figure 9.11 shows the relative capacities of: the graphite reference electrode when it was empty and full of lithium (red curves); the Li_xCoO_2 reference electrode when it reached 4.3 V and when it was full of lithium (blue curves); and the *capacity* of the experimental cell in the charged state (black curve), all plotted versus time for the three $LiCoO_2$/graphite cells in this study. As an example, the relative capacity endpoints of the reference curves in Figure 9.10 are the points plotted in Figure 9.11 for the positive and

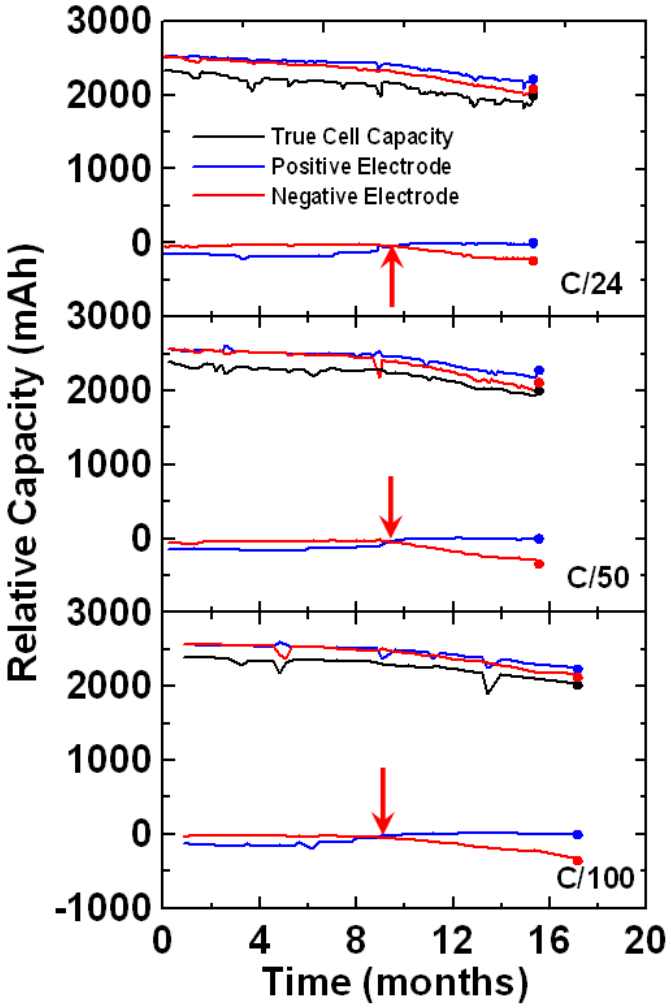

Figure 9.11 The relative capacities of: the graphite reference electrode when it was empty and full of lithium (red curves); the Li_xCoO_2 reference electrode when it reached 4.3 V and when it was full of lithium (blue curves); and the *capacity* of the experimental cell in the discharged (Q = 0; no curve is plotted on the Figure for this case) and charged state (black curve), all plotted versus time for the three cells in this study.

negative electrodes. Figure 9.11 shows that the experimental cell reaches a full state of charge (4.2 V) before the positive electrode reaches 4.3 V vs. Li (upper blue curve in all panels) and before the negative electrode is completely filled (upper red curves in all panels). Figure 9.11 shows that the *capacity* of both the positive and negative electrodes decreases slowly over time (*capacity* difference between the two red curves or between

the two blue curves) due to a loss in electrically connected active mass. Figure 9.11 also shows that the electrode which determines the fully discharged state switches from the negative electrode to the positive electrode around 9 months, as indicated by the red arrows. The positions in time of the red arrows in Figure 9.11 coincide with the positions of the red arrows in Figure 9.7. Therefore the change in the rate of *capacity* loss with time in Figure 9.7 occurs when the positive electrode full lithiation point slips past the negative electrode full delithiation point.

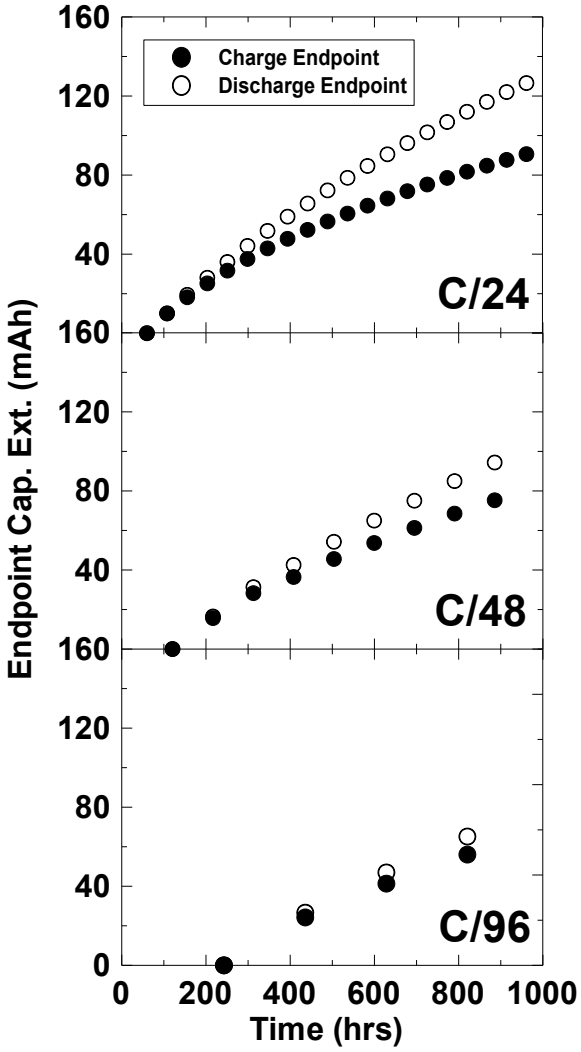

Figure 9.12 Charge and discharge *capacity* endpoint extent graphs for the three $LiCoO_2$/graphite cells in the short term test carried out on the HPC. The endpoints have been normalized to begin at zero for the first cycle.

Positive electrode slippage can only occur if electrolyte oxidation is occurring**.** Figure 9.12 shows the charge and discharge endpoint *capacities* plotted versus time for the three $LiCoO_2$/graphite cells during the short term testing on the high precision charger. It is clear that the charge endpoint is continually slipping to higher *capacities* for these cells. It appears that in these cells, an electrolyte additive combination has been used to approximately match the initial electrode slippage rates so that minimal *capacity* fading was initially observed by the user [118]. The data in Figure 9.12 can be used to create an approximate picture of the absolute *capacities* of the electrodes during the cycling of the cells.

Figure 9.13 shows the approximate absolute *capacities* of the electrodes and the Li-ion cells in the charged state plotted versus time. The curves in Figure 9.13 were obtained by adding the average charge endpoint slippage rate (averaged over the last 400 hours for the 3 cells in Figure 9.12) of 0.089 mAh/h to each of the curves in Figure 9.11. The overall motion to higher absolute *capacities* is caused by the continual electrolyte oxidation in the cells. This oxidation consumes electrolyte, thickens passive films and presumably leads to the impedance increase observed beyond 15 months of testing. The addition of a constant slippage rate to all the curves in Figure 9.11 to obtain the curves in Figure 9.13 is only an approximation. Ideally, it would have been best if all the long term cycling results had been collected on the HPC so that the endpoint *capacities* could be tracked throughout the entire duration of the cycling. Unfortunately, we do not have the resources to do this.

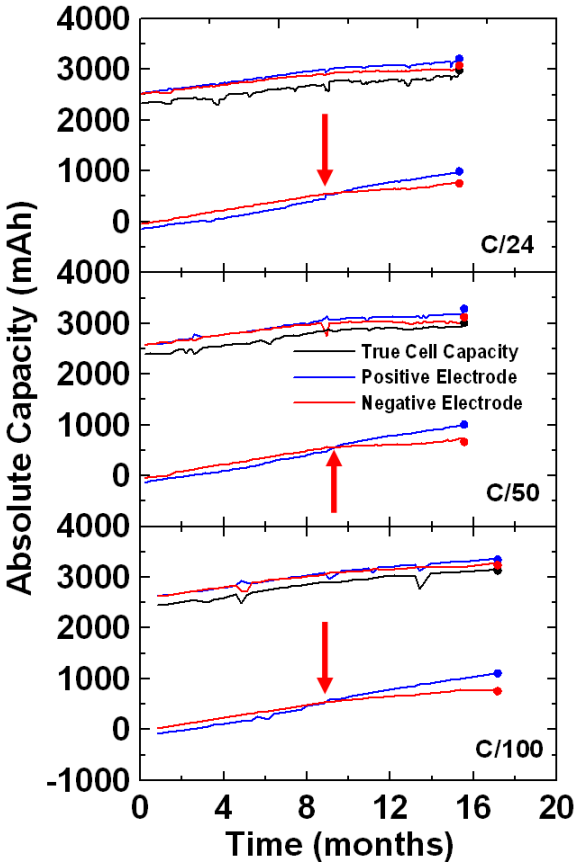

Figure 9.13 The approximate absolute *capacities* of: the graphite reference electrode when it was empty and full of lithium (red curves); the Li_xCoO_2 reference electrode when it reached 4.3 V and when it was full of lithium (blue curves); and the *capacity* of the experimental cell in the discharged (Q = 0) and charged state (black curve), all plotted versus time for the three cells in this study. Figure 9.13 was obtained from Figure 9.11 by adding 0.089 mAh/h slippage to all curves in Figure 9.11.

Chapter 8 showed that the growth of the SEI could be explained by the parabolic growth law, and thus Li lost to the SEI will decrease with $t^{1/2}$. **If** one assumes that the other parasitic currents are constant over time, then one can develop a qualitative picture of the *capacity* loss mechanisms inside the cells. Figure 9.14 shows the schematic of the electrodes in a $LiCoO_2$/graphite cell versus time for a cell cycled at low rates and elevated temperatures. The negative to positive electrode *capacity* ratio was set to be initially greater than 1 in agreement with Figure 9.10 that shows that the negative

electrode never fills completely. The negative electrode slippage shows curvature due to the slowing of SEI growth with time. Figures 9.10 and 9.11 show that that the negative electrode was completely delithiated during each cycle for the first 9 months, but after 9 months it was not. Instead, after 9 months, the positive electrode was completely filled. This crossover in behavior is captured by the arrow in Figure 9.14. Therefore, the change in slope in Figure 9.7, as indicated by the arrows, was caused when the end of discharge *capacity* was no longer controlled by the emptying of the Li_xC_6 but by the filling of the $LiCoO_2$. Figures 9.13 and 9.14 show similar features and we believe that Figure 9.14 represents a useful summary of the results of this work that can be used as a model by other researchers.

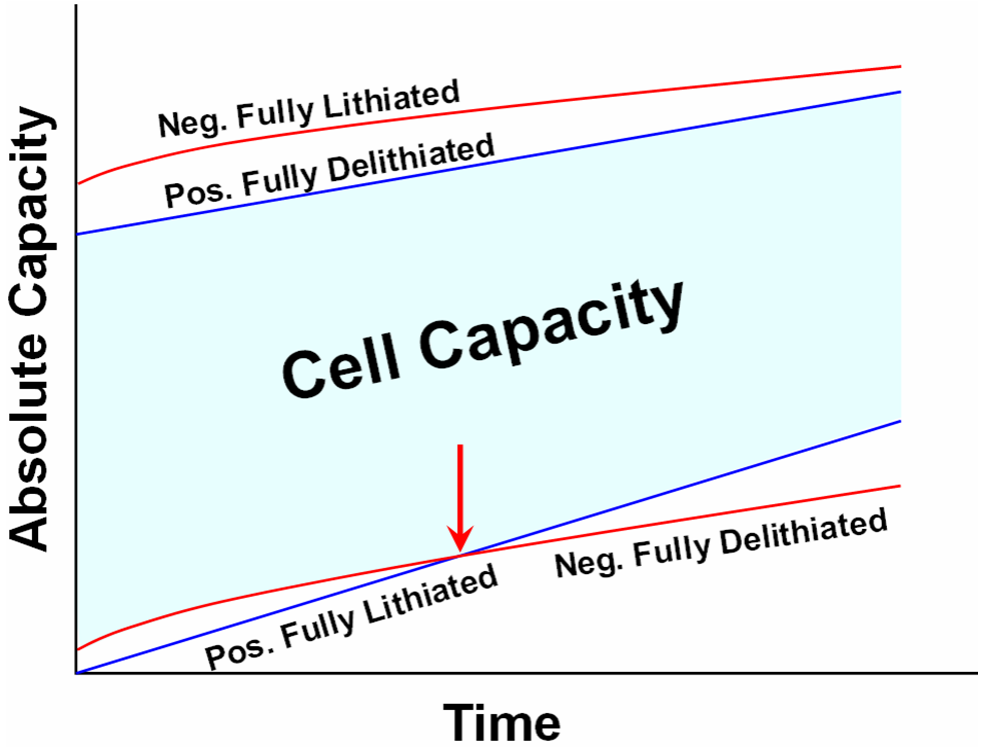

Figure 9.14 Schematic showing how the absolute *capacities* of the positive and negative electrode charge and discharge endpoints evolve with time for the $LiCoO_2$/graphite cells tested for 17 months at 55°C. The resulting cell *capacity* is indicated by the shaded region.

Most interesting in this analysis is that all three experimental cells reached the change in slope designated by the arrows in Figure 9.7 at the same time and **not** at the same cycle number. This shows that mechanical degradation, which would increase with cycle number, is not responsible for the positive electrode *capacity* loss. Instead, it is the continual electrolyte oxidation, evidenced by the imperfect coulombic efficiency shown in Figure 9.4 and the charge endpoint slippage in Figure 9.12, which was responsible for the damage to the positive electrode. When electrolyte is oxidized, charge balance requires an associated charge transfer process to occur, e.g., transition metal dissolution, Li insertion or some other process. This work shows that this process is occurring at the same rate for all three cells, despite the different cycling rates.

Chapter 10 Narrow Range Cycling and Storage of Li-Ion Cells

Capacity loss in Li-ion cells occurs because of chemical degradation involving reactions between electrode materials and electrolyte and mechanical degradation caused by the lack of (or poor) electrical contact to all active particles in the electrodes. The cycling performance of the various electrodes and electrolyte chemistries has been extensively studied. However, many of these tests use high rate cycling [1–5], and are performed over the space of only a few weeks, thus the *capacity* loss may mostly reflect mechanical degradation because the time for chemical degradation is limited. Some of these tests include studies of the impact of charge-discharge cycling to different voltage limits [119–125]. Conversely, there have only been a few published results that test cycle life performance over a period of years [6,7,60,74,107,126]. They demonstrated that the *capacity*, power, internal pressure and impedance of Li-ion cells are strongly dependent on the age of Li-ion cells.

Here, the HPC and a custom storage system were used to study parasitic reactions in common types of Li-ion cells. The cells were cycled between narrow voltage limits near full state of charge and stored at various voltages to observe the effect of temperature and potential on parasitic reactions. It is shown that there is a direct relationship between narrow range cycling results and the *capacity* lost in a cell during storage.

10.1 Experiment

Two types of commercial Li ion 18650 cells were obtained from a reputable supplier to perform these tests. Fourteen each of $LiCoO_2$/graphite cells (2400 mAh), and $Li[Ni_{1/3}Co_{1/3}Mn_{1/3}]O_2$(NMC)/graphite cells (2000 mAh) were obtained. Figure 10.1 shows some typical data collected during the narrow range cycling (Figure 10.1A) and storage tests (Figure 10.1B) of $LiCoO_2$/graphite cells. All narrow range cycling and storage cells were first cycled twice between 3.0 and 4.2 V for the $LiCoO_2$ cells and between 3.0 and 4.1 V for the NMC cells with a current of 100 mA and at a temperature of 30, 40, 50 or 60°C. After the two initial cycles, the narrow range cells were then discharged to the lower voltage limit of the new 100 mV cycling range, where they continued to cycle for at least 400 hrs. Table 10.1 shows the voltage limits and applied currents used during the narrow range cycling of each cell. The advantage of cycling between these narrow limits is that it allows one to probe the impact of the upper potential limit on cell lifetime. The storage cells, on the other hand, were discharged to a voltage of 4.20 V, 4.15 V, 4.10 V or 4.05 V for the $LiCoO_2$ cells or 4.10 V, 4.05 V, 4.00 V or 3.95 V for the NMC cells. The cells were then stored under open circuit conditions for the next 500 hrs at the same temperatures as before, only measuring the cell voltage once every 6 hours. After 500 hrs, the storage cells were cycled two more times with an applied current of 100 mA to measure the *capacity* loss experienced during the storage period, as described in Chapter 5.

All narrow range cycling was performed using the HPC. All storage experiments were performed using the automated storage systems described in Chapter 5.

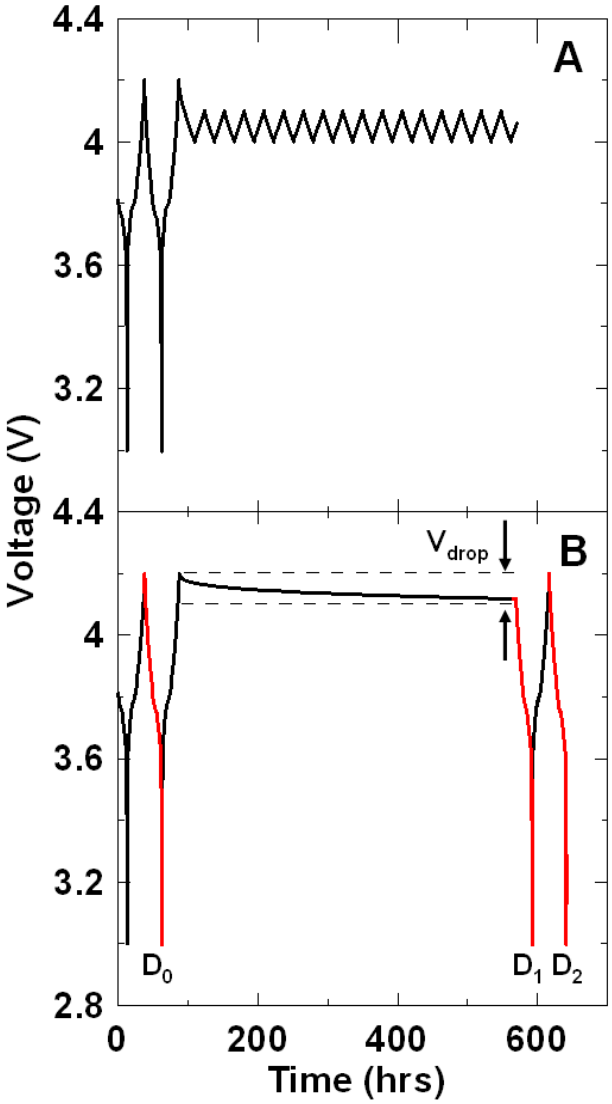

Figure 10.1 Typical data collected during the narrow range cycling (top panel) and storage tests (bottom panel) of $LiCoO_2$/Graphite cells at 30°C

Table 10.1 The voltage limits and applied currents used during the narrow range cycling of the $Li[Ni_{1/3}Co_{1/3}Mn_{1/3}]O_2$ and $LiCoO_2$ /graphite cells.

Cell Type	Voltage Range (V)	Current (mA)	Temperature (°C)
$LiCoO_2$	4.20 – 4.10	19.0	30, 40, 50 & 60
$LiCoO_2$	4.15 – 4.05	19.0	30, 40, 50 & 60
$LiCoO_2$	4.10 – 4.00	19.0	30, 40, 50 & 60
$LiCoO_2$	4.05 – 3.95	19.0	50 & 60
$Li[Ni_{1/3}Mn_{1/3}Co_{1/3}]O_2$	4.10 – 4.00	15.0	30, 40, 50 & 60
$Li[Ni_{1/3}Mn_{1/3}Co_{1/3}]O_2$	4.05 – 3.95	15.0	30, 40, 50 & 60
$Li[Ni_{1/3}Mn_{1/3}Co_{1/3}]O_2$	4.00 - 3.90	15.0	30, 40, 50 & 60
$Li[Ni_{1/3}Mn_{1/3}Co_{1/3}]O_2$	3.95 – 3.85	15.0	50 & 60

10.2 Theoretical Background

Figure 10.2 shows differential voltage (dV/dQ) versus capacity (Q) (top row) for the experimental data (red line) and the theoretical fit (black line) for the first cycle of the cells at 30°C. The theoretical fit was made using the dV/dQ analysis program described

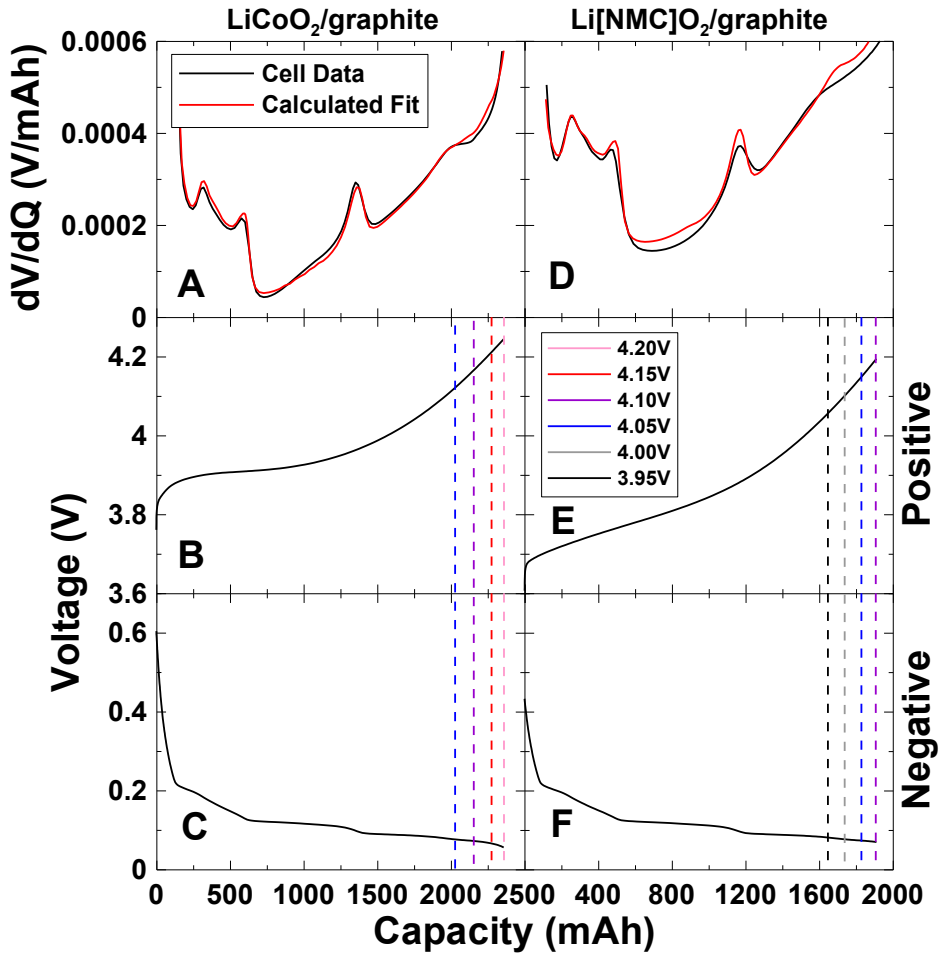

Figure 10.2 Top row) dV/dQ versus capacity for the experimental data (red line) and the theoretical fit (black line) for the first cycle of the $LiCoO_2$/graphite (left column) and $Li[Ni_{1/3}Mn_{1/3}Co_{1/3}]O_2$/graphite cells (right column) at 30°C. Middle and bottom rows) Extracted V(Q) curves for the positive and negative electrodes, respectively, from the dV/dQ analysis software which developed the fits shown in the top row. Dashed vertical lines have been added to the middle and bottom rows to indicate the *capacities* of the positive and negative electrodes at the top of the various narrow voltage ranges.

in Chapter 6.3. The theoretical dV/dQ curves match the experimental curves very well suggesting that the model is good and that the relative electrode *capacities* are correct. The reference voltage-capacity curves of the positive and negative electrodes versus Li are shown in the 2nd and 3rd rows of panels in Figure 10.2. These curves have been positioned so that the calculated dV/dQ versus Q matches the experimental dV/dQ versus Q curves. Figure 10.2 shows that above a full cell terminal voltage of 3.9 V, the potential of the negative electrode versus Li/Li^+ remains fairly constant with state of charge compared to the positive electrode. Dashed vertical lines have been added to the 2nd and 3rd rows of panels in Figure 10.2 to indicate the *capacities* of the positive and negative electrodes at the top of the various narrow voltage ranges which are probed in the experiments of this paper.

In Chapter 3 a Li inventory model was introduced to account for the loss of Li to the most common parasitic processes in Li-ion cells. Using Table 3.3 and the derivations in Appendix A, the measured quantities of CE, Δ_D, Δ_C and Fade for a cell cycling between narrow voltage limits (Figure 3.7) can be expressed in terms of the parasitic currents of I_{Li}, I_{ox}^{a}, I_{ox}^{b} and I_p:

$$CE = 1 - 2[I_{ox}^{a} + I_{ox}^{b}]/I_A \tag{10.1}$$

$$\Delta_C = 2(Q_o\text{-}K)\,[I_{ox}^{a} - I_p + I_{ox}^{b}]/I_A \tag{10.2}$$

$$\Delta_D = 2(Q_o\text{-}K)\,[I_{ox}^{a} + I_{ox}^{b}]/I_A \tag{10.3}$$

$$Fade = 2(Q_o\text{-}K)\,[I_p]/I_A \tag{10.4}$$

Most interesting about these equations is that even though Li is lost to the SEI, via I_{Li}, this does not contribute to *capacity* loss for narrow range cycling where the negative

electrode potential does not vary with capacity. *Capacity* fade is observed only through positive electrode damage.

There may be situations where positive electrode material damage limits the amount of lithium that can be inserted into the positive electrode as opposed to trapping Li that cannot be removed (the latter case was treated above). Additionally, loss of electrical contact of the positive electrode material reduces the *capacity* of the positive electrode at both top of charge and bottom of discharge. These specific cases have not been explicitly treated above, but can be, using the formalism developed in Chapter 3 and Appendix A.

The parasitic currents in the cell are responsible for the cell voltage change and *capacity* loss during storage as outlined in Chapter 5. The potential drop during storage was shown to be given by:

$$V_{drop} = [q_{ox}^{a} + q_{ox}^{b}]\, dV/dQ \qquad [10.5]$$

where q_{ox}^{a} and q_{ox}^{b} are the parasitic *capacities* due to electrolyte oxidation and shuttle mechanisms during storage. dV/dQ is the slope of the V-Q relation at the storage potential. It was also shown in Chapter 5 that the cell discharge *capacities* immediately after storage, D_1, [See Figure 10.1B] and after charge after storage, D_2, are related to V_{drop} by,

$$D_2 - D_1 = V_{drop}\, dQ/dV \qquad [10.6]$$

where dQ/dV is the differential capacity of the Li-ion cell at the storage potential.

It is possible to relate quantities measured by the High Precision Charger to those measured by storage. For example, in cases where positive electrode damage is small, and there is no *capacity* loss, one finds at any given time, t, from the beginning of testing:

$$V_{drop}(t) = dV/dQ \int \Delta_C/\tau \, dt \qquad [10.7]$$

where the integral runs from 0 to the time t and τ is the time of one narrow range cycle. In a hypothetical case where V_{drop} varied linearly in time and Δ_C was the same for every cycle, then

$$V_{drop} \, dQ/dV \approx \Delta_C \, [\text{Time of Storage}]/[\tau]. \qquad [10.8]$$

In this experiment, the validity of equations [10.7] and [10.8] are explored.

10.3 Results

Figure 10.3 shows the voltage versus *capacity* of four NMC/graphite and four $LiCoO_2$/graphite cells cycling between 4.0 V and 4.1 V and at temperatures of 30, 40, 50 or 60°C. For clarity, only the 1st, 5th, 10th and 15th cycles are shown. The capacity axis tracks the accumulated capacity of the cells, assuming that the capacity of the cell after the very first discharge was 0.00 mAh. The charge and discharge endpoints continually slip to higher relative capacities as the cells were cycled, because of the parasitic reactions inside the cell [33,34]. Figure 10.3 also shows that as the temperature increased the slippage of the charge and discharge endpoints also increased, suggesting an increase in the parasitic reaction rates inside the cell.

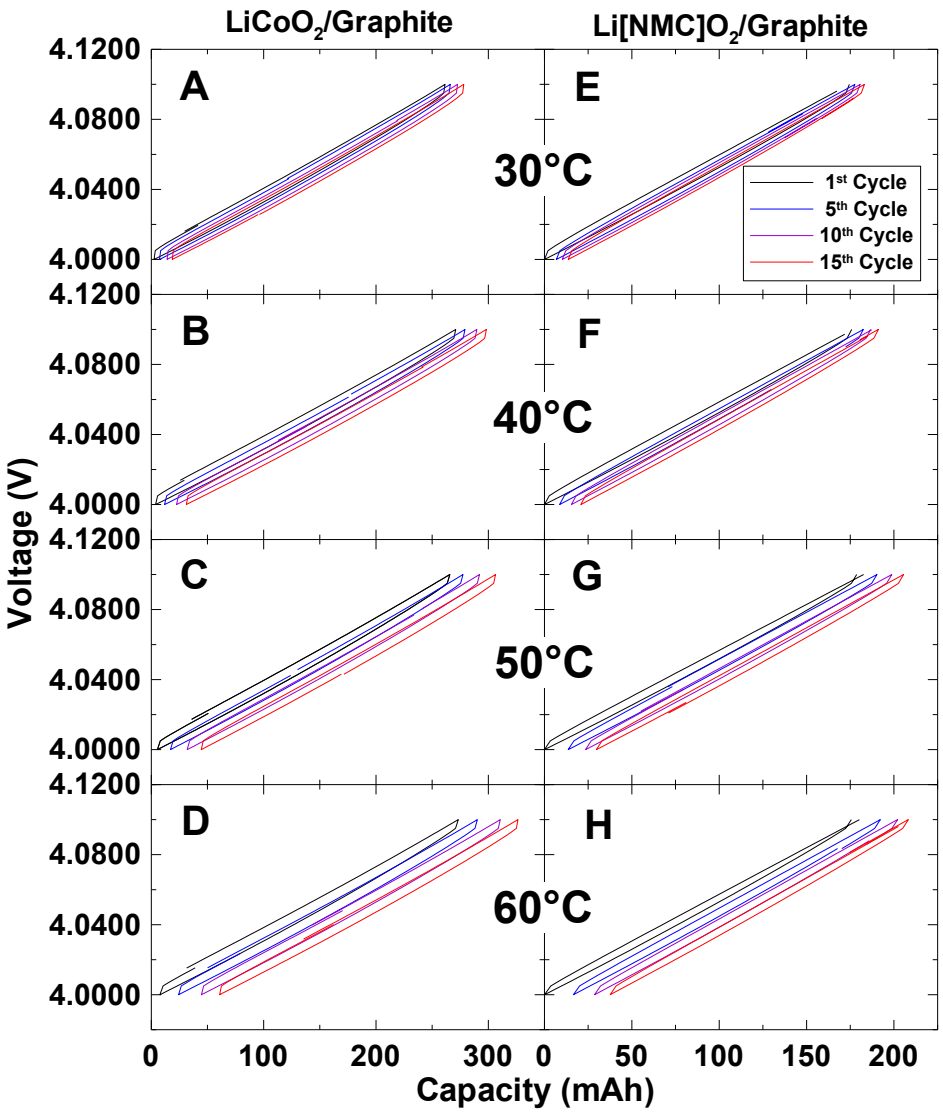

Figure 10.3 Voltage versus capacity of the $LiCoO_2$/graphite (left column) and $Li[Ni_{1/3}Mn_{1/3}Co_{1/3}]O_2$/graphite (right column) cells cycling between 4.0 V and 4.1 V and charged and discharged with a current of 15.0 mA.

Figure 10.4 shows the charge slippage plotted versus time for all the cells in this study. The charge slippage has been plotted as % of the full cell *capacity* so that data for the NMC/graphite and $LiCoO_2$/graphite cells can be directly compared. Figure 10.4 shows the dramatic increase of the charge slippage rate with upper cutoff potential and with temperature.

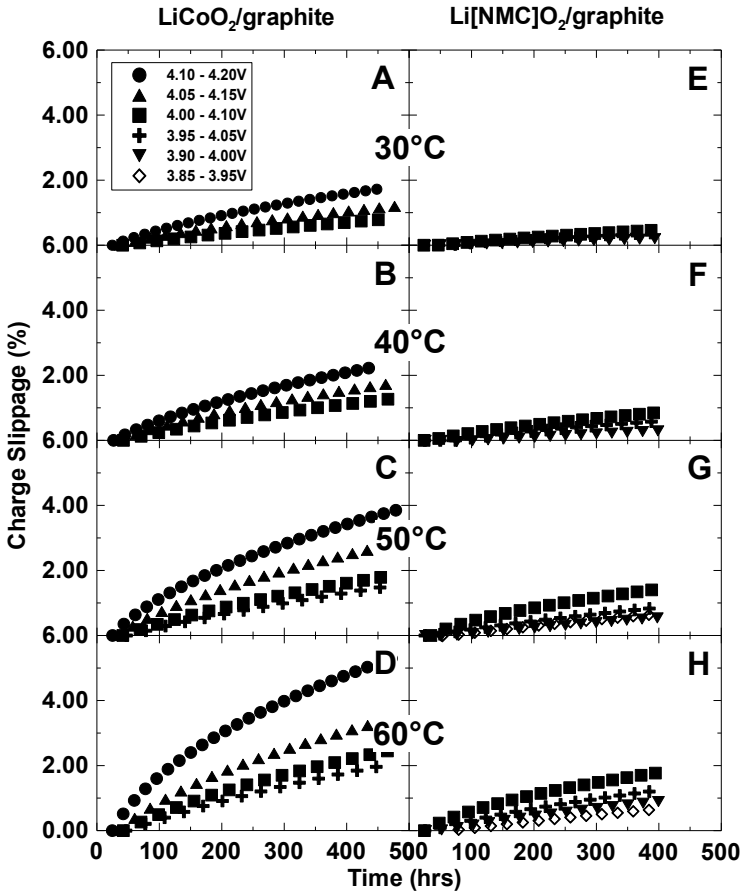

Figure 10.4 Charge slippage versus time of the $LiCoO_2$/graphite (left column) and $Li[Ni_{1/3}Mn_{1/3}Co_{1/3}]O_2$/graphite (right column) cells cycled between the voltage limits and at the temperatures indicated.

Figure 10.5 shows the normalized *capacity* plotted versus cycle number for commercial NMC/graphite and $LiCoO_2$/graphite cells cycling in the narrow ranges outlined in Table 1 at 30, 40, 50 and 60°C. The NMC/graphite cells show *capacity* loss with cycling in all cases and the $LiCoO_2$/graphite cells show either constant *capacity* or a **surprising** *capacity* increase with cycling. The data for the NMC cells prove that positive electrode damage (origin unknown) is occurring in the NMC/graphite cells, as positive electrode damage is the only mechanism that can cause *capacity* loss in narrow range cycling such as this (see Equation 10.4). The *capacity* increase of the $LiCoO_2$/graphite cells cycling at the highest potentials and the highest temperatures can

be explained by a consideration of Figure 10.2. The negative to positive electrode *capacity* ratio in these cells is very close to 1.00. Thus, the graphite electrode is almost completely filled and its potential drops somewhat when the cells are charged to a terminal voltage of 4.2 V in the early cycles as demonstrated in Figure 10.2. As cycling proceeds, the slippage rate of the negative electrode exceeds that of the positive electrode so the negative electrode moves to higher potential versus Li at the end of charge. In order to reach a terminal voltage of 4.2 V, the positive electrode is charged to successively higher potentials versus Li, hence causing a *capacity* increase in this narrow range cycling.

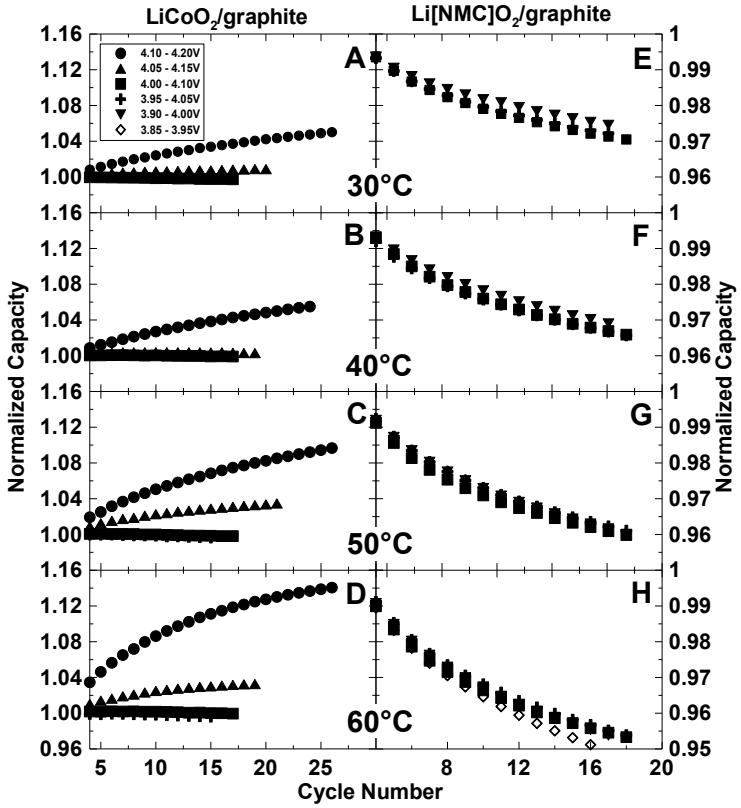

Figure 10.5 Normalized *capacity* versus cycle number of the $LiCoO_2$/graphite (left column) and $Li[Ni_{1/3}Mn_{1/3}Co_{1/3}]O_2$/graphite (right column) cells being cycled between the voltage limits and at the temperatures indicated.

Figure 10.5 shows that even in the most dramatic case, for $LiCoO_2$/graphite cells cycled between 4.1 and 4.2 V at 60°C, the *capacity* gain is 14% over 500 hours of testing

or 26 cycles. The initial *capacity* was about 180 mAh over this range, so this gain corresponds to about 25 mAh out of a total cell *capacity* of 2400 mAh. Figure 10.6 shows the cumulative charge endpoint slippage in mAh versus time for the $LiCoO_2$/graphite cell cycled between 4.1 and 4.2 V at 60°C. During the time that the *capacity* increased by 25 mAh, the charge endpoint slipped by about 160 mAh. The charge slippage far exceeds the *capacity* gain so we will ignore this *capacity* gain in our consideration of the validity of equations 10.7 and 10.8.

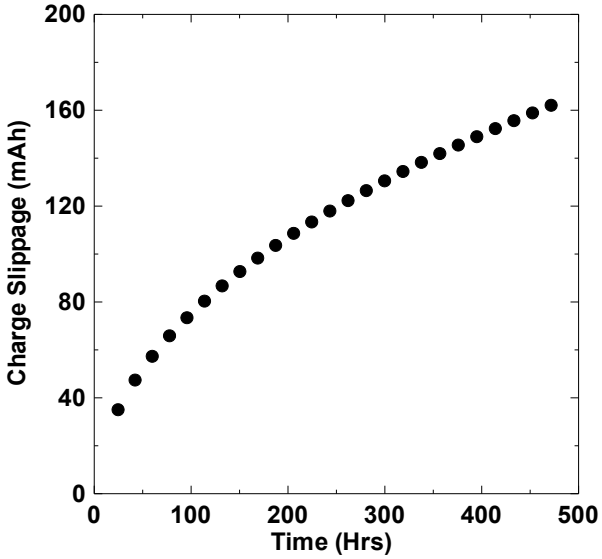

Figure 10.6 Cumulative charge endpoint slippage versus time for the $LiCoO_2$/graphite cell cycled between 4.1 and 4.2 V and at a temperature of 60°C

Figure 10.7A shows the slippage of the charge endpoints per hour (in mAh/h) and Figure 10.7B shows the fractional charge slippage (based on the full cell *capacity*) per hour both plotted versus the upper voltage limit of the narrow cycling range for each type of cell. The charge endpoint slippage rates were measured at 400 hours of testing for all the cells. As in Figure 10.4, as the temperature or upper cut off voltage of the cells increased, the slippage of the charge endpoints also increased. This suggested that electrolyte oxidation and/or transition metal dissolution inside the cells was being

amplified at higher voltages and temperatures. Figure 10.7B shows the fractional slippage of the NMC/graphite charge endpoints per hour to be lower than the $LiCoO_2$/graphite cells at the same upper voltage limit and temperature, suggesting that NMC has a reduced rate of parasitic reactions. Figure 10.7 demonstrates the usefulness of narrow range cycling. Researchers performing similar tests could assess the ideal upper voltage limits for different cell chemistries, balancing the need to reduce electrolyte oxidation in the cell and acquiring additional *capacity*. It may be worth noting that the slippage rate in mAh/h has the unit of mA and is a therefore a direct measure of the average parasitic current due to electrolyte oxidation and shuttle mechanisms. The largest parasitic current in Figure 10.7 corresponds roughly to a C/10000 rate.

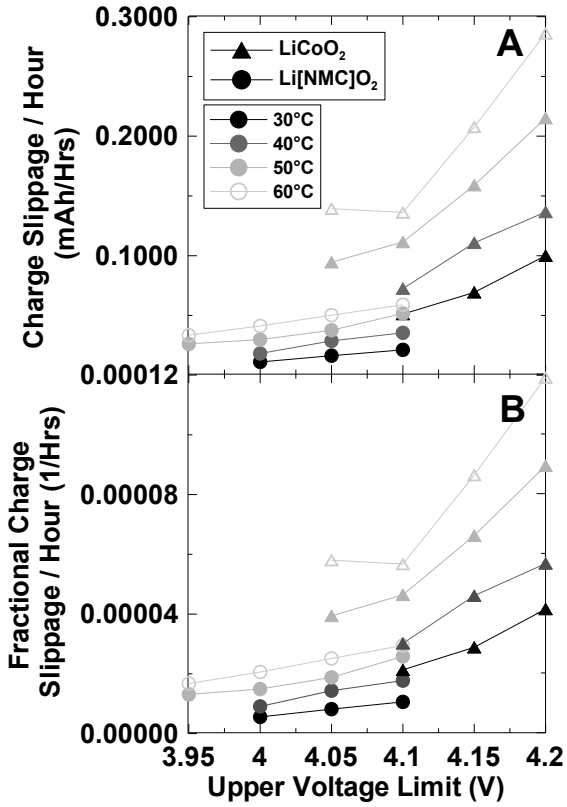

Figure 10.7 Top panel) Slippage of the charge endpoints per hour and (Bottom panel) fractional charge slippage per hour both plotted versus the upper voltage limit of the narrow cycling range of each cell. The fractional charge slippage is based on the 100% *capacity* of the cells, 2400 mAh for $LiCoO_2$/graphite cells and 2000 mAh for the NMC/graphite cells.

Figure 10.8 shows the coulombic inefficiency divided by the time of one charge-discharge cycle plotted versus time for the commercial $LiCoO_2$/graphite and NMC/graphite cells. The CIEs of all of the cells decreased with increased cycling number and time, but never reached 0.0000. This suggests that the parasitic reactions at the positive electrode slow down with time, but do not stop completely. The CIEs were

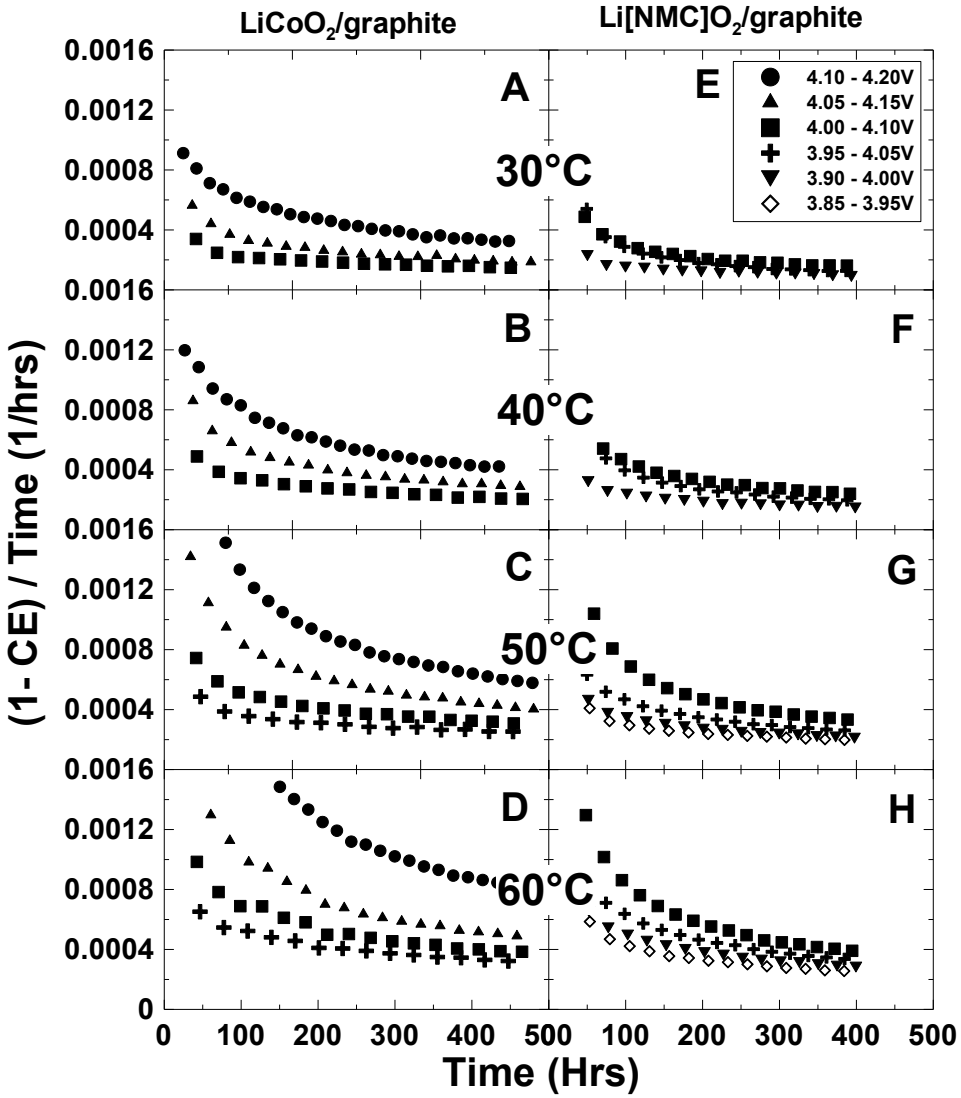

Figure 10.8 Coulombic inefficiency (1-CE) divided by the time of one charge-discharge cycle versus time for the $LiCoO_2$/graphite (left column) and $Li[Ni_{1/3}Mn_{1/3}Co_{1/3}]O_2$/graphite (right column) cells.

strongly affected by temperature and voltage, so that as the temperature or voltage limits were increased the CIE, departed further from 0.0000. This suggests, as do Figures 10.4, 10.5 and 10.6, that electrolyte oxidation and/or transition metal dissolution rates increase at higher temperatures and voltages.

Figure 10.9 shows the cell voltage plotted versus both Q and dQ/dV for a single cycle of the commercial NMC/graphite and $LiCoO_2$/graphite cells charged and discharged with 100 mA at 40°C. dQ/dV versus voltage during charge (red) and discharge (black) cycles are shown. Table 10.2 lists the average value of dQ/dV, called dQ/dV_{avg} at each of the upper cutoff voltages used in these experiments for both cell chemistries. These values of dQ/dV_{avg} are needed to compare HPC results to storage results.

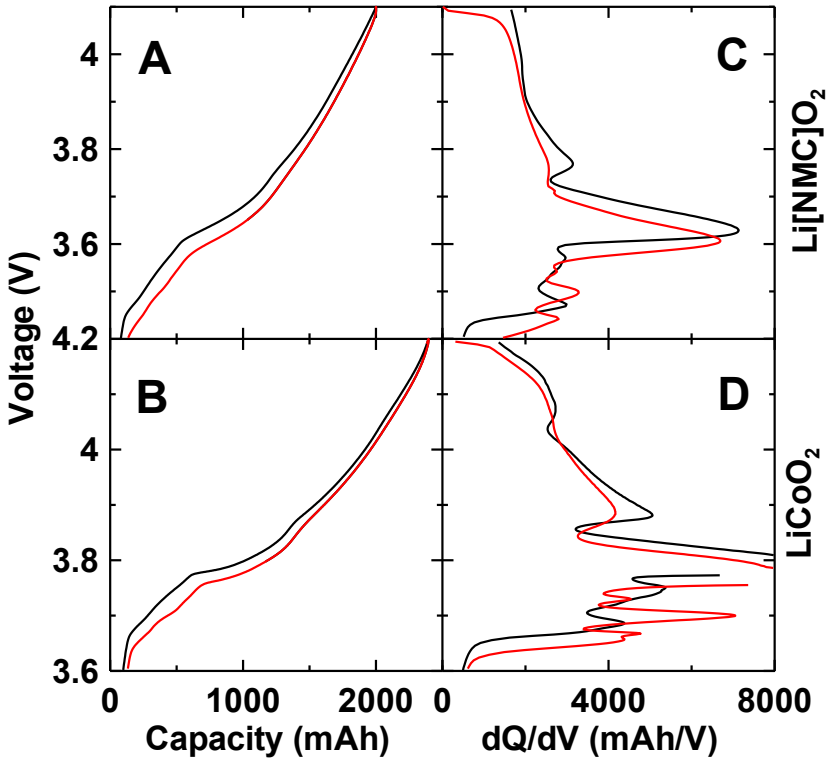

Figure 10.9 Voltage versus capacity (left column) and differential capacity (dQ/dV) (right column) for a single cycle of the commercial $LiCoO_2$/graphite and $Li[Ni_{1/3}Mn_{1/3}Co_{1/3}]O_2$/graphite cells at 30°C.

Table 10.2 Lists the average value of dQ/dV at each of the upper cut off voltages for the $Li[Ni_{1/3}Mn_{1/3}Co_{1/3}]O_2$ and $LiCoO_2$/graphite cells used in this experiment.

	Temperature			
Upper Voltage Limits	**30°C**	**40°C**	**50°C**	**60°C**
$LiCoO_2$/graphite	**dQ/dV_{avg} (mAh/V)**			
4.20	1850	1860	1850	1830
4.15	1980	1990	1970	1960
4.10	2470	2490	2500	2510
4.05	2680	2690	2690	2700
$Li[Ni_{1/3}Mn_{1/3}Co_{1/3}]O_2$/graphite				
4.10	1550	1550	1570	1520
4.05	1690	1690	1690	1700
4.00	1800	1800	1800	1810
3.95	1900	1890	1870	1880

Figure 10.10 shows storage results for both $LiCoO_2$/graphite and NMC/graphite cells. In Figure 10.10, the decay of cell voltage with time during storage has been plotted as 1.00 V – "voltage drop" versus time for easy comparison of the different chemistries at the different voltages and temperatures. The reader is cautioned that the $LiCoO_2$/graphite cells show storage results at 4.2 V and 4.15V while the NMC/graphite cells do not. Chapter 5 showed that processes which change the Li content of the positive electrode in a fully charged cell are responsible for changes in the open circuit voltage of the cell as is captured in Equation 10.5. Figure 10.10 shows that the rate of voltage drop decreases with time, suggesting that the parasitic reactions at the positive electrode slow down with time. Figure 10.10 also shows that the rate of voltage drop decreases as the initial storage voltage decreases. These two observations are consistent with observations made regarding charge endpoint slippage (Figures 10.4 and 10.7) and coulombic inefficiency (Figure 10.8) (both decrease as V decreases and as T decreases).

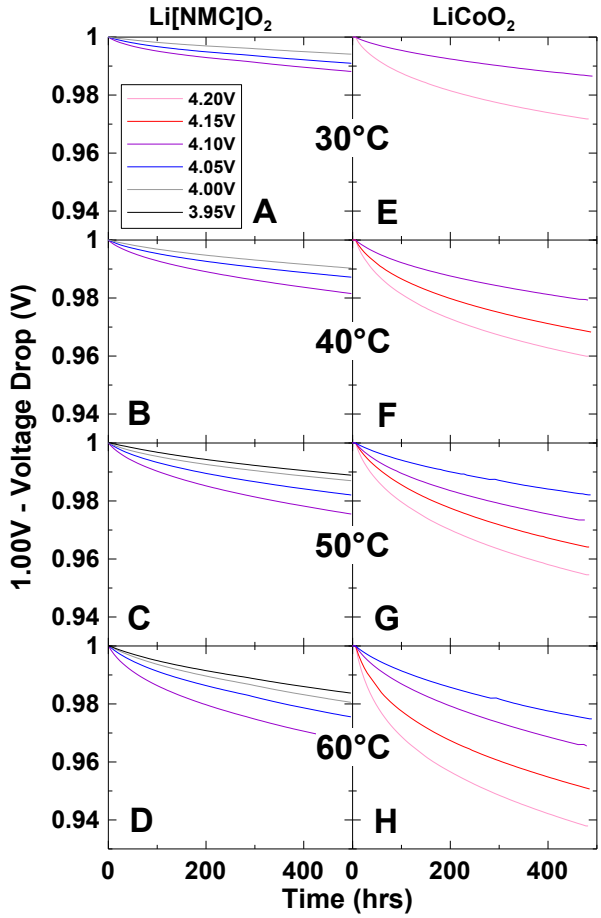

Figure 10.10 [1.00 – voltage drop] versus time of the $LiCoO_2$/graphite (right column) and $Li[Ni_{1/3}Mn_{1/3}Co_{1/3}]O_2$/graphite (left column) cells during open circuit storage at the voltages and temperatures indicated.

Figures 10.11A and 10.11C show the total voltage drop, V_{drop}, plotted versus storage temperature and starting voltage for the same cells described by Figure 10.10. As the temperature and starting voltage of the cells increased, the voltage drop of the cells also increased. Thus, storage experiments confirm the narrow range cycling results above, that electrolyte oxidation and/or shuttle mechanisms are amplified at higher voltages and temperatures. Figures 10.11B and 10.11D show the product of V_{drop} and dQ/dV_{avg} (taken from Table 10.2 for the appropriate voltage) plotted versus storage temperature and starting voltage. The quantity, V_{drop} dQ/dV_{avg} represents the charge corresponding to the amount of lithium atoms inserted into the positive electrode during

the storage period. V_{drop} dQ/dV_{avg} has been calculated as a fraction of total cell *capacity* so that comparisons between the two chemistries can be made. Figures 10.11B and 10.11D show that the NMC positive electrode has a smaller self-discharge rate than the $LiCoO_2$ electrodes under all conditions, at least for the cells studied here. Obviously, electrolyte additives (unknown) and positive electrode specific surface area (also unknown) would affect this comparison in similar cells made by other suppliers.

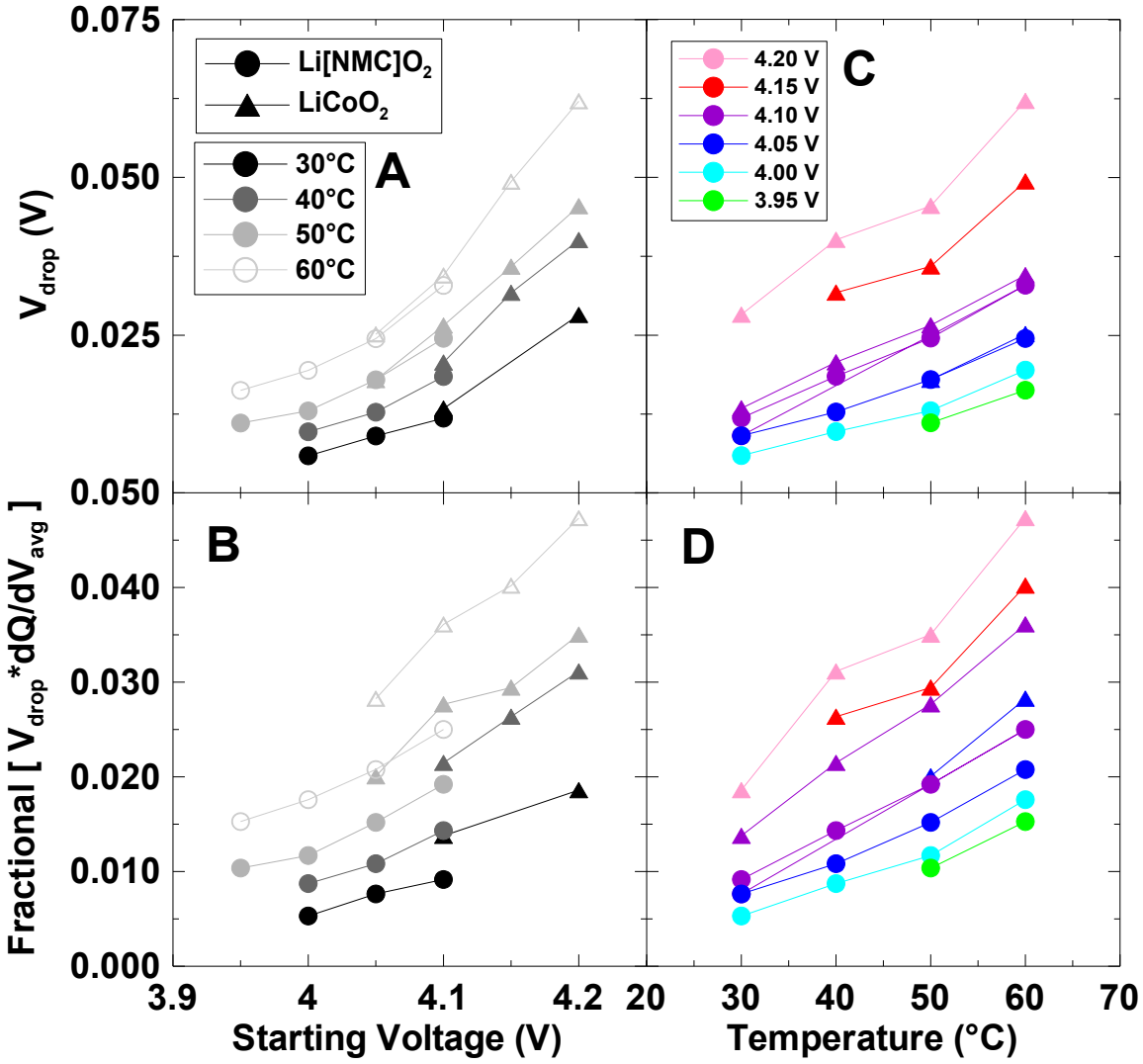

Figure 10.11 Voltage drop (top row) and fractional [voltage drop * dQ/dV] (bottom row) versus starting voltage (left column) and storage temperature (right column) for the same $Li[Ni_{1/3}Mn_{1/3}Co_{1/3}]O_2$ and $LiCoO_2$/graphite cells in Figure 10.10.

Figure 10.12 compares the time dependence of V_{drop} and charge endpoint *capacity* slippage for $LiCoO_2$/graphite cells at 40°C. The cells were stored at 4.2, 4.15 and 4.1 V. Nominally identical cells were cycled between 4.1 and 4.2 V, between 4.05 and 4.15 V and between 4.0 and 4.10 V. V_{drop} versus time for the cell stored at 4.15 V should be compared to the charge endpoint slippage for the cell cycled between 4.1 and 4.2 V. The two curves are similar. V_{drop} versus time for the cell stored at 4.10 V should be compared to the charge endpoint slippage for the cell cycled between 4.05 and 4.15 V. The two curves are similar. The agreement between the storage and precision cycling results is a consequence of equation (10.7) which predicts that these behaviours should be identical in the case where there is no positive electrode damage. At long times the storage and narrow range cycling data begin to deviate from each other. This is caused by the drop in voltage of the storage cell. At small times the average voltage of the cycling and storage cells are very similar and thus I_{ox}^{a} and I_{ox}^{b} will be very similar too. This is why there is an excellent agreement between the V_{drop} and the product of the charge endpoint slippage and dQ/dV(V) of the cells early on. However, as the voltage of the storage cell decreases, I_{ox}^{a} and I_{ox}^{b} decrease as well, causing the rate at which the voltage of the storage cell decreases to slow down too. Similar agreement between V_{drop} and charge endpoint slippage was observed for all the $LiCoO_2$ cells. This suggests that high precision storage experiments give basically the same information as high precision narrow-range cycling experiments. Given that the former are much easier to carry out, this suggests that investments in high precision storage equipment are justified.

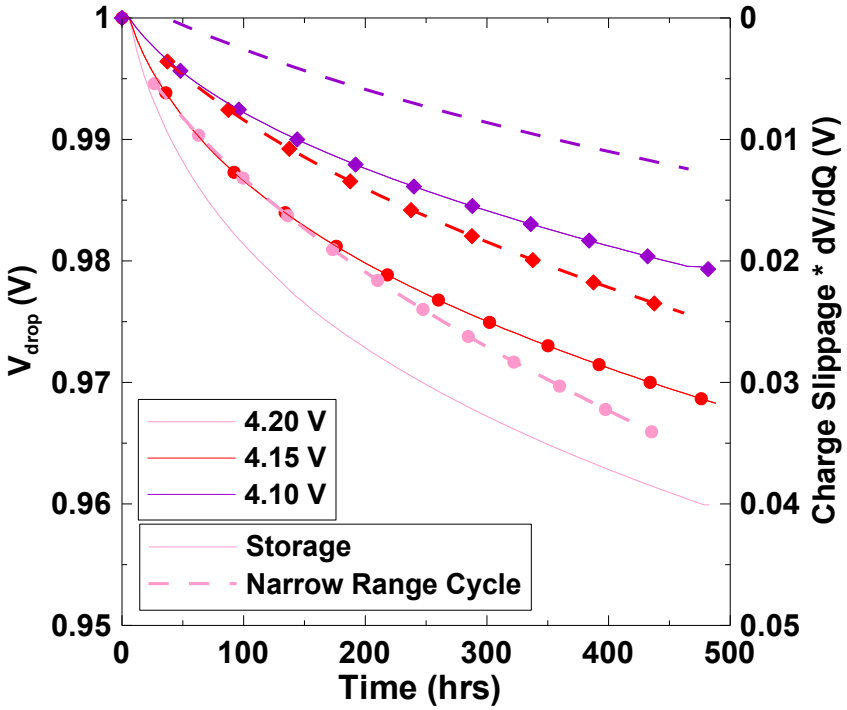

Figure 10.12 Voltage drop versus time (solid curves) of the $LiCoO_2$/graphite cells in open-circuit storage at 40°C and the product of the charge endpoint *capacity* slippage and dV/dQ versus time (dashed curves) of the $LiCoO_2$/graphite cells cycling between narrow voltage limits at the same temperature. Curves having the same markers should be compared as is explained in the text.

Figure 10.13A shows the fractional charge endpoint slippage per hour of the cells in Figure 10.6 plotted versus V_{drop} dQ/dV_{avg} in fractional *capacity* (based on the total cell *capacity*). Based on Equation 10.8, these quantities should be linearly related, and Figure 10.13 shows a good correlation. Figure 10.13B shows the fractional charge slippage per hour of the cells in Figure 10.6 plotted versus the fractional reversible *capacity* loss, $D_2 - D_1$, of the cells in Figure 10.11 during storage. Again, according to the equations developed above, a good correlation is expected and is observed. The charge slippage

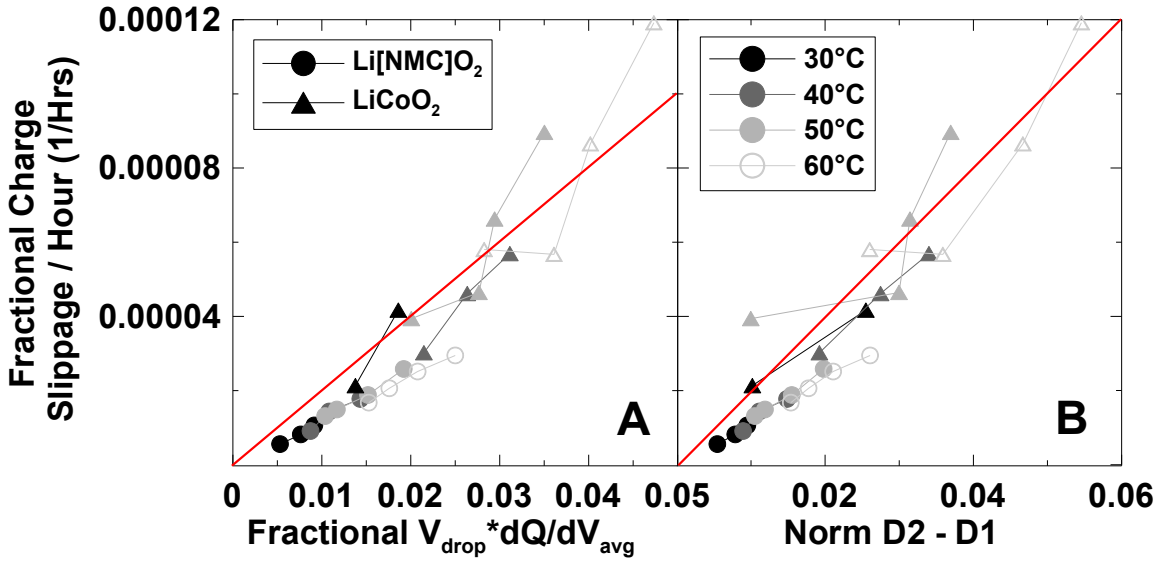

Figure 10.13 Fractional charge slippage per hour of the cells in Figure 10.4 plotted versus the fractional [voltage drop * dQ/dV] (left column) and fractional $D_2 - D_1$ (right column) of the cells in Figure 10.11. According to Equation 10.8, these quantities should be linearly related. Lines have been added to help guide the eyes.

was measured after 400 hours of testing for all the cells. If electrolyte oxidation at the positive electrode is responsible for the voltage drop of the cells, then, based on Equations 10.6 and 10.8 one expects both $V_{drop}\ dQ/dV_{avg}$ and $D_1 - D_2$ to be proportional to the charge endpoint slippage per hour, as is observed.

One outcome of this work is the strong dependence of these parasitic reactions on upper cutoff potential and temperature, at least on the surfaces of these particular electrode materials. Such results give the author serious doubts that successful electrolytes can be developed for high potential positive electrode materials like $LiNi_{0.5}Mn_{1.5}O_4$ which operates near 4.7 V and always shows high charge endpoint *capacity* slippage. By contrast, the Dahn lab (to be published) has shown that alternative high potential materials involving oxygen loss during the first charge, like $Li[Li_{0.2}Ni_{0.2}Mn_{0.6}]O_2$, show charge endpoint *capacity* slippage at 4.6 V which is similar to

that of NMC at 4.1 or 4.2 V. There is something very special about the surfaces of the oxygen loss materials that apparently limits electrolyte oxidation.

This experiment shows that high precision charger and storage tests should be used in concert to study the parasitic currents that occur in the Li-ion cell.

Chapter 11 Synergies in Blended LMO and NMC Positive Electrodes.

Spinel type $LiMn_2O_4$ (LMO) and its derivatives are currently one of the most promising positve electrode materials for large-format Li-ion batteries. This is because of three dimensional Li^+ diffusion, low cost, low toxicity and the abundant raw materials. However, LMO is plagued with some serious issues, such as poor cycling at elevated temperatures (>50°C). Much has been published by different research groups on this subject and different solutions have been proposed with varying levels of success [67–69,127–130]. However, the recommended solutions normally produce lower *capacity* materials or require a more expensive electrolyte.

In 2001, Numata et al. recommended an interesting approach to improve the *capacity* retention of LMO based electrodes; to mix it with a different positive electrode material [131]. They found that by simply mixing LMO and $LiNi_{0.8}Co_{0.2}O_2$ together, HF generation, Li loss and Mn dissolution were significantly reduced for cells stored at elevated temperatures. Since only a small amount of this higher specific *capacity* material needed to be added to obtain the desired effect, the process was easy and inexpensive. After that publication there have been numerous other publications on the subject of physical mixtures of positive electrode materials. Some examples of mixed positive electrode materials are LMO - $LiNi_{0.8}Co_{0.2}O_2$ [132], $Li_{1.1}Mn_{1.9}O_4$ - $LiNi_{0.8}Co_{0.15}Al_{0.05}O_2$ [133], $Li_{1.1}Mn_{1.9}O_4$ - NiO [134], $LiMn_{1.8}Li_{0.1}Ni_{0.1}O_{3.8}F_{0.2}$ - $LiCoO_2$ [135], LMO - $LiNi_{0.80}Co_{0.15}Al_{0.05}O_2$ [136], LMO - $Li[Li_{1/15}Ni_{1/5}Co_{2/5}Mn_{1/3}O_2]$ [137] and so on [138–143].

Here, the HPC was used to study the CE, normalized *capacity* loss and charge endpoint slippage of electrodes made by mixing $Li[Ni_{1/3}Mn_{1/3}Co_{1/3}]O_2$ (NMC) and LMO together. Electrodes with higher concentrations of NMC enjoyed higher than expected *capacity* retentions and improved CE. The majority of the *capacity* loss in these mixed electrodes originated from the spinel component and the spinel slowly transformed to a more Mn-poor phase. Consequently the lost Mn was found on the negative electrodes and a relationship between Mn dissolution and CE was observed.

11.1 Experiment

The active material of the mixed electrodes prepared by simply mixing commercially available LMO (T100 - Tronox) and NMC (BC618K - 3M) together. The ratios at which the LMO and NMC were mixed together were 100%:0%, 75%:25%, 50%:50%, 25%:75% and 0%:100%. The active material was then added to Super-S carbon black (MMM Carbon, Belgium) and PVDF binder at a weight to weight ratio of 86:7:7 respectively. The slurry was spread on an Al foil with a notch bar and then dried in air at 90°C overnight. The electrolyte used in all of the cells was 1 M $LiPF_6$ in an ethylene carbonate/diethyl carbonate [1:2 v/v, Novolyte Technologies] solution. The 2325 coin-type cells with two Celgard 2300 separators and a lithium foil common counter and reference electrode were assembled in an argon-filled glove box with the mixed electrodes described above. All cells were charged and discharged with a constant current between 3.0 and 4.3 V and at a rate of C/10. To observe possible behaviours and trends the five electrodes types were cycled at 30.0, 40.0, 50.0 and 60.0°C. All of the mixed electrodes were tested using the HPC.

To observe the effects of cycling on Mn dissolution and the solid state structure of LMO electrodes, LMO/Li cells were constructed in the same way described above. The cells used in the Mn dissolution tests were cycled on a 96 channel Maccor cycling unit (Maccor 2000 series) at a temperature of 55^{o}C. The cells were then cycled 5, 10, 20 or 50 times and then removed and dissembled quickly to perform the atomic absorption tests described in Chapter 7.3. The cells used in the solid state structure tests were cycled on the HPC at a temperature of 50^{o}C. The cells were cycled 2, 5 or 9 times, discharged to 3.0 V and allowed to come to equilibrium for several hours. The cells were then dissembled in a He-filled glove box where the electrode materials were recovered and placed into a special air sensitive holder discussed in Chapter 7.1. All XRD patterns were collected with a Siemens D5000 powder diffractometer.

11.2 Results

Figure 11.1 shows the differential capacity versus voltage of the 5 mixed electrodes cycling at 40^{o}C. The differential capacities of the electrodes are a superposition of the individual components. Figure 11.2 shows the specific discharge *capacities* for all the mixed electrodes versus cycle number. The specific *capacity* of the cells increased with increased NMC content and temperature. The cycling stability of the cells deteriorated with increased temperature and LMO content suggesting that the LMO component used in the mixed electrodes was not able to cycle well at temperatures above 50^{o}C.

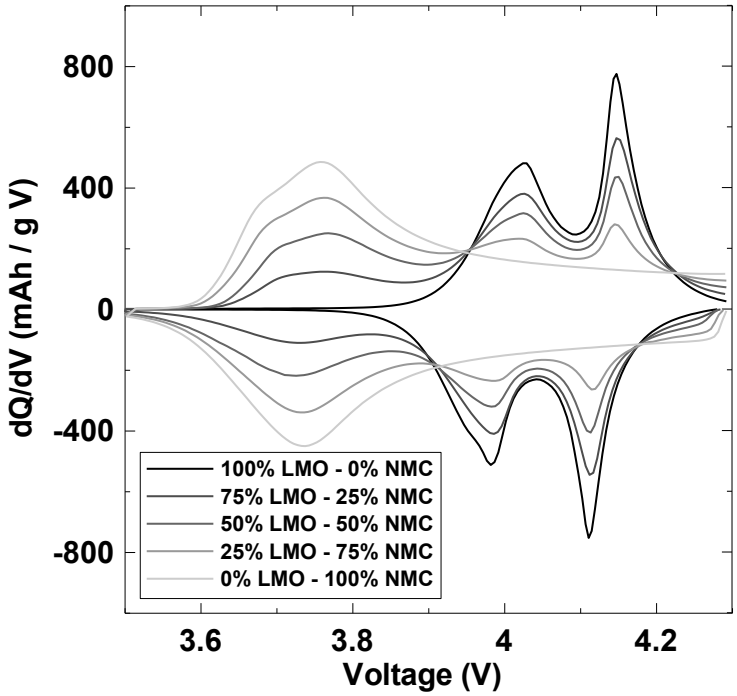

Figure 11.1 Differential capacity versus potential of the five mixed electrodes charged and discharged at C/10 and at a temperature of 40°C.

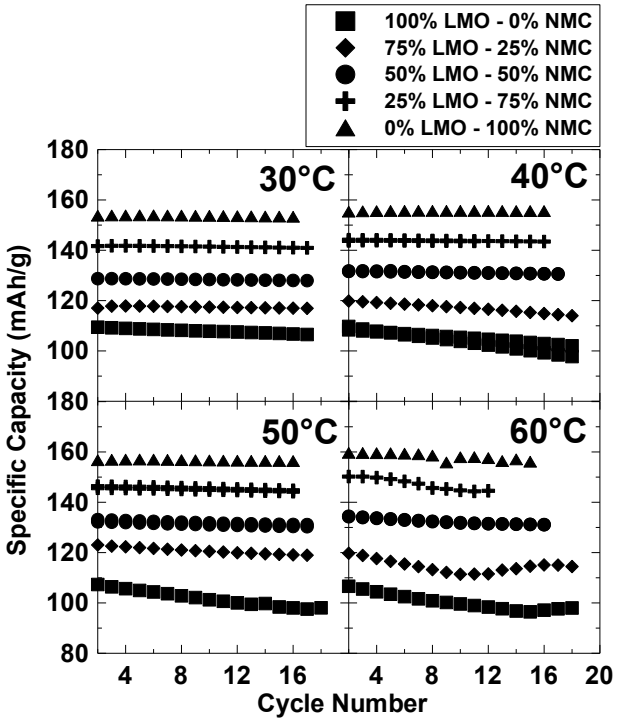

Figure 11.2 Discharge *capacities* for all the mixed electrode cells versus cycle number. The cells were charged and discharged at C/10 and at the temperatures indicated.

Figure 11.3 shows the normalized *capacities* versus cycle number for all of the cells described by Figure 11.2. The *capacity* retention of all the mixed electrodes decreased as the temperature increases. The *capacity* retention of all the cells increased with increased NMC content for all temperatures. In fact, all the cells containing both

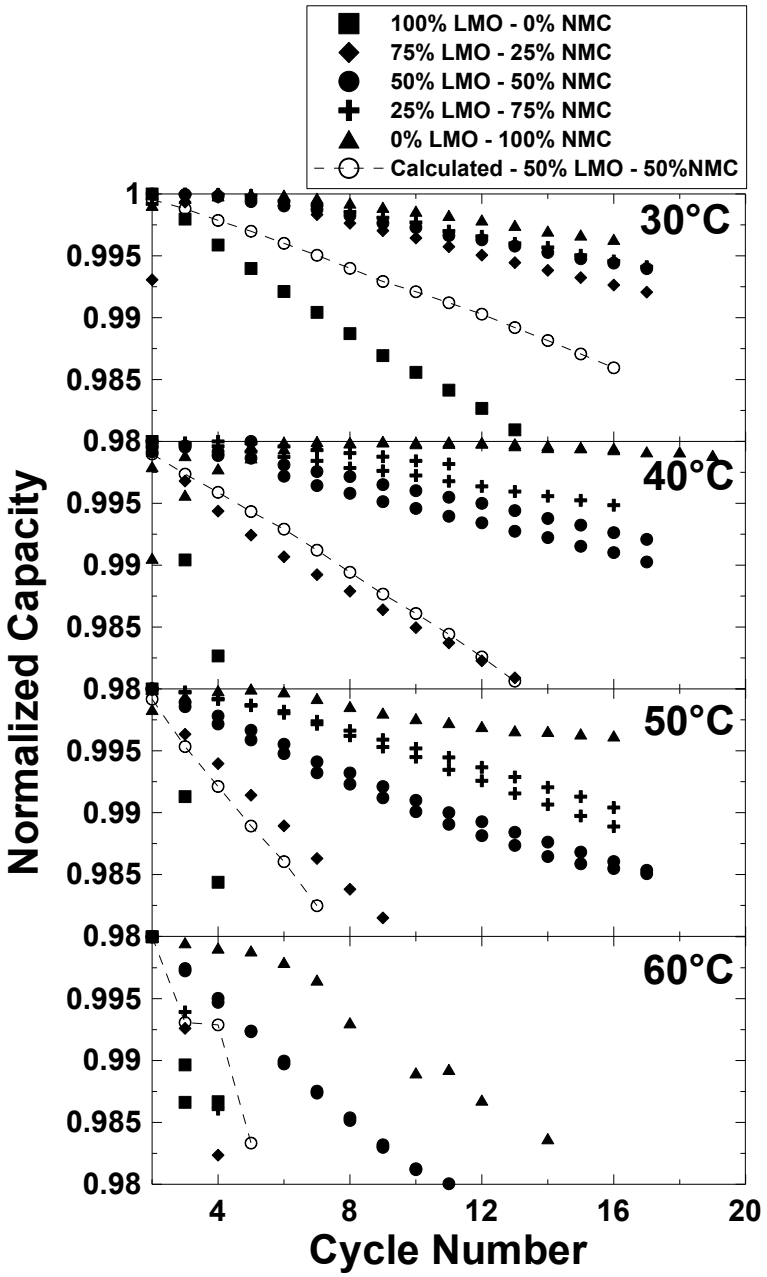

Figure 11.3 Normalized *capacities* for all the mixed electrode cells plotted vs. cycle number charged and discharged at C/10 and at the temperatures indicated.

NMC and LMO enjoy better *capacity* retention than would be expected assuming their individual cathode materials were working independently. To illustrate this observation, the expected values for the 50% LMO – 50% NMC electrodes were calculated using the mid point between the 100% LMO and 100% NMC electrodes for each temperature. The expected 50% LMO – 50% NMC electrodes have larger normalized *capacity* loss then the experimental 50% LMO – 50% NMC electrodes. For temperatures greater than 30°C, the normalized *capacity* loss for the expected 50% LMO – 50% NMC electrodes follow the measured 75% LMO – 25% NMC results fairly closely. This suggests that a relatively small amount of NMC needs to be added to LMO electrodes in order to improve *capacity* retention significantly.

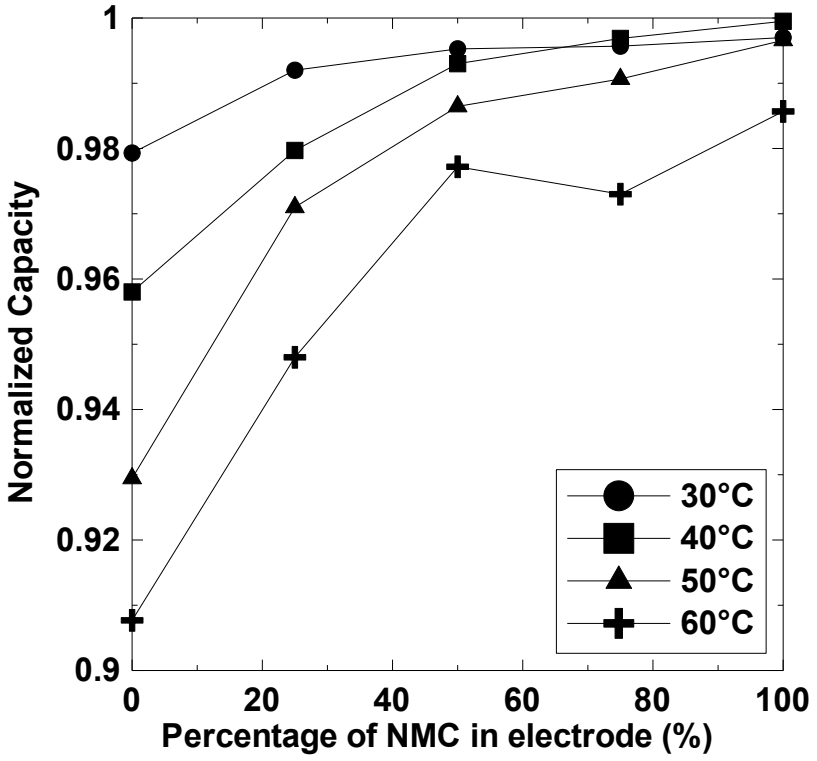

Figure 11.4 Fractional *capacity* remaining after 14 cycles plotted versus the percentage of NMC in the electrodes for the cells described by Figures 11.2 and 11.3.

Figure 11.4 shows the normalized *capacity* after 14 cycles versus percentage of NMC in the mixed electrodes described in Figure 11.3. The *capacity* retention dramatically improved when 25% or 50% NMC was added to the electrodes. Mixed electrodes with more than 50% NMC showed less dramatic improvements in *capacity* retention as the concentration of NMC increased.

Figure 11.5 shows a simplified schematic diagram of the coulombic imbalance caused by Mn dissolution in LMO/Li cells. During charge, 8 Li ions are extracted from the LMO electrode and 1 Mn ion is dissolved, causing 10 electrons to be passed around the external circuit to balance the charge. At the Li metal anode, all of the Li ions and the Mn ion are deposited. During discharge, the 8 Li ions can be re-inserted into the LMO

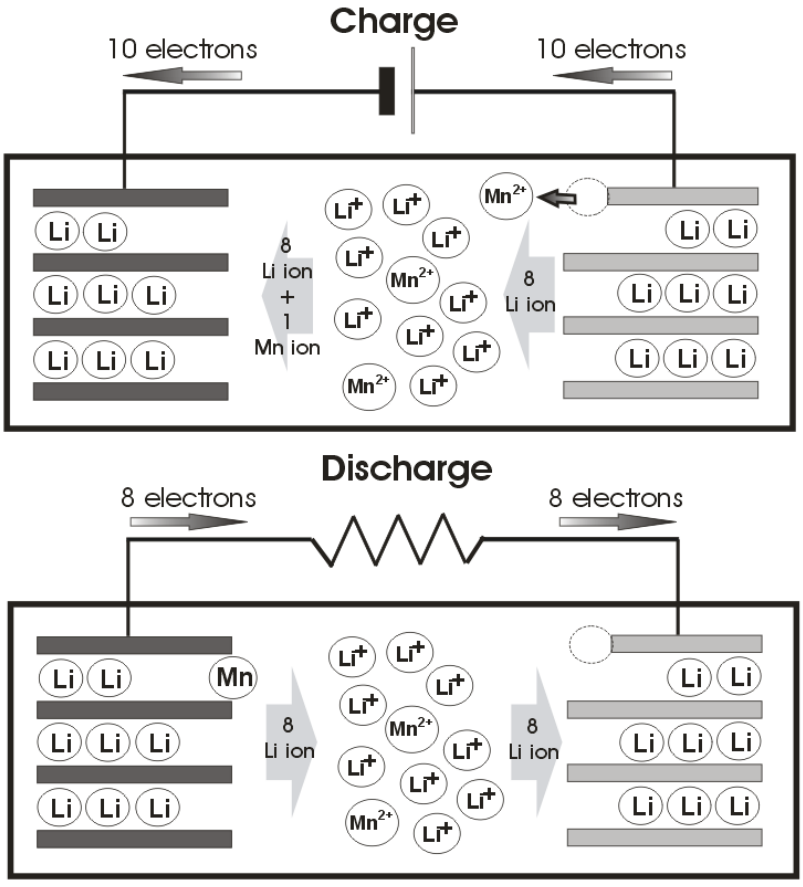

Figure 11.5 A schematic diagram of the coulombic imbalance caused by Mn dissolution in LMO/Li cells during one charge and discharge

structure but the charge corresponding to the transferred Mn cannot be recovered. Thus only 8 electrons are passed back through the external circuit during discharge. In Equation 3.15 this leads to a CE less then unity (1.0000) and indicates the presence of a parasitic process. A similar mechanism involving transition metal dissolution from NMC would affect the CE of the cell in a similar way.

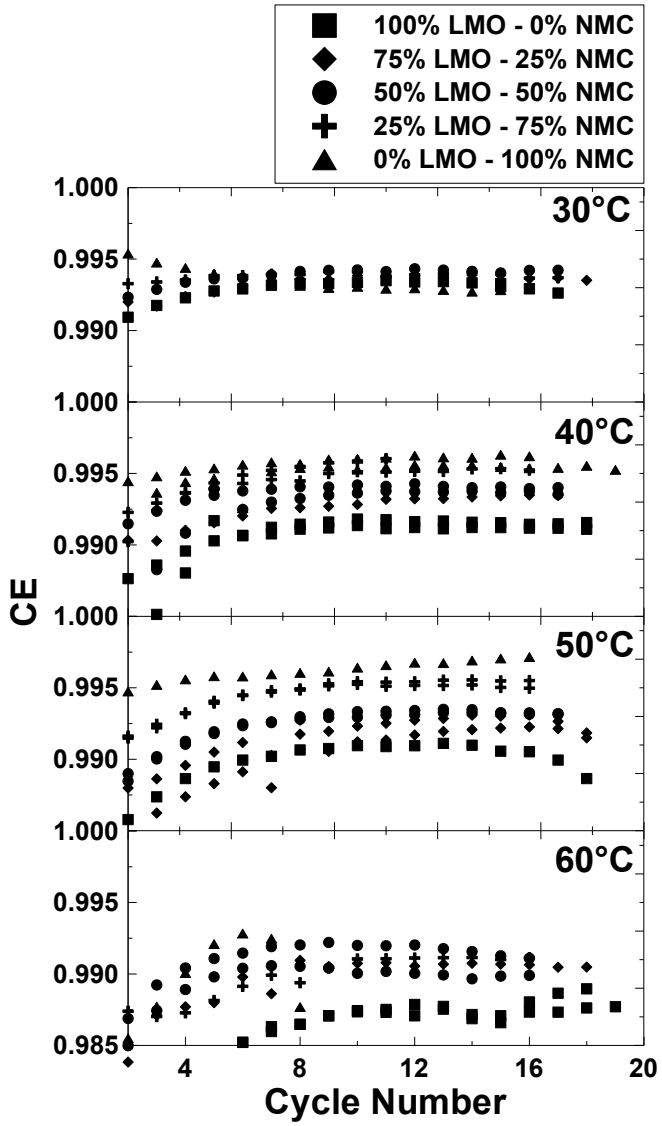

Figure 11.6 Coulombic efficiencies for all the mixed electrode cells plotted versus cycle number. The cells were charged and discharged at C/10 and at the temperatures indicated.

Figure 11.6 shows the CE versus cycle number for the same cells described by Figures 11.2, 11.3 and 11.4. The CE of the cells at 40, 50 and 60°C was strongly dependent on NMC content, such that as the amount of NMC in the electrodes increased, the CE increased towards unity. This suggests that the coulombic imbalance caused by Mn dissolution was worse in LMO rich electrodes than it was in NMC rich electrodes.

Figure 11.7 shows the CE versus Mn content found in the Li metal negative electrodes after cycling for the same cells described by Figure 11.6. The CE of the cells decreased as the Mn content in the negative electrodes increased. Pure NMC electrodes show a stronger decrease in CE with Mn content (triangles in Figure 11.7) compared to LMO electrodes (squares in Figure 11.7). This may be because Co and Ni dissolution also contributes to the imperfect CE of the NMC electrodes.

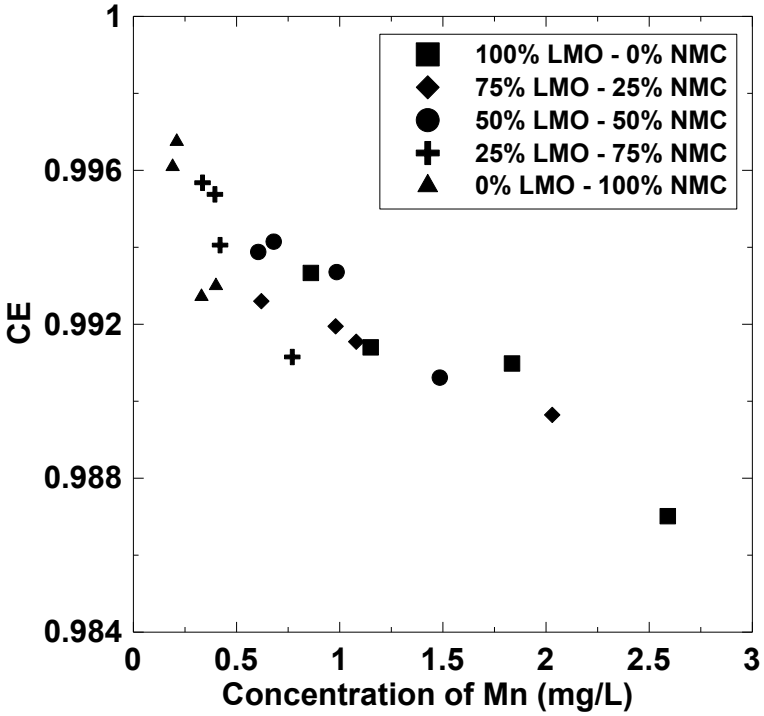

Figure 11.7 Coulombic efficiencies versus Mn content found in the Li negative electrode of the mixed electrode cells.

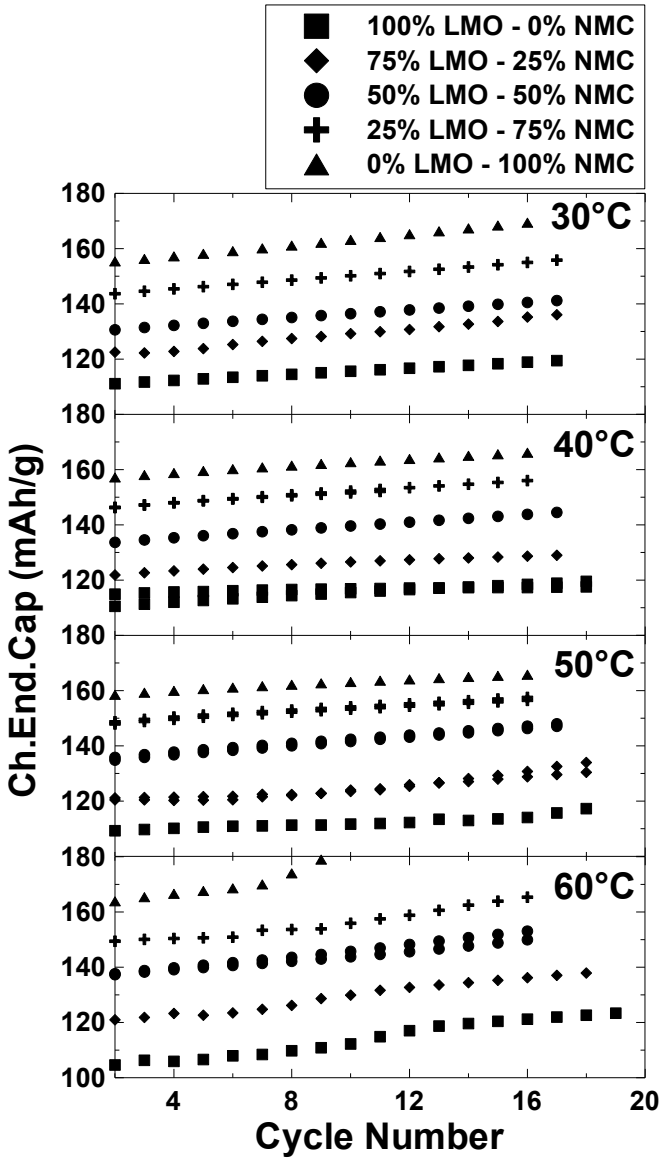

Figure 11.8 Absolute charge endpoint *capacity* plotted versus cycle number for the Li/LMO:NMC cells. All the cells show significant charge endpoint slippage at all temperatures.

Figure 11.8 shows the charge endpoint *capacity* versus cycle number for the same cells described in Figure 11.2. The charge endpoints move, or slip, to higher relative *capacities* with cycling and this slippage is quite severe for all cells. In Chapter 3 it was shown that the slippage of the charge endpoint was governed by electrolyte oxidation,

positive electrode *capacity* loss, shuttle mechanisms, metal ion dissolution or some combination of these occurring in the cell. Figure 11.7 suggests that Mn dissolution was an important contributor to the coulombic inefficiency of the mixed electrodes, so it seemed likely that it also played an important role in the charge endpoint slippage.

Figure 11.9 shows the charge slippage that occurs during the time of one charge – discharge cycle for the cells described by Figure 11.8 plotted versus the Mn content found in the Li metal negative electrode after cycling. Electrodes with the same ratio of NMC and LMO show a roughly linear increase in measured charge endpoint slippage as a function of Mn content (trend lines added to help guide the eyes). This suggests, as in Figure 11.7, that Mn dissolution was an important contributor to the charge endpoint slippage of the mixed electrodes. Figure 11.9 also shows that as the concentration of LMO in the mixed electrodes increases, the slopes of the charge endpoint slippage versus Mn content graphs decrease.

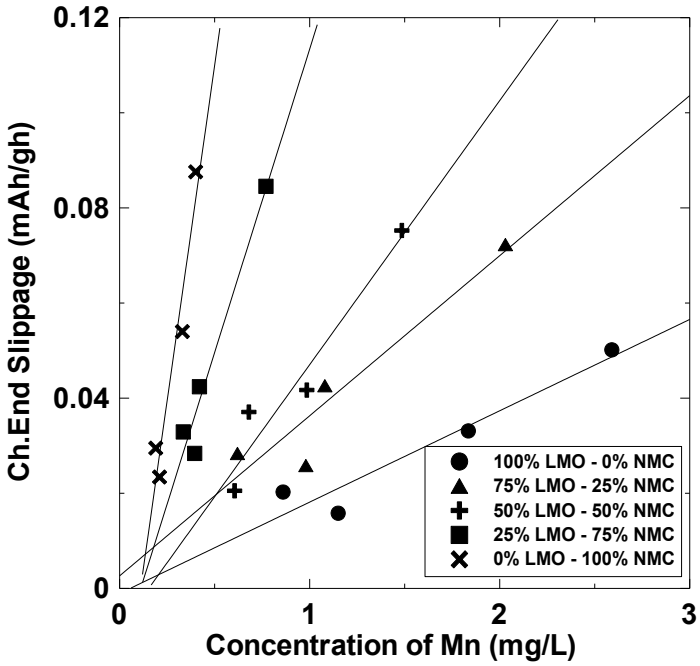

Figure 11.9 Absolute charge endpoint *capacity* slippage per unit time plotted versus the content of Mn found at the Li negative electrode for the cells described by Figures 11.7 and 11.8.

Figure 11.10 shows the Mn content lost from the positive electrode per unit of charge endpoint slippage (i.e. the inverse of the slopes in Figure 11.9) plotted versus the percentage of LMO in the electrodes. As the concentration of LMO in the electrodes increased, the amount of Mn lost per unit of charge endpoint slippage also increased, but the increase was not linear. The dotted line in Figure 11.10 shows a linear trend line. This suggests that adding NMC to the electrodes causes a synergistic effect which reduces the amount of Mn dissolution over that simply expected from a physical mixture. It is worth noting that the maximum charge endpoint slippage in Figure 11.9 is **not** reduced by NMC addition, so in the presence of NMC other processes, such as consumption of protons [135], may be occurring that lead to high charge endpoint slippage.

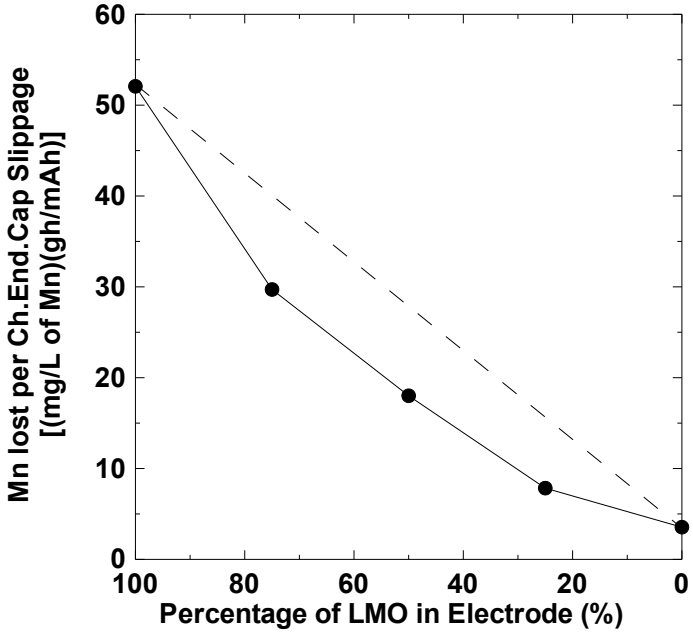

Figure 11.10 Inverse slopes of the fitted lines in Figure 11.9 plotted versus percentage LMO in the electrodes. This shows that the amount of Mn produced per unit of charge endpoint slippage is reduced in the mixed electrodes compared to that expected (dashed line) for a physical mixture.

Figure 11.11 shows the fractional *capacity* loss plotted versus Mn content found on the Li negative electrode after cycling for LMO/Li (no NMC) half cells cycled 5, 10, 20 and 50 times at 55°C. The fractional *capacity* loss increased with the Mn content found on the negative electrode. This suggests that Mn dissolution is also an important contributor to the *capacity* fade of the LMO electrodes in agreement with the findings of other authors [68,69,129].

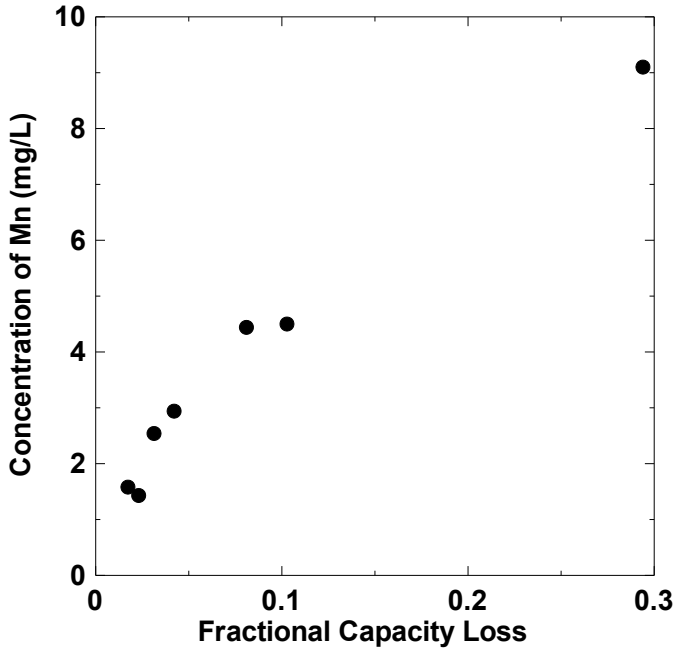

Figure 11.11 Fractional *capacity* loss plotted versus Mn content found in the Li negative electrode of LMO/Li cells versus cycle number. LMO/Li cells were charged and discharged at C/10 and at a temperature of 55^{o}C.

Figure 11.12 shows dQ/dV versus V of the three most LMO rich LMO/NMC electrodes at 50°C for the 2nd, 5th and 10th cycles. For the two NMC-containing electrodes there is a very stable peak at ~ 3.75 V caused by the presence of NMC. The two LMO peaks at ~ 4.00 V and ~ 4.15 V changed with cycle number but became more stable as the NMC content increased. This suggests two things; that the principal contributor to the *capacity* loss of the mixed electrodes was the LMO component, and

that somehow NMC stabilizes LMO during cycling. The right hand column of Figure 11.12 shows the effect of this stabilization in an expanded view of the 4.15 V LMO peak. The peaks do not drop proportionally with LMO content. By the tenth cycles the 50%:50%, 75%:25% and 100%:0% electrodes drop by 33.9 mAh/gV, 102.6 mAh/gV and 186.3 mAh/gV respectively. As in Figure 11.3, this suggests that adding NMC to an LMO electrode can somehow dramatically improve the cyclability.

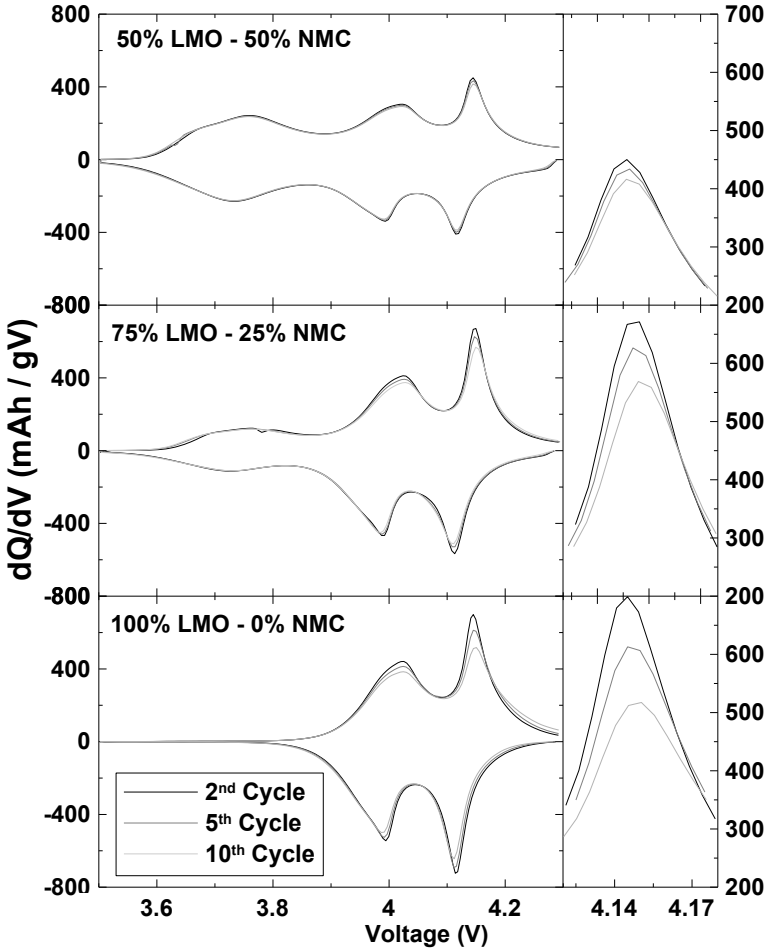

Figure 11.12 dQ/dV versus V of the three most LMO-rich electrodes at 50°C charged and discharged at C/10.

Figure 11.13 shows dQ/dV versus V for the same cells described by Figure 11.12, but only the LMO component. This Figure was prepared by fitting the 3.75 V NMC peak

of the mixed electrodes with the dQ/dV vs. V of the pristine NMC electrode cycling at the same temperature. Once a proper fit was made, the dQ/dV versus V of the NMC component was subtracted from the dQ/dV versus V of the mixed electrode leaving only the LMO dQ/dV versus V behind. The three LMO dQ/dV versus V curves changed in a similar way. The ~ 4.00 V and ~ 4.15 V LMO peaks decreased in height, the dQ/dV versus V level above 4.18 V increased and the ~ 4.09 V minimum remained about at a constant height with cycling. If the *capacity* loss was simply a matter of loss of active material, it would stand to reason that dQ/dV versus V of the LMO component would decrease proportionally and maintain its original shape. If serious impedance increases were occurring, the ~ 4.00 V and ~ 4.15 V LMO peaks would have shifted to higher potentials. This is not the case.

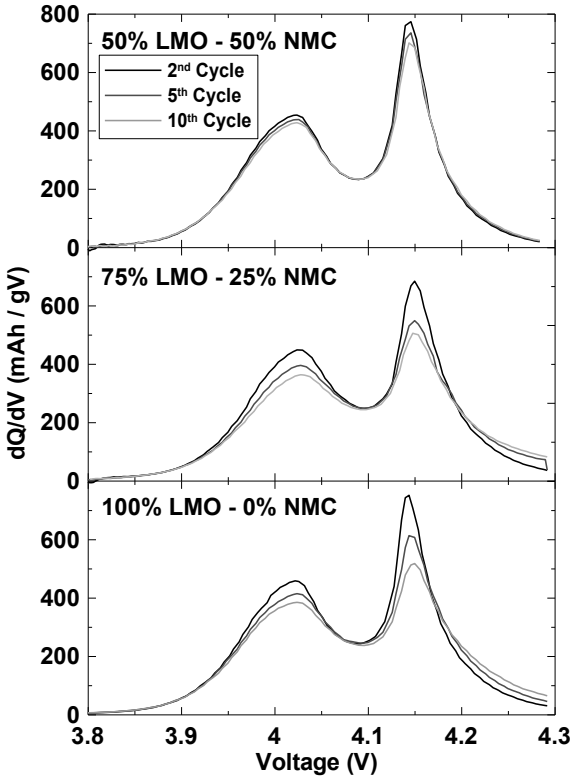

Figure 11.13 LMO component of the dQ/dV versus V of the three most LMO-rich electrodes at 50°C charged and discharged at C/10.

The dQ/dV versus V curve of $Li_{1+x}Mn_{2-x}O_4$/Li cells changes systematically with x [144]. Peaks decease in height as x increases, just as is observed in Figure 11.13. This suggests that Mn dissolution is occurring, leading to a material with excess lithium that has lower specific *capacity*. We do not claim that the materials are exactly $Li_{1+x}Mn_{2-x}O_4$ throughout every particle as it is most likely the Mn loss is most severe at the surface of the particles. Hence x in $Li_{1+x}Mn_{2-x}O_4$ most likely is larger at the particle surfaces than in the interior. This should lead to a broadening of XRD patterns of the electrode material taken after some cycles since the lattice constant depends on x [144].

Figure 11.14 shows the XRD pattern of a pristine LMO electrode and 3 other LMO electrodes cycled on the HPC 2, 5 or 9 times at 50 ^oC. The XRD peaks broaden with cycling suggesting a range of lattice constants within each particle as suggested above.

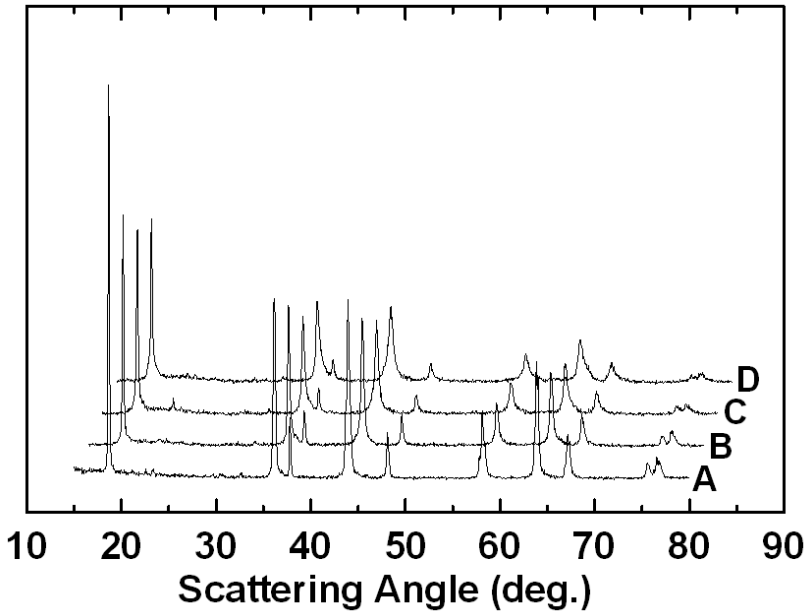

Figure 11.14 XRD of a pristine LMO electrode (A) and LMO electrodes charged and discharge 2 (B), 5 (C) or 9 (D) times. X-rays of the cycled electrodes were collected after they were equilibrated at 3.0 V vs. Li/Li^+. Each successive XRD spectra has been shifted vertically and horizontally for clarity

Figure 11.15 shows the dQ/dV versus V (left panel) for the last charge of the electrodes described by the XRD patterns shown in Figure 11.14. The dQ/dV vs. V curves of the cells were consistent with those seen for the 100% LMO electrode in Figure 11.12. Figure 11.15 also shows selected expanded views of the XRD pattern (right panel) in Figure 11.14. For example, the (311) Bragg peak is indicated near 36.3° in Figure 11.15. The majority of the peaks in Figures 11.14 and 11.15 show broadening on the right hand side consistent with $Li_{1+x}Mn_{2-x}O_4$ with a larger value of x (smaller lattice constant) forming at the surface of the particles. Figure 2 in reference [145] gives the lattice constants versus x in $Li_{1+x}Mn_{2-x}O_4$ and shows that a = 8.12 Å for x = 1/3, the limit of x when all the Mn is in the 4+ oxidation state. If a = 8.22 Å, then the (311) Bragg peak should appear at a scattering angle of 36.24° and if a = 8.12 Å, the (311) peak is at 36.70°. Figure 11.15 shows that the (311) peak is initially near 36.2° but, with cycling, develops a broad shoulder that could arise from a broad peak centered near 36.7°,

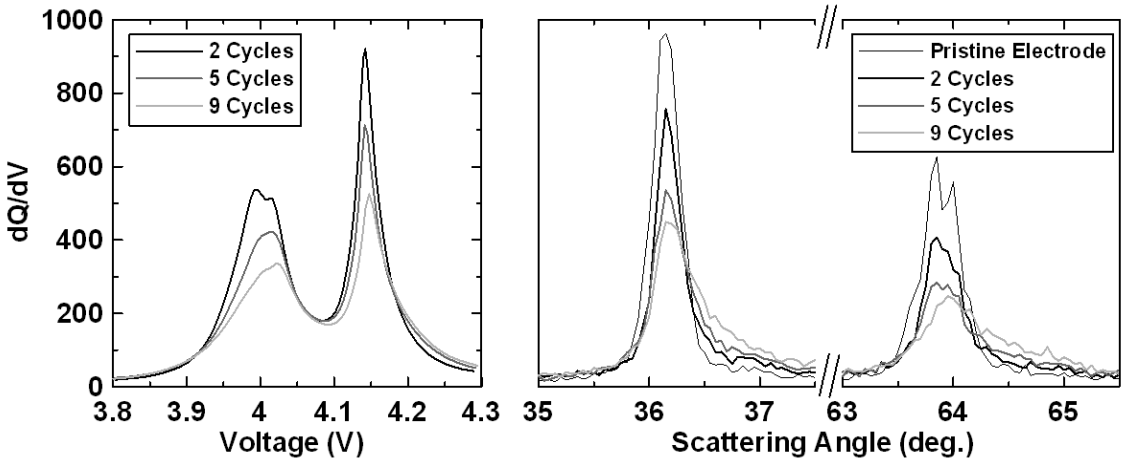

Figure 11.15 dQ/dV vs. V of the last charge for the cells described by Figure 11.14 (Left Panel). Expanded views of the XRD patterns of a pristine LMO electrode and LMO electrodes charged and discharged 2, 5 or 9 times (as indicated).

consistent with the formation of a thin surface layer of $Li_{1+x}Mn_{2-x}O_4$ with x near 1/3. Tarascon's group has reported similar XRD patterns for LMO electrodes exposed to 100°C temperatures in short term storage tests [68,146,147]. In the most recent of these reports [147] they concluded that this new phase was a Li rich protonated phase. This may be the case, but we also believe the data in Figures 11.14 and 11.15 are simply consistent with $Li_{1+x}Mn_{2-x}O_4$ [148].

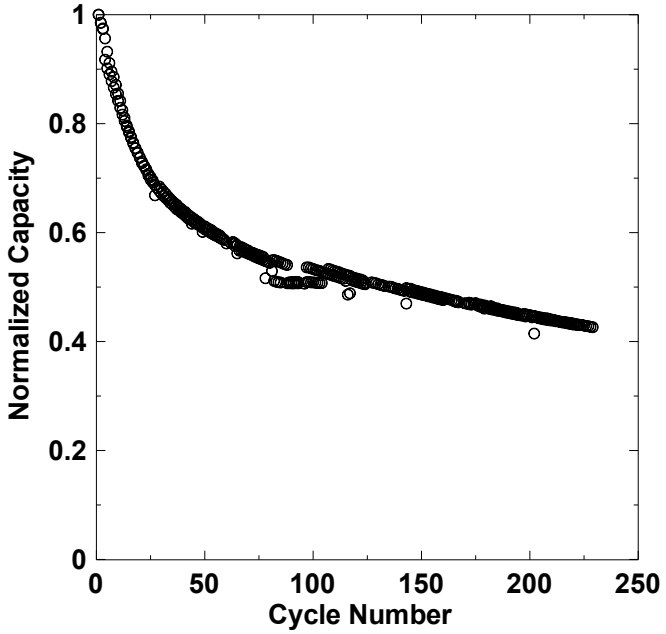

Figure 11.16 Fractional *capacity* of two LMO/graphite 18650 cells versus cycle number. The nominal 1400 mAh cells were tested at 55°C using charge and discharge currents of 25 mA. The cells were cycled between 3.0 and 4.2 V. Seventeen months of continuous testing is shown here.

Figure 11.16 shows the *capacity* versus cycle number for extended long-term cycling of two commercial LMO/graphite 1400 mAh 18650 cells [from a well-known manufacturer]. The cells were charged and discharged at 25 mA between 3.0 and 4.2 V at 55°C. The data represents 17 months of continuous cycling at 55°C. The cells lost *capacity* dramatically at the beginning. As time went on, x in $Li_{1+x}Mn_{2-x}O_4$ presumably

increased and the specific *capacity* dropped ($Q_{specific} \approx 148$ (1-3x) mAh/g) but the Mn dissolution apparently slowed greatly and the *capacity* more or less stabilized eventually. Much of the *capacity* lost in Figure 11.16 was due to consumption of lithium in the SEI at the graphite electrode as has been shown in numerous publications [34,67,69,128,130]. The SEI is thought to be damaged by the incorporation of Mn, so as Mn dissolution slowed as x in $Li_{1+x}Mn_{2-x}O_4$ increases, the *capacity* loss rate decreased.

Similar to the publication by Numata et al. [131] it is clear that that the presence of another positive electrode material helps reduce mechanisms where Mn dissolution is produced from LMO electrodes [131]. Hence, electrodes containing more NMC are apparently better able to slow down these reactions and then apparently x in $Li_{1+x}Mn_{2-x}O_4$ increases more slowly with cycle number.

Physical mixing of electrode materials offers many possibilities to researchers and battery manufacturers, because the short-comings of one electrode material can be compensated by the advantages of another. Most interesting is that often the mixture performs better than expected due to some synergistic interplay between the materials as is the case in the experiments reported here. A full understanding of these synergistic effects, beyond the scope of this report, is required to push Li-ion battery technology as far as it can go.

Chapter 12 Conclusion and Future Work

12.1 Conclusion

Li-ion batteries are used in cell phones, digital cameras, laptop computers and other portable electronic devices because of their high energy density and long life time. Li-ion batteries now outlive many of the devices they power. New applications such as electrified vehicles, satellites and grid energy storage need Li-ion batteries with longer calendar lives than those for portable electronics applications. However, to ensure that the cells have the required life times is problematic because it would take an extremely long time to test. In an attempt to show that cells can survive some desired number of cycles many battery manufactures and researchers use high rate cycling to evaluate their cells. Figure 9.6 shows that such accelerated testing may, however, lead to spurious conclusions about cycle life under realistic conditions. This thesis shows that precision coulometry and storage techniques are more useful for evaluating cell failure mechanisms and lifetimes than traditional battery testing equipment.

High precision coulometry not only provides accurate coulombic efficiency measurements, but also allows the slippage of the charge and discharge endpoints to be carefully detected. As discussed in Chapter 3 the motion of these endpoints is associated with various parasitic reactions occurring inside cell, such as the growth of the SEI, electrolyte oxidation, electrode damage, etc. Therefore, changes in the slippage rate of a cell can lead to an understanding of how different electrode materials, electrolytes, electrolyte additives or cycling conditions impact the components of the cell. This

technique, however, does not give information about the mechanisms but allows the impact of all the mechanisms to be measured.

dV/dQ analysis was also shown as a powerful technique for evaluating the failure mechanisms of Li-ion cells. The dV/dQ program allows the potential versus Li and absolute *capacity* of each electrode in a full cell to be determined from simple voltage versus *capacity* charge-discharge cycling data from a full cell. Chapter 6 showed that by matching the calculated dV/dQ fits from the program to the experimental dV/dQ versus V results, the electrode slippage and *capacity* loss rates could be accurately determined. There may be no better technique for evaluating and differentiating different *capacity* loss mechanisms in real Li-ion cells.

Precision coulometry has shown that the SEI growth rate and consumption of Li on graphite electrodes can be described quite well with the parabolic growth law [Equations. 8.1–8.3]. This, in turn, means that time, not cycle count, will dominate the loss of lithium at the negative electrode in Li-ion cells cycled at low rates. This has been shown to be the case for graphite half cells (Figure 8.5). Minimizing the negative electrode specific surface area was also shown to be a key factor in reducing the continual loss of lithium from Li-ion cells due to continual SEI growth (Figure 8.8). Many researchers believe that the SEI forms in the first cycle and then stops. This is not the case, at least in the temperature range between 30 and 50°C for 1 M $LiPF_6$ EC:DEC electrolyte. Therefore, high surface area negative electrodes will continue to remove active lithium from cells during cycling and storage faster than low surface area electrodes.

This thesis has shown that the addition of NMC to LMO-based positive electrodes produces a remarkable improvement in the *capacity* retention of the cells at elevated temperatures. Even with a modest addition of NMC to a LMO electrode, the *capacity* retention was significantly better than expected when compared to a prediction based on the sum of the results for the individual positive electrode materials (Figure 11.3). It was also found that NMC helps to suppress Mn dissolution from LMO, and that this dissolution is a major contributor to the *capacity* loss and coulombic inefficiency of the LMO/Li cells (Figure 11.7). This data showed that high precision coulomtry could be used to directly measure parasitic processes like metal ion dissolution. This study also showed that in the presence of NMC the electrodes retained more Mn ions and helped to prevent the LMO material from forming into a more Li rich, lower *capacity*, phase on the particles surfaces.

This thesis also showed commercial $LiCoO_2$ and $Li[NiCoMn]O_2$/graphite cells cycling between narrow voltage limits and stored at various voltages. It was found that narrow range cycling is a useful technique for identifying the relative amount of damage caused in cells by cycling the cells between different voltage limits. Thus researchers could use these kinds of tests to assess the ideal voltage limit for different cell chemistries. Storage experiments performed on the same cell chemistries also revealed similar problems caused by electrolyte oxidation. High precision narrow range cycling and storage experiment results should be used in concert to extract information about the different parasitic currents that occur in a Li-ion cell.

It is our opinion that high precision coulometry is a useful tool that should be used widely by Li-ion battery researchers. It is highly unfortunate that commercially available

battery cyclers lack the required precision for these experiments at this time. We encourage battery cycler manufacturers to produce equipment with the required precision for these studies.

12.2 Future Work

The work performed for this thesis lays the basic foundation for studies involving the precision coulometry of Li-ion batteries. However, despite the advancements of the HPC it can still only measure CE with an estimated accuracy and precision of about 0.01%. For a battery to meet the more preferable goal of 10000 cycles, it would have to have a CE of at least 99.999% which means the HPC would have to be able to measure CE to an accuracy and precision of one part in 10^5. In order to improve the HPC, the specifications of accuracy and precision described in Table 4.1 need to be more carefully controlled. To improve the accuracy of the delivered current, the current could be measured using a precision voltmeter measuring the potential drop across a precision resistor placed in series with the cell under test. Electronic equipment can often be sensitive to changes in the ambient temperature in which they are stored. The precision of the measured cell voltage could hence be improved by temperature controlling the voltmeters

The length of time between voltage measurements could be shortened by reducing the number of channels on a single system and improving the operating software. The current operating software was written in LabVIEW™ which like most visual programming languages is relatively slow. In addition, the HPC has 10 channels per system and spends an average of 500 msec per channel, thus each channel can only be

monitored every 5 seconds. A streamlined operating system and a reduced number of channels per system would allow every channel to be monitored on a more regular basis and help reduce time related errors.

Fluctuations in cell temperature could be reduced by equipping each cell with an individual heat sink. The thermostats used by the HPC have been shown to vary by only 0.25°C over long times, however heat sinks would average over these changes and reduce variations in cell temperature. As the coulombic efficiency of well made Li-ion cells approach values closer and closer to unity, more accurate battery testing systems will be needed to detect the small deviations from a "perfect" CE of 1.000000….

In this thesis studies like precision coulometry, storage tests and dV/dQ analysis were introduced as a means of monitoring degradation in Li-ion cells. However, other studies can also be used to understand the different failure mechanisms occurring inside the cells. Electrochemical impedance spectroscopy can be used to measure small changes in the internal impedance of a cell. When cycling with large currents, growth in the internal impedance of a cell can cause an increase in the polarization of the cell voltage, which can result in *capacity* loss. Using impedance spectroscopy, the impact of different cell chemistries on the internal impedance of a cell can be quantified, so that the best cell design can be chosen. In fact, AC impedance measurements on cells tested on the high precision charger are now a standard in our lab [149], introduced after the author's experiments were completed

These electrochemical tests allow the impact of different cell chemistries to be measured, but do not identify the exact mechanisms occurring in the cell. Ex-situ material analysis studies can be done to better understand the nature of the failure

mechanism. If the mechanisms behind the unwanted reactions could be understood, work could be done to develop solutions to improve cell performance. Ex-situ tests, such as X-ray photoelectron spectroscopy [150–152] are now possible using the new organic XPS system recently commissioned by Ian Hill.

In this thesis, different positive and negative electrodes, voltage ranges and slow cycling rates were tested to observe the impact these parameters have on the coulombic efficiency of the cells. Certainly, the combination of tests involving the above parameters could be endless. Not shown in this thesis are high precision tests involving different electrolytes, salts and electrolyte additives performed by Chris Burns and Nupur Sinha [35,149,153]. The HPC is very useful in detecting the effect these electrolyte additives have during the initial cycles of the cell, so that the best combination of electrolyte additives can be quickly screened and selected for production.

Tests involving high rate cycling on the HPC would allow the effects of Li plating on the negative electrode to be carefully quantified. These tests would be particularly useful in the automotive industry, where Li plating is often caused by the large currents, from regenerative braking, that quickly charge the batteries in electrified vehicles.

As the cycle life for Li-ion cells increase, the techniques used to test the cell must improve as well. Combinations of precision coloumetery, storage, dV/dQ analysis and impedance spectroscopy experiments help to identify the failure mechanisms occurring inside the cells that will eventually limit cell performance. Combinations of carefully conducted experiments examining parasitic reactions allow for a thorough screening of new electrode materials, electrolyte, additives and cell designs that will produce longer cycle lives and meet the industrial demands of the future.

Bibliography

[1] L. Li, X. Li, Z. Wang, H. Guo, P. Yue, W. Chen, and L. Wu, *J. of Alloys and Compounds*, **507**, 172-177 (2010).

[2] S.-T. Myung, K. Izumi, S. Komaba, Y.-K. Sun, H. Yashiro, and N. Kumagai, *Chem. Mater*., **17**, 3695-3704 (2005).

[3] K. Striebel, J. Shim, A. Sierra, H. Yang, X. Song, R. Kostecki, and K. McCarthy, *J. of Power Sources,* **146**, 33-38 (2005).

[4] J.-M. Tarascon, A. S. Gozdz, C. Schmutz, F. Shokoohi, and P. C. Warren, *Solid State Ionics,* **86–88**, 49-54 (1996).

[5] Y. P. Wu, E. Rahm, and R. Holze, *J. of Power Sources*, **114**, 228-236 (2003).

[6] M. Broussely, P. Biensan, F. Bonhomme, P. Blanchard, S. Herreyre, K. Nechev, and R. J. Staniewicz, *J. of Power Sources*, **146**, 90-96 (2005).

[7] M. Broussely, S. Herreyre, P. Biensan, P. Kasztejna, K. Nechev, and R. . Staniewicz, *J. of Power Sources*, **97–98**, 13-21 (2001).

[8] K. Asakura, M. Shimomura, and T. Shodai, *J. of Power Sources*, **119–121**, 902-905 (2003).

[9] D. Aurbach, B. Markovsky, A. Rodkin, E. Levi, Y. Cohen, H.-J. Kim, and M. Schmidt, *Electrochimica Acta*, **47**, 4291-4306 (2002).

[10] B. Markovsky, A. Rodkin, Y. Cohen, O. Palchik, E. Levi, D. Aurbach, H.-J. Kim, and M. Schmidt, *J. of Power Sources*, **119**, 504-510 (2003).

[11] R. P. Ramasamy, R. E. White, and B. N. Popov, *J. of Power Sources*, **141**, 298-306 (2005).

[12] E. Scott, J. Brown, C. Schmidt, and W. Howard, *Electrochem. Soc. Meeting Abs*., **502**, 239 (2005).

[13] K. Xu, *Chem. Rev.,* **104**, 4303-4418 (2004).

[14] H. Yamane, T. Inoue, M. Fujita, and M. Sano, *J. of Power Sources*, **99**, 60-65 (2001).

[15] K. Abe, Y. Ushigoe, H. Yoshitake, and M. Yoshio, *J. of Power Sources*, **153**, 328-335 (2006).

[16] Y. Li, R. Zhang, J. Liu, and C. Yang, *J. of Power Sources*, **189**, 685-688 (2009).

[17] S. Patoux, L. Daniel, C. Bourbon, H. Lignier, C. Pagano, F. Le Cras, S. Jouanneau, and S. Martinet, *J. of Power Sources*, **189**, 344-352 (2009).

[18] L. El Ouatani, R. Dedryvere, C. Siret, P. Biensan, and D. Gonbeau, *J. Electrochem. Soc.,* **156**, A468-A477 (2009).

[19] K. Abe, K. Miyoshi, T. Hattori, Y. Ushigoe, and H. Yoshitake, *J. of Power Sources*, **184**, 449-455 (2008).

[20] G. H. Wrodnigg, J. O. Besenhard, and M. Winter, *J. Electrochem. Soc*., **146**, 470-472 (1999).

[21] K.-S. Lee, S.-T. Myung, K. Amine, H. Yashiro, and Y.-K. Sun, *J. Mater. Chem*., **19**, 1995-2005 (2009).

[22] Y.-K. Sun, S.-T. Myung, C. S. Yoon, and D.-W. Kim, *Electrochem. Solid-State Lett*., **12**, A163-A166 (2009).

[23] Y.-K. Sun, S.-W. Cho, S.-W. Lee, C. S. Yoon, and K. Amine, *J. Electrochem. Soc*., **154**, A168-A172 (2007).

[24] Y.-K. Sun, S.-T. Myung, B.-C. Park, J. Prakash, I. Belharouak, and K. Amine, *Nat Mater.*, **8**, 320-324 (2009).

[25] G. Li, Z. Yang, and W. Yang, *J. of Power Sources*, **183**, 741-748 (2008).

[26] Z. Chen and J. R. Dahn, *Electrochimica Acta,* **49**, 1079-1090 (2004).

[27] J. Wang, Y. Bai, M. Wu, J. Yin, and W. F. Zhang, *J. of Power Sources*, **191**, 614-618 (2009).

[28] T.-F. Yi, C.-Y. Li, Y.-R. Zhu, J. Shu, and R.-S. Zhu, *J. of Solid State Electrochem.,* **13**, 913-919 (2008).

[29] T. Song, J. Xia, J.-H. Lee, D. H. Lee, M.-S. Kwon, J.-M. Choi, J. Wu, S. K. Doo, H. Chang, W. I. Park, D. S. Zang, H. Kim, Y. Huang, K.-C. Hwang, J. A. Rogers, and U. Paik, *Nano. Lett.,* **10**, 1710-1716 (2010).

[30] M. Zhang, D. Lei, X. Yin, L. Chen, Q. Li, Y. Wang, and T. Wang, *J. Mater. Chem*., **20**, 5538-5543 (2010).

[31] M. N. Obrovac and L. J. Krause, J. Electrochem. Soc., **154**, A103-A108 (2007).

[32] A. J. Smith, J. C. Burns, S. Trussler, and J. R. Dahn, *J. Electrochem. Soc.,* **157**, A196 (2010).

[33] A. J. Smith, J. C. Burns, D. Xiong, and J. R. Dahn, *J. Electrochem. Soc.*, **158**, A1136 (2011).

[34] A. J. Smith, J. C. Burns, and J. R. Dahn, *Electrochem. and Solid-State Lett.*, **14**, A39 (2011).

[35] J. C. Burns, G. Jain, A. J. Smith, K. W. Eberman, E. Scott, J. P. Gardner, and J. R. Dahn, *J. Electrochem. Soc.*, **158**, A255 (2011).

[36] A. J. Smith, J. C. Burns, X. Zhao, D. Xiong, and J. R. Dahn, *J. Electrochem. Soc.*, **158**, A447 (2011).

[37] A. J. Smith, J. C. Burns, and J. R. Dahn, *Electrochem. and Solid-State Lett.* **13**, A177 (2010).

[38] D. Gerard and A. Herold, *Carbon*, **13**, 337-339 (1975).

[39] J.-M. Tarascon and M. Armand, *Nature*, **414**, 359-367 (2001).

[40] L. Xiao, Y. Zhao, Y. Yang, X. Ai, H. Yang, and Y. Cao, *J. of Solid State Electrochem.*, **12**, 687-691 (2007).

[41] K. Shaju, G. Subba Rao, and B. V. . Chowdari, *Electrochimica Acta,* **48**, 145-151 (2002).

[42] P. Arora, B. Popov, and R. White, *J. Electrochem. Soc.*, 807-815 (1998).

[43] K. S. Park, J. T. Son, H. T. Chung, S. J. Kim, C. H. Lee, and H. G. Kim, *Electrochem. Com.*, **5**, 839-842 (2003).

[44] K. Kondo, M. Sano, A. Hiwara, T. Omi, M. Fujita, A. Kuwae, M. Iida, K. Mogi, and H. Yokoyama, *J. Phys. Chem. B*, **104**, 5040-5044 (2000).

[45] T. Kawamura, S. Okada, and J. Yamaki, *J. of Power Sources*, **156**, 547-554 (2006).

[46] S. Wang, W. Qiu, Y. Guan, B. Yu, H. Zhao, and W. Liu, *Electrochimica Acta*, **52**, 4907-4910 (2007).

[47] I. Kuribayashi, M. Yokoyama, and M. Yamashita, *J. of Power Sources,* **54**, 1-5 (1995).

[48] K. Hayamizu and Y. Aihara, *Electrochimica Acta*, **49**, 3397-3402 (2004).

[49] T. Reddy, *Linden's Handbook of Batteries, 4th Edition*, 4th ed. (McGraw-Hill Professional, 2010).

[50] J. Christensen and J. Newman, *J. Electrochem. Soc.*, **150**, A1416-A1420 (2003).

[51] J. Christensen and J. Newman, *J. Electrochem. Soc.*, **152**, A818-A829 (2005).

[52] D. Aurbach, Y. Ein-Eli, O. C. (Youngman), Y. Carmeli, M. Babai, and H. Yamin, *J. Electrochem. Soc.,* **141**, 603-611 (1994).

[53] M.-Q. Li, M.-Z. Qu, X.-Y. He, and Z.-L. Yu, *Electrochimica Acta*, **54**, 4506-4513 (2009).

[54] G. E. Blomgren, *J. of Power Sources*, **81**, 112-118 (1999).

[55] K. Araki and N. Sato, *J. of Power Sources*, **124**, 124-132 (2003).

[56] R. Wright, J. Christophersen, C. Motloch, J. Belt, C. Ho, V. Battaglia, J. Barnes, T. Duong, and R. Sutula, *J. of Power Sources*, **119**, 865-869 (2003).

[57] D. Aurbach, Y. Gofer, and J. Langzam, *J. Electrochem. Soc*., **136**, 3198-3205 (1989).

[58] M. Q. Xu, W. S. Li, X. X. Zuo, J. S. Liu, and X. Xu, *J. of Power Sources*, **174**, 705-710 (2007).

[59] H. J. Ploehn, P. Ramadass, and R. E. White, *J. Electrochem. Soc*., **151**, A456-A462 (2004).

[60] G. Pistoia, A. Antonini, R. Rosati, and D. Zane, *Electrochimica Acta*, **41**, 2683-2689 (1996).

[61] J. Chen, C. Buhrmester, and J. R. Dahn, *Electrochem. and Solid-State Lett.*, **8**, A59 (2005).

[62] K. Edström, T. Gustafsson, and J. O. Thomas, *Electrochimica Acta*, **50**, 397-403 (2004).

[63] G. G. Amatucci, J. M. Tarascon, and L. C. Klein, *Solid State Ionics*, **83**, 167-173 (1996).

[64] A. Manthiram and R. Chebiam, *Ceram. Trans*., **109**, 277 (2000).

[65] K. Amine, J. Liu, and I. Belharouak, *Electrochem. Com*., **7**, 669-673 (2005).

[66] S. K. Martha, H. Sclar, Z. Szmuk Framowitz, D. Kovacheva, N. Saliyski, Y. Gofer, P. Sharon, E. Golik, B. Markovsky, and D. Aurbach, *J. of Power Sources,* **189**, 248-255 (2009).

[67] G. Amatucci, A. Du Pasquier, A. Blyr, T. Zheng, and J.-M. Tarascon, *Electrochimica Acta*, **45**, 255-271 (1999).

[68] A. Du Pasquier, *J. Electrochem. Soc.*, **146**, 428-429 (1999).

[69] J. Vetter, P. Novák, M. R. Wagner, C. Veit, K.-C. Möller, J. O. Besenhard, M. Winter, M. Wohlfahrt-Mehrens, C. Vogler, and A. Hammouche, *J. of Power Sources*, **147**, 269-281 (2005).

[70] N. Tran, L. Croguennec, C. Labrugère, C. Jordy, P. Biensan, and C. Delmas, *J. Electrochem. Soc.*, **153**, A261 (2006).

[71] K. S. Tan, M. V. Reddy, G. V. S. Rao, and B. V. R. Chowdari, *J. of Power Sources*, **147**, 241-248 (2005).

[72] J. R. Dahn and R. R. Haering, *Can. J. Phys*., **61**, 1093 (1983).

[73] N. N. Sinha, A. J. Smith, J. C. Burns, G. Jain, K. W. Eberman, E. Scott, J. P. Gardner, and J. R. Dahn, *J. Electrochem. Soc.*, **158**, A1194 (2011).

[74] K. Takeno, M. Ichimura, K. Takano, and J. Yamaki, *J. of Power Sources*, **142**, 298-305 (2005).

[75] A. R. Armstrong, A. J. Paterson, A. D. Robertson, and P. G. Bruce, *Chem. Mater.*, **14**, 710-719 (2002).

[76] G. Armstrong, A. R. Armstrong, J. Canales, and P. G. Bruce, *Electrochem. and Solid-State Lett.*, **9**, A139 (2006).

[77] A. D. Robertson, A. R. Armstrong, and P. G. Bruce, *Chem. Mater.*, **13**, 2380-2386 (2001).

[78] L. Croguennec, P. Deniard, R. Brec, P. Biensan, and M. Broussely, *Solid State Ionics*, **89**, 127-137 (1996).

[79] M. Dubarry, V. Svoboda, R. Hwu, and B. Yann Liaw, *Electrochem. and Solid-State Lett.*, **9**, A454 (2006).

[80] M. Dubarry and B. Y. Liaw, *J. of Power Sources*, **194**, 541-549 (2009).

[81] M. Dubarry, B. Y. Liaw, M.-S. Chen, S.-S. Chyan, K.-C. Han, W.-T. Sie, and S.-H. Wu, *J. of Power Sources*, **196**, 3420-3425 (2011).

[82] D. D. MacNeil, Z. Lu, and J. R. Dahn, *J. Electrochem. Soc.*, **149**, A1332 (2002).

[83] Y. W. Xiao, *J. Electrochem. Soc.*, **146**, 3623 (1999).

[84] T. Ohzuku, *J. Electrochem. Soc.*, **140**, 2490 (1993).

[85] J. Barker, M. Y. Saidi, and J. L. Swoyer, *Solid State Ionics*, **167**, 413-418 (2004).

[86] S. Brown, K. Ogawa, Y. Kumeuchi, S. Enomoto, M. Uno, H. Saito, Y. Sone, D. Abraham, and G. Lindbergh, *J. of Power Sources*, **185**, 1454-1464 (2008).

[87] P.-C. J. Chiang, M.-S. Wu, and J.-C. Lin, *Electrochem. and Solid-State Lett.*, **8**, A423 (2005).

[88] Y. Zhang and C.-Y. Wang, *J. Electrochem. Soc.*, **156**, A527 (2009).

[89] J. P. Christophersen, C. D. Ho, C. G. Motloch, D. Howell, and H. L. Hess, *J. Electrochem. Soc.*, **153**, A1406 (2006).

[90] I. Bloom, A. N. Jansen, D. P. Abraham, J. Knuth, S. A. Jones, V. S. Battaglia, and G. L. Henriksen, *J. of Power Sources*, **139**, 295-303 (2005).

[91] I. Bloom, J. P. Christophersen, D. P. Abraham, and K. L. Gering, *J. of Power Sources*, **157**, 537-542 (2006).

[92] K. Honkura, H. Honbo, Y. Koishikawa, and T. Horiba, *Electrochem. Soc. Trans*., **13**, 61-73 (2008).

[93] J. R. Dahn, *Phys. Rev. B*, **44**, 9170-9177 (1991).

[94] B. D. Cullity, *Elements of X-Ray Diffraction*, 2nd ed. (Addison-Wesley, 1978).

[95] B. E. Warren, *X-ray Diffraction* (Addison-Wesley Educational Publishers Inc, 1968).

[96] R. Dunlap, D. Small, D. MacNeil, M. Obrovac, and J. Dahn, *J. of Alloys and Compounds*, **289**, 135-142 (1999).

[97] S. Brunauer, P. H. Emmett, and E. Teller, *J. Am. Chem. Soc.*, **60**, 309-319 (1938).

[98] W. Salvin, *Atomic Absorption Spectroscopy* (Interscience Publishers, N.Y., 1968).

[99] E. Peled, *J. Electrochem. Soc.*, **126**, 2047 (1979).

[100] E. Peled, *J. Electrochem. Soc.*, **144**, L208 (1997).

[101] K. Xu, U. Lee, S. S. Zhang, and T. R. Jow, *J. Electrochem. Soc.*, **151**, A2106 (2004).

[102] R. Fong, U. Sacken, and J. R. Dahn, *J. Electrochem. Soc.*, **137**, 2009 (1990).

[103] Z. Ogumi and M. Inaba, *Bulletin of the Chem. Soc. of Japan,* **71**, 521-534 (1998).

[104] F. Kong, *Electrochem. and Solid-State Lett.*, **1**, 39 (1999).

[105] D. Aurbach, M. L. Daroux, P.W. Faguy, and E. Yeager, *J. Electrochem. Soc.*, **134**, 1611 (1987).

[106] K. R. Lawless, *Reports on Progress in Physics*, **37**, 231-316 (1974).

[107] R. Spotnitz, *J. of Power Sources*, **113**, 72-80 (2003).

[108] P. Ramadass, B. Haran, R. White, and B. N. Popov, *J. of Power Sources*, **123**, 230-240 (2003).

[109] T. Yoshida, M. Takahashi, S. Morikawa, C. Ihara, H. Katsukawa, T. Shiratsuchi, and J. Yamaki, *J. Electrochem. Soc.*, **153**, A576 (2006).

[110] R. Wright, C. Motloch, J. Belt, J. Christophersen, C. Ho, R. Richardson, I. Bloom, S. Jones, V. Battaglia, G. Henriksen, T. Unkelhaeuser, D. Ingersoll, H. Case, S. Rogers, and R. Sutula, *J. of Power Sources*, **110**, 445-470 (2002).

[111] I. Bloom, B. Cole, J. Sohn, S. Jones, E. Polzin, V. Battaglia, G. Henriksen, C. Motloch, R. Richardson, T. Unkelhaeuser, D. Ingersoll, and H. Case, *J. of Power Sources,* **101**, 238-247 (2001).

[112] A. M. Colclasure, K. A. Smith, and R. J. Kee, *Electrochimica Acta*, **58**, 33-43 (2011).

[113] J. Christensen and J. Newman, *J. Electrochem. Soc.*, **151**, A1977 (2004).

[114] M.-H. Park, M. G. Kim, J. Joo, K. Kim, J. Kim, S. Ahn, Y. Cui, and J. Cho, *Nano Lett.*, **9**, 3844-3847 (2009).

[115] X. Li, F. Kang, X. Bai, and W. Shen, *Electrochem. Comm.*, **9**, 663-666 (2007).

[116] F. Robert, P. E. Lippens, R. Fourcade, J. C. Jumas, F. Gillot, J. M. Morcrette, and J. M. Tarascon, *Hyperfine Interact.*, **167**, 797 (2006).

[117] Q. Zhang and R. E. White, *J. of Power Sources*, **179**, 793-798 (2008).

[118] T. Ohzuku, A. Ueda, N. Yamamoto, and Y. Iwakoshi, *J. of Power Sources,* **54**, 99-102 (1995).

[119] I. A. Courtney and J. R. Dahn, *J. Electrochem. Soc.*, **144**, 2943 (1997).

[120] I. A. Courtney and J. R. Dahn, *J. Electrochem. Soc.*, **144**, 2045 (1997).

[121] J. Yang, Y. Takeda, N. Imanishi, and O. Yamamoto, *Electrochimica Acta*, **46**, 2659-2664 (2001).

[122] Y. Wang and J. Y. Lee, *J. Phys. Chem. B*, **108**, 17832-17837 (2004).

[123] R. Dominko, C. V.-A. Garrido, M. Bele, M. Kuezma, I. Arcon, and M. Gaberscek, *J. of Power Sources*, **196**, 6856-6862 (2011).

[124] S. Nordlinder, L. Nyholm, T. Gustafsson, and K. Edström, *Chem. Mater.*, **18**, 495-503 (2005).

[125] C.-N. Li, J.-M. Yang, V. Krasnov, J. Arias, and K.-W. Nieh, *Applied Physics Lett*., **90**, 263102-263102-3 (2007).

[126] G. Sarre, P. Blanchard, and M. Broussely, *J. of Power Sources*, **127**, 65-71 (2004).

[127] G. G. Amatucci, N. Pereira, T. Zheng, and J.-M. Tarascon, *J. Electrochem. Soc.*, **148**, A171 (2001).

[128] G. Amatucci and J.-M. Tarascon, *J. Electrochem. Soc.*, **149**, K31 (2002).

[129] M. Wohlfahrt-Mehrens, C. Vogler, and J. Garche, *J. of Power Sources*, **127**, 58-64 (2004).

[130] T. Tsujikawa, K. Yabuta, T. Matsushita, M. Arakawa, and K. Hayashi, *Electrochem. Soc. Trans*., **25**, 309-315 (2010).

[131] T. Numata, C. Amemiya, T. Kumeuchi, M. Shirakata, and M. Yonezawa, *J. of Power Sources*, **97**, 358-360 (2001).

[132] Z. F. Ma, X. Q. Yang, X. Z. Liao, X. Sun, and J. McBreen, *Electrochem. Comm*., **3**, 425-428 (2001).

[133] S.-T. Myung, M. H. Cho, H. T. Hong, T. H. Kang, and C.-S. Kim, *J. of Power Sources*, **146**, 222-225 (2005).

[134] S.-T. Myung, K. Hosoya, S. Komaba, H. Yashiro, Y.-K. Sun, and N. Kumagai, *Electrochimica Acta*, **51**, 5912-5919 (2006).

[135] A. Manthiram and W. Choi, *Electrochem. and Solid-State Lett.*, **10**, A228 (2007).

[136] P. Albertus, J. Christensen, and J. Newman, *J. Electrochem. Soc.*, **156**, A606 (2009).

[137] S. K. Jeong, J. S. Shin, K. S. Nahm, T. Prem Kumar, and A. M. Stephan, *Mat. Chem. and Physics,* **111**, 213-217 (2008).

[138] A. M. Stux and K. E. Swider-Lyons, *J. Electrochem. Soc.*, **152**, A2009 (2005).

[139] H.-S. Kim, S.-I. Kim, and W.-S. Kim, *Electrochimica Acta*, **52**, 1457-1461 (2006).

[140] T. F. Yi, Y. R. Zhu, X. D. Zhu, J. Shu, C. B. Yue, and A. N. Zhou, *Ionics*, **15**, 779 (2009).

[141] H. Kitao, T. Fujihara, K. Takeda, N. Nakanishi, and T. Nohma, *Electrochem. and Solid-State Lett.*, **8**, A87 (2005).

[142] J. F. Whitacre, K. Zaghib, W. C. West, and B. V. Ratnakumar, *J. of Power Sources,* **177**, 528-536 (2008).

[143] N. Imachi, Y. Takano, H. Fujimoto, Y. Kida, and S. Fujitani, *J. Electrochem. Soc.*, **154**, A412 (2007).

[144] Y. Gao and J. R. Dahn, *J. Electrochem. Soc.*, **143**, 1783 (1996).

[145] J. M. Paulsen and J. R. Dahn, *Chem. Mater*., **11**, 3065-3079 (1999).

[146] A. Blyr, A. Pasquier, G. Amatucci, and J.-M. Tarascon, *Ionics*, **3**, 321-331 (1997).

[147] A. du Pasquier, A. Blyr, A. Cressent, C. Lenain, G. Amatucci, and J. Tarascon, *J. of Power Sources*, **81**, 54-59 (1999).

[148] M. S. Whittingham, *Chem. Rev*. **104**, 4271-4302 (2004).

[149] J. C. Burns, N. N. Sinha, D. J. Coyle, G. Jain, C. M. VanElzen, W. M. Lamanna, A. Xiao, E. Scott, J. P. Gardner, and J. R. Dahn, *J. Electrochem. Soc.*, **159**, A85 (2012).

[150] A. Xiao, L. Yang, B. L. Lucht, S.-H. Kang, and D. P. Abraham, *J. Electrochem. Soc.*, **156**, A318 (2009).

[151] W. Li, A. Xiao, B. L. Lucht, M. C. Smart, and B. V. Ratnakumar, *J. Electrochem. Soc.*, **155**, A648 (2008).

[152] W. Li and B. L. Lucht, *J. Electrochem. Soc.*, **153**, A1617 (2006).

[153] D. Xiong, J. C. Burns, A. J. Smith, N. Sinha, and J. R. Dahn, *J. Electrochem. Soc.*, **158**, A1431 (2011).

Appendix A Li Accounting for Narrow Range Cycling

In Chapter 3 a Li inventory model was introduced to account for the loss of Li to the most common parasitic processes in Li-ion cells. In this model each parasitic process has an effective parasitic current and corresponding *capacity* per half cycle of a Li-ion cell. The inventory model can be used to make a mathematical relationship between these parasitic processes and some of the measurable quantities, like coulombic efficiency, charge endpoint *capacity* slippage, *capacity* fade per cycle, and so on. However, the model developed in Chapter 3 only relates these parasitic currents to the measurable quantities for a full Li-ion cell cycled over 100% state of charge in a situation where the negative electrode is completely emptied of Li during each discharge. For the narrow range cycling shown in Figure 3.7, this is not the case and the inventory model developed in Chapter 3 needs to be modified.

To keep track of the effects of the various parasitic processes described above, an inventory of all the active lithium in the cell cycling between narrow voltage limits is maintained. For the purposes of the model it is assumed that the cell has completed a single formation cycle (i.e. the first charge and discharge of the cell) and has finished in a completely discharged state before the first charge.

Using the calculated *capacities* in Table 3.3, the different parasitic processes described in Chapter 3 can be related to some of the measurable quantities of the cell cycling between narrow voltage limits. As observed in Chapter 3, cell A in Figure 3.6 (positive electrode is the limiting electrode at the bottom of discharge) is simply a limiting case of a cell cycling between narrow voltage limits, where K=0. Therefore, only

the general case is treated here. The slippage per cycle of the charge endpoint, Δ_C, and discharge endpoint, Δ_D, can be expressed as:

$$\Delta_C = Q`_c - Q_d = Q_o - K + q_{ox}^a - 3q_p - Q_o + K + q_{ox}^a + q_p$$

$$\Delta_C = 2q_{ox}^a - 2q_p \quad \text{(A.1)}$$

and

$$\Delta_D = Q_c - Q_d = Q_o - K + q_{ox}^a - q_p - Q_o + K + q_{ox}^a + q_p$$

$$\Delta_D = 2q_{ox}^a \quad \text{(A.2)}$$

where Q_d is the discharge *capacity* of the cell and Q_c and $Q`_c$ are the charge *capacities* immediately preceding and following Q_d, respectively. The *capacity* fade per cycle of a Li-ion cell can also be determined by subtracting Equation A.1 from Equation A.2, to give:

$$\text{Fade} = \Delta_D - \Delta_C = 2q_p \quad \text{(A.3)}$$

Using the information in Table 3.3, one obtains:

$$CE = \frac{Q_d}{Q_c} = \frac{Q_o - K - q_{ox}^a - q_p}{Q_o - K + q_{ox}^a - q_p} \quad \text{(A.4)}$$

$$CE \approx 1 - \frac{2q_{ox}^a}{(Q_o - K)} = 1 - \frac{\Delta_D}{(Q_o - K)} \quad \text{(A.5)}$$

where Equation A.5 is a first order approximation of Equation A.4. Equation A.5 also shows that CE can be directly related to Δ_D (Equation A.2) of the cell. The effects of shuttle mechanisms, involving I_{ox}^{b}, have not been included in these expressions for CE, Δ_C, Δ_D, and Fade but will be included next.

Finally, using the expressions for I_{Li}, I_{ox}^{a}, I_{ox}^{b} and I_p in Chapter 3 one can rewrite Equations A.1, A.2, A.3 and A.5 in terms of the parasitic currents:

$$CE = 1 - 2[I_{ox}^{a} + I_{ox}^{b}]/I_A \tag{A.6}$$

$$\Delta_C = 2(Q_o\text{-}K)\,[I_{ox}^{a} - I_p + I_{ox}^{b}]/I_A \tag{A.7}$$

$$\Delta_D = 2(Q_o\text{-}K)\,[I_{ox}^{a} + I_{ox}^{b}]/I_A \tag{A.8}$$

$$Fade = 2(Q_o\text{-}K)\,[I_p]/I_A \tag{A.9}$$

The parasitic currents associated with I_{ox}^{b} do not change the amount of active Li in the cell so I_{ox}^{b} could be easily incorporated into equations A.6 through A.9. During each half cycle, they serve to increase the charge *capacity* by $(Q_o\text{-}K)\ I_{ox}^{b}/I_A$ and decrease the discharge *capacity* by $(Q_o\text{-}K)I_{ox}^{b}/I_A$. Most interesting about these equations is that even though Li is lost to the SEI, via I_{Li}, this does not contribute to *capacity* loss for narrow range cycling where the negative electrode potential does not vary with *capacity*. *Capacity* fade is observed only through positive electrode damage.

Appendix B Copyright Agreement Letters

From: Aaron Smith [AJSMITH3@dal.ca]
Sent: Monday, February 13, 2012 12:46 PM
To: Copyright
Subject: Request for permission to reproduce or re-publish ECS materials

Dear ECS
My name is Aaron J Smith and I am a student of Jeff Dahn. I am seeking permission to use a few papers we have published in your journals to be reproduced as chapters in my thesis.

The title of my thesis will be: A HIGH PRECISION STUDY OF LI ION BATTERIES To be published by: Dalhousie University Four copies of my thesis will be published: 6

I will keep two copy of my thesis for myself. Other copies will be distributed between my supervisor, parents and both sets of grandparents.

The papers I am looking to reproduce are

1) A. J. Smith and J. R. Dahn, ?Delta Differential Capacity Analysis?, Journal of The Electrochemical Society, 159 (3), A290-A293 (2012).
(Published 10 January 2012)
2) A. J. Smith, J. C. Burns, D. Xiong and J. R. Dahn, "Interpreting High Precision Coulometry Results on Li-ion Cells", Journal of The Electrochemical Society, 158 (10), A1136-A1142 (2011). (Published August 15, 2011)

3) A. J. Smith, J. C. Burns, Xuemei Zhao, Deijun Xiong, and J. R.
Dahn, "A High Precision Coulometry Study of the SEI Growth in Li/Graphite Cells", Journal of The Electrochemical Society, 158 (5)
A447-A452 (2011). (Published March 10, 2011)

4) A. J. Smith, J. C. Burns, and J. R. Dahn, "High-Precision Differential Capacity Analysis of LiMn2O4/graphite Cells", Electrochemical and Solid-State Letters, 14 (4) A39-A41 (2011). (Published February 8, 2011)

5) A. J. Smith, J. C. Burns, and J. R. Dahn, "A High Precision Study of the Coulombic Efficiency of Li-Ion Batteries", Electrochemical and Solid-State Letters, 13 (12) A177-A179 (2010). (Published September 13, 2010)

6) A. J. Smith, J. C. Burns, S. Trussler, and J. R. Dahn, "Precision Measurements of the Coulombic Efficiency of Lithium-Ion Batteries and of Electrode Materials for Lithium-Ion Batteries", Journal of The Electrochemical Society, 157 (2) A196-A202 (2010). (Published December 17, 2009)

Permission is granted to include the above-referenced papers in your thesis, provided that you obtain permission of the other individual authors. In the thesis, please acknowledge the authors and the citation given above, and include the words: "Reproduced by permission of ECS — The Electrochemical Society."